2012

X-ray Radiation Enabled Cancer Detection And Treatment With Nanoparticles

Mainul Hossain
University of Central Florida

X-RAY RADIATION ENABLED CANCER DETECTION AND TREATMENT WITH NANOPARTICLES

by

MAINUL HOSSAIN
B.S. University of Dhaka, 2009
M. S. University of Central Florida, 2012

A dissertation submitted in partial fulfillment of the requirements
for the degree of Doctor of Philosophy
in the Department of Electrical Engineering and Computer Science
in the College of Engineering and Computer Science
at the University of Central Florida
Orlando, Florida

Fall Term
2012

Major Professor: Ming Su

ABSTRACT

Despite significant improvements in medical sciences over the last decade, cancer still continues to be a major cause of death in humans throughout the world. Parallel to the efforts of understanding the intricacies of cancer biology, researchers are continuously striving to develop effective cancer detection and treatment strategies. Use of nanotechnology in the modern era opens up a wide range of possibilities for diagnostics, therapies and preventive measures for cancer management. Although, existing strategies of cancer detection and treatment, using nanoparticles, have been proven successful in case of cancer imaging and targeted drug deliveries, they are often limited by poor sensitivity, lack of specificity, complex sample preparation efforts and inherent toxicities associated with the nanoparticles, especially in case of *in-vivo* applications. Moreover, the detection of cancer is not necessarily integrated with treatment. X-rays have long been used in radiation therapy to kill cancer cells and also for imaging tumors inside the body using nanoparticles as contrast agents. However, X-rays, in combination with nanoparticles, can also be used for cancer diagnosis by detecting cancer biomarkers and circulating tumor cells. Moreover, the use of nanoparticles can also enhance the efficacy of X-ray radiation therapy for cancer treatment.

This dissertation describes a novel *in vitro* technique for cancer detection and treatment using X-ray radiation and nanoparticles. Surfaces of synthesized metallic nanoparticles have been modified with appropriate ligands to specifically target cancer cells and biomarkers *in vitro*. Characteristic X-ray fluorescence signals from the X-ray irradiated nanoparticles are then used for detecting the presence of cancer. The method enables simultaneous detection of multiple

cancer biomarkers allowing accurate diagnosis and early detection of cancer. Circulating tumor cells, which are the primary indicators of cancer metastasis, have also been detected where the use of magnetic nanoparticles allows enrichment of rare cancer cells prior to detection. The approach is unique in that it integrates cancer detection and treatment under one platform, since, X-rays have been shown to effectively kill cancer cells through radiation induced DNA damage. Due to high penetrating power of X-rays, the method has potential applications for *in vivo* detection and treatment of deeply buried cancers in humans.

The effect of nanoparticle toxicity on multiple cell types has been investigated using conventional cytotoxicity assays for both unmodified nanoparticles as well as nanoparticles modified with a variety of surface coatings. Appropriate surface modifications have significantly reduced inherent toxicity of nanoparticles, providing possibilities for future clinical applications.

To investigate cellular damages caused by X-ray radiation, an on-chip biodosimeter has been fabricated based on three dimensional microtissues which allows direct monitoring of responses to X-ray exposure for multiple mammalian cell types.

Damage to tumor cells caused by X-rays is known to be significantly higher in presence of nanoparticles which act as radiosensitizers and enhance localized radiation doses. An analytical approach is used to investigate the various parameters that affect the radiosensitizing properties of the nanoparticles. The results can be used to increase the efficacy of nanoparticle aided X-ray radiation therapy for cancer treatment by appropriate choice of X-ray beam energy, nanoparticle size, material composition and location of nanoparticle with respect to the tumor cell nucleus.

Dedicated to

My parents and my sister

ACKNOWLEDGMENTS

First and foremost, I would like to thank my advisor Prof. Ming Su for his continuous guidance, support and encouragement throughout my research. His constructive criticisms and strong professionalism have helped me become a competent researcher over the years. I am grateful to my dissertation committee members, Prof. Vikram Kapoor, Prof. Aman Behal, Prof. Xun Gong, Prof. Haiyan Nancy Hu and Prof. Weiwei Deng for their invaluable suggestions and constant inspiration.

I am grateful to all members of my research group for helping me learn things quickly and efficiently. Specifically, I would like to thank Dr. Minghui Zhang and Dr. Zhaoyong Sun for numerous useful discussions; Dr. Yang Luo and Yong Qiao for assistance with cell culture and cytotoxicity assays; Dr. Yang Hong and Dr. Chaoming Wang for helping with the nanoparticle synthesis and surface modification procedures. I am grateful for their much needed friendship that helped me get through the difficult times in graduate school. I would also like to express my sincere gratitude to Dr. Wilfred Ngwa for providing valuable suggestions and insights into the numerical calculations involving radiosensitizing properties of the nanoparticles.

Finally, I would like to thank University of Central Florida, the School of Electrical Engineering and Computer Science and the NanoScience Technology Center for providing me the prestigious Graduate Fellowship Award and granting me the opportunity to carry out my research in a world class research environment.

TABLE OF CONTENTS

LIST OF FIGURES

LIST OF TABLES

CHAPTER 1:INTRODUCTION

1.1 Early Detection of Cancer

Cancer is a highly complex disease in which genetic alternations cause cells to divide without control and spread into other tissues and organs. Nation`s leading cancer organizations estimated a total of 1,596,670 new cases of cancer with 571,950 projected deaths for the year 2011 in the United States alone.[1] According to the American Cancer Society, cancer still remains the second major cause of death in the United States of America in 2010, next only to cardiovascular diseases. Worldwide, 12.5% of the deaths are caused by cancer which is more than the total percentage of deaths from AIDS, malaria and tuberculosis combined. The trends in incidence and death rates differ from one type of cancer to another and depend on several factors including age, sex, ethnicity, socio-economic condition and access to medical or healthcare facilities for cancer diagnosis and treatment. Although, the overall number of cancer patients and those dying from the disease have declined over the past decade, cancer still continues to be a major threat with over 11 million projected deaths worldwide in 2030.[2]

According to the World Health Organization (WHO), existing modalities for cancer management can prevent only up to one-third of new cancer cases. The rest two-third needs to be dealt with strategies that integrate early detection with effective treatment measures.[3] Early detection refers to the timely diagnosis of cancer in symptomatic individuals and screening in asymptomatic persons who are at risk of developing the disease. Early diagnosis can reduce mortality and recurrence probability of cancer by allowing early treatments when tumors can be

easily treated.[4] Unfortunately, cancer is often diagnosed and treated too late when the cancer cells have already invaded other parts of the body by a process known as metastasis. In metastasis, tumor cells detach from primary sites and are carried by bloodstream to distant organs where they can implant themselves giving rise to secondary tumors. The early detection and removal of these circulating tumor cells (CTCs) from blood can play an important role in preventing the onset of metastasis, which causes death of over 90% of cancer patients. For example, the five year survival rate of localized breast cancer is 95%, while that for metastatic cancer reduces to 30%, thus highlighting the importance of early detections in cancer management.[5] However, early and accurate diagnosis of cancer remains a challenging task since many of today`s diagnostic techniques are limited by poor sensitivity, extensive sample preparation efforts, long turnover times, lack of multiplicity, high cost, and high rate of false positives. In addition, diagnosis is followed by treatment that often involves frequent exposure to high radiation doses, chemotherapy and invasive measures like surgery which prolong patient suffering.

1.2 Nanotechnology in Cancer Management

Nanotechnology is a multidisciplinary field that involves the design and engineering of nano-tools and nano-objects between 1-100 nm in size. At the nanoscale, quantum mechanical effects start to dominate and the physical, chemical, and biological properties of materials differ from their bulk counterparts.[6] By creating nanometer-scale structures, it is possible to control

fundamental characteristics of a material, including its melting point, magnetic properties, and even color, without changing the material's chemical composition.

According to the National Cancer Institute, nanotechnology promises to achieve significant breakthroughs in the fields of cancer diagnosis, treatment and prevention. Nanoscale objects such as nanoparticles and quantum dots are smaller than the human cells (5-10 μm in diameter) and can readily interact with biomolecules on both the cell surface and within the cell. These molecular level interactions provide useful information for monitoring complex cellular processes including the onset of biomolecular transformations leading towards cancer metastasis. The surfaces of nanoparticles can be modified with appropriate ligands to target tumor cells with high specificity and affinity and are used extensively for delivering therapeutic drugs and imaging contrast agents to the cancer cells while sparing the normal healthy cells. Surface modifications render nanoparticles biocompatible and reduce toxicity levels, which is crucial for *in vivo* applications. Applications of nanotechnology for cancer management involve the use of nanoparticles for detecting cancer at its earliest stages, precisely locating its position within the body, delivering anticancer drugs, specifically to malignant cells, and determining if these drugs are killing the malignant cells. Figure 1-1 summarizes the cancer nanotechnology applications through molecular tumor imaging, early detection, molecular diagnosis, targeted therapy, and bioinformatics.[7]

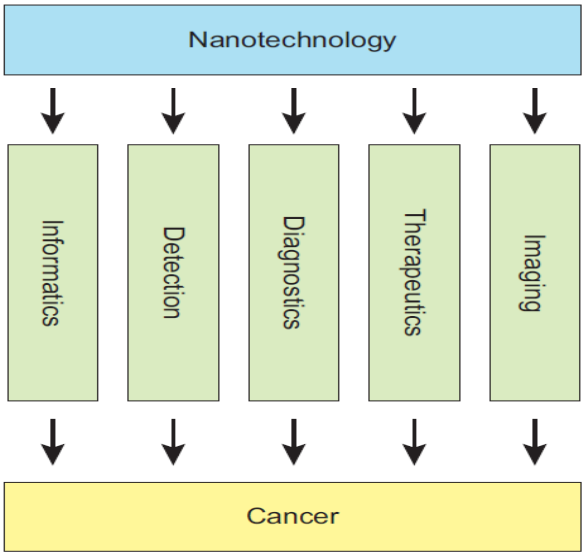

Figure 1-1 Nanotechnology applications in cancer management.

Imaging of tumors for cancer detection is currently being achieved through several modalities that include X-ray based computed tomography (CT), positron emission tomography (PET), single photon emission computed tomography (SPECT) and magnetic resonance imaging (MRI). Although, methods like CT, MRI and X-rays have achieved high spatial resolution, they use non-targeted contrast agents and are often unable to distinguish cancer cells from normal cells at early stages of cancer development. The efficacy of existing imaging techniques can be greatly enhanced using targeted nanoparticles to specifically bind to or penetrate tumor cells.[8] For instance, bioconjugated prostrate membrane antigen targeting quantum dots have been used successfully for simultaneous targeting and imaging of prostate tumors in living mice. The key lies in identifying one or more target molecules that are overly expressed in cancer cells but are rare in normal cells. The large surface area of nanoparticles allows them to be conjugated with a variety of functional groups or ligands that can be combined with multiple diagnostic and therapeutic agents for simultaneous detection and treatment of cancers. Moreover, the

nanoparticles encapsulated with biocompatible polymers have prolonged circulation in blood and can accumulate at sufficient concentrations inside the tumor cells for producing high contrast images. Since cancer is a heterogeneous disease, diagnosis and treatment largely depends on the molecular profiles of the individual patients. Recent advances in cancer nanotechnology offer exciting opportunities for personalized oncology in which diagnosis and treatments can be tailored based on the exact genetic and molecular characteristics of the individual concerned. This is further aided by bioinformatics tools that can analyze massive amount of genomic and proteomic data along with patient histories for identifying and validating multiple cancer biomarkers.[9]

1.3 Role of Biomarkers in Cancer Detection

Cancer biomarkers are found in tumor tissues or serum and include a wide variety of molecules such as deoxyribonucleic acid (DNA), messenger ribonucleic acid (mRNA), transcription factors, cell surface receptors, and secreted proteins. Cancer biomarkers can be used for prognosis to predict the natural course of a tumor, indicating whether the outcome for the patient is likely to be good or poor. They also enable monitoring of a patient`s response to a given drug and the efficacy of the drug. Identifying the presence of biomarkers allows early detection of cancers. However, since cancer is a heterogeneous disease, detection of a single biomarker is insufficient for providing information about tissue type and malignant transformation throughout the various stages of tumor development and progression.[10] In addition, biomarkers are present in extremely low concentrations and are difficult to detect in the

background of complex body fluids. Parallel to efforts to find specific biomarkers, a feasible way of enhancing diagnostic reliability is to detect multiple cancer biomarkers with high sensitivity at the same time.[11] The multiplexed detection reflects functional relation among biomarkers, and identifies biomarkers associated with different stages of disease, allowing early detection of lethal cancers.

Nanoparticles with unique optical, electrical, magnetic or electrochemical signatures can be used for biomarker detection owing to their intimate contact with biomolecules. Extremely high sensitivities have been achieved at pico or femto-mole/liter levels by converting bio-recognition events into measurable physical signals that can be amplified.[10] But, the multiplicity of nanoparticle detections using optical methods is limited due to narrow operating range and broad peak: only one or few types of biomarkers can be detected at one time; and screening multiple biomarkers in a sample will take long time, a lot of agents and effort. Commonly used techniques for cancer biomarker detection include polymerase chain reaction (PCR), enzyme-linked immunosorbent assay (ELISA), and DNA microarray. These methods have certain benefits such as high throughput, but they mostly suffer from poor sensitivity and extensive sample preparation efforts. An ideal detection scheme would be one that offers high sensitivity and multiplicity for identifying multiple biomarkers at ultralow concentrations.

1.4 Role of Circulating Tumor Cells in Cancer Metastasis

Metastasis in cancer patients is characterized by the presence of tumor cells that are shed into blood from primary tumors and carried by the bloodstream to distant organs. These

circulating tumor cells or CTCs directly correlate with metastatic disease state providing useful information about tumor growth and regression as well as disease progression. Detection and analysis of CTCs therefore play a crucial role in predicting the prognosis and overall survival of cancer patients and are essential for selecting and monitoring cancer therapy.

1.5 Radiation Induced Damage of Cancer Cells

Radiation therapy typically uses high doses of radiation such as X-rays for killing cancer cells or tumors. Together with chemotherapy and surgery, radiation therapy forms one of the most important methods of cancer treatment. Being highly penetrating, X-rays and γ-rays can be used to treat deeply buried cancers without using invasive measures. In radiation therapy, a beam of radiation attenuates as it passes through the patient, depositing energy along its path. The energy deposited per unit mass is referred to as the dose. At high doses, radiation damages the DNA inside tumor cells making them unable to grow and divide, eventually causing cell death. The killing effect is achieved either directly through the interaction of radiation with tumors or indirectly through the hydrolysis of water molecules inside tumor cells. The latter generates large numbers of highly reactive and unstable free radicals or reactive oxygen species (ROS), which immediately react with any biomolecules in the surrounding area, causing irreparable cellular damage. Figure 1-2 illustrates the mechanism of DNA damage using X-ray radiation.

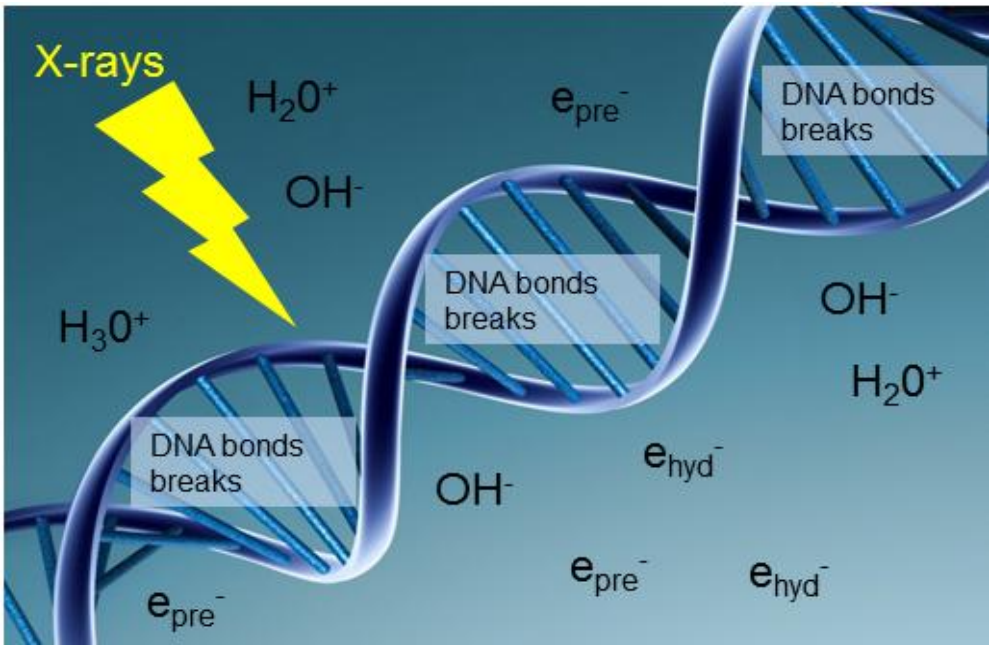

Figure 1-2 Mechanisms for radiation induced DNA damage.

The free electrons generated from hydrolysis of water lose their kinetic energy and enter into a pre-hydrated state (e^-_{pre}). Prehydrated electrons then form complexes with water molecules and hydrated electrons (e^-_{hyd}). Prehydrated electrons also react with the bases of DNA duplexes, forming transient anions which in turn could decompose, breaking molecular bonds in the DNA. Although, radiation therapy is targeted towards solid tumors inside the body, normal and non-cancerous cells surrounding tumors will also be affected by the radiation. Radiation therapy therefore aims to maximize the dose to tumor cells while minimizing exposure to normal, healthy cells.

Careful treatment planning by a radiation oncologist and use of techniques such as collimation or beam filtration can minimize radiation damage to normal cells. However, these measures still suffer from lack of selectivity between malignant and healthy cells. Preferential uptake of high atomic number (Z) nanoparticles such as gold (Z = 79) by the tumor cells have

been shown to produce localized dose enhancements upon irradiation by kilovoltage X-rays. Previous studies demonstrated ~30-50% increase in radiation induced damage to tumor cells loaded with X-ray absorbing metallic microspheres. These high Z agents provide a high probability for photon interaction by photoelectric effect. Increased absorption of X-rays by the high Z nanoparticles attached to the tumor wall transfers a large portion of the energy of the primary ionizing photons directly to the tumor. The high linear energy transfer of resulting photoelectrons, characteristic X-rays and Auger electrons are responsible for localized dose enhancements causing lethal damage to the tumor cells while sparing normal, healthy cells. The enhancement factor depends on the size, location and concentration of the nanoparticles, the energy of the primary X-ray beam as well as the cell type that is being irradiated. A combined treatment strategy with nanoparticles and X-rays therefore promises better tumor control than either nanoparticles or X-rays alone.

1.6 Needs for an Integrated Cancer Management System

It is clear that early detection of multiple cancer biomarkers and CTCs in blood play a significant role in enhancing the survival rate in cancer patients. Although new and improved techniques for detection and treatment of potential cancers have emerged over the past decades, most of them have not been incorporated into clinical practices due to their complex nature and lack of reliability in identifying multiple cancer types *in vivo*. Moreover, an integrated system that combines both detection and treatment has not yet been demonstrated. Here, we propose a novel technique for detecting and quantifying multiple cancer biomarkers and CTCs with high

sensitivity and specificity using characteristic X-ray fluorescence signatures from targeted metallic nanoparticles. Once the tumor has been identified, X-ray dose can be tuned to kill cancer cells in-situ and on demand, allowing simultaneous detection and treatment. Synthesized high Z metallic nanoparticles are modified with appropriate ligands to bind with targeted cancer biomarkers (DNAs and proteins) by forming a double helix DNA chain or sandwiched antibody-antigen complexes. Nanoparticles are also combined with folic acid ligands to be conjugated with the folate receptors overexpressed on the surface of certain cancer cells. The targeting specificity of the nanoparticles and the level of toxicity have been investigated through several experiments as described in the subsequent sections. The actual design incorporates a portable X-ray tube and detector that is capable of detecting X-ray photons with energies ranging between 0-40 keV at a resolution of 145 eV. Characteristic X-ray fluorescence signals that are induced from the metallic nanoparticles upon X-ray irradiation can be used to detect the presence of cancer biomarkers and tumor cells while strength of the signal can be used for quantifying the extent of the disease.

The proposed mechanism offers a number of advantages over the current methods of cancer detection. Since X-ray signatures are unique to individual elements, different nanoparticles can be used to target multiple tumor types (or biomarkers) at the same time, allowing multiplexed detection with high sensitivity and specificity. Results are obtained instantaneously as the samples are being irradiated and long turnover times are not required as in the case of existing techniques. In case of *in vivo* applications, this significantly reduces patient exposure time, thereby lowering the risks of inducing secondary cancers due to over doses of radiation. In addition, surface modifications have been performed to reduce inherent nanoparticle

toxicities. With high penetrating power of X-rays, the method can eventually be used to detect deeply buried cancers *in vivo*. X-ray dose can be easily tuned by varying the tube current, voltage and using appropriate collimation and filtration of the X-ray beam in order to achieve desired killing of cancer cells. Dose management and radiosensitizing effect of nanoparticles targeted towards the cancer cells are essential in order to minimize damage to the healthy cells while at the same time maximizing the lethal effects in cancer cells. For *in vitro* analysis, little or no sample preparation is required. The device for X-ray irradiation and characteristic fluorescence detection is highly portable and can be readily integrated into existing clinical settings. Moreover, data acquisition is fully automated and can be analyzed very quickly with commercially available softwares.

1.7 X-rays

Since its discovery in 1895 by physicist W.C Rontgen, X-rays have been used extensively for both diagnosis and therapy. X-rays are highly penetrating and invisible electromagnetic radiation capable of producing images of tissues, bones, and organs and detecting tumors inside the human body. X-rays are more readily absorbed by bones than by surrounding blood and tissues producing images with distinct contrasts that allow identification of solid tumors or lesions. Moreover, X-ray irradiation of cells and tissues can generate free radicals that can damage the DNA of cancer cells as described in section 1.5. Use of X-rays therefore allows simultaneous detection and treatment of cancer.

1.7.1 X-ray Generation

X-rays are commonly produced by accelerating electrons through a potential difference and directing them onto a target material (typically tungsten). The high energy electrons are decelerated in the strong electromagnetic field of the target atom's electrons or nucleus. The deceleration of the fast moving electrons produces a continuous spectrum of bremsstrahlung or braking radiation and the characteristic X-rays. The continuous spectrum of the braking radiation extends from zero up to the particles` initial energies. For the sharp peaks of the characteristic X-rays, their energies correspond to the energy levels of the atomic electrons in the target material. The characteristic X-ray lines are superimposed on the continuous bremsstrahlung X-ray spectrum. Figure 1-3 shows a typical X-ray spectrum from a tungsten target X-ray tube:

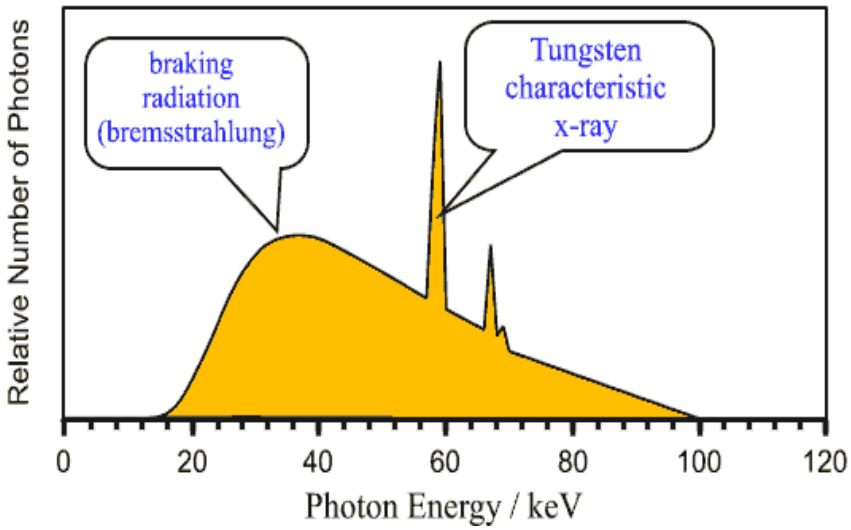

Figure 1-3 X-ray spectrum from a tungsten X-ray tube.

1.7.2 X-ray-Matter Interaction

Figure 1-4 illustrates the various methods by which X-rays can interact with materials. Figure 1-4A represents the primary, unattenuated radiation that passes through a material without any interaction. The main interactions responsible for diagnostic and therapeutic X-rays include elastic and inelastic scattering and photoelectric absorption. Pair production occurring for extremely high energy (1.02 MeV) X-ray photons has not been discussed here.

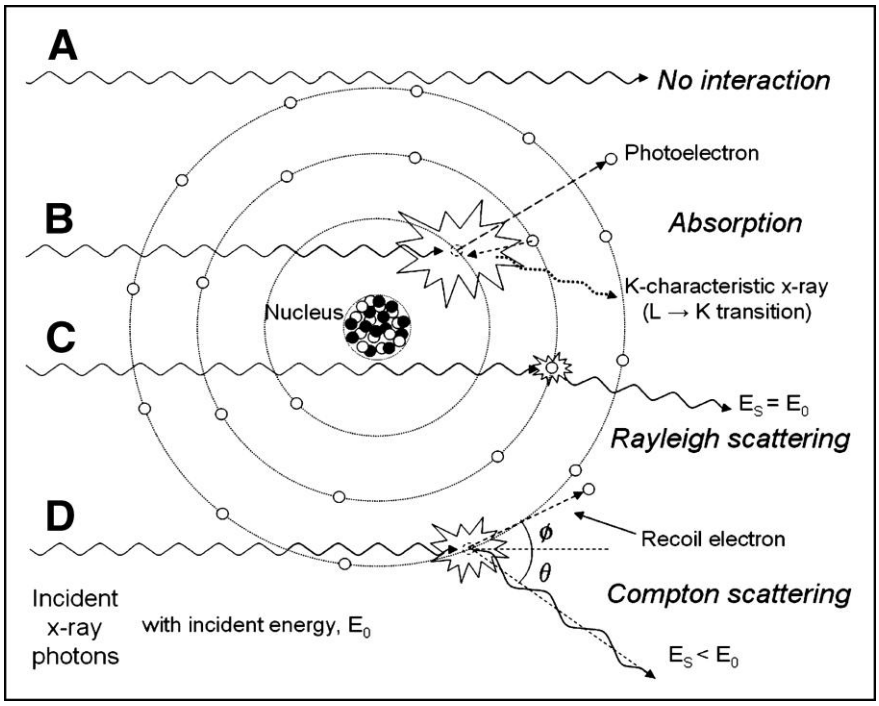

Figure 1-4 X-ray interactions with atoms.

In elastic or Rayleigh scattering, an incoming X-ray photon undergoes collision with an electron in an atom. Upon collision, the incident X-ray photon is deflected without any loss of energy (Figure 1-4C). The energy of the electron is raised but it is not removed from the atom. When the electron returns to its previous energy level it emits an X-ray photon with energy equal

to that of the incident one but with a slightly different direction. The probability of Rayleigh scattering increases with increasing Z of the target atom and decreasing X-ray energy.

For inelastic or Compton scattering, an X-ray photon of energy $E_{o,}$ greater than the binding energy of an atomic electron, collides with an electron in an atom. The photon gives either the whole or a part of its energy to the electron (Figure 1-4D). The electron receiving partial energy from the X-ray photon recoils and is removed from the atom at an angle ϕ. The rest of the energy E_s is transferred to the scattered X-ray photon which is deflected at an angle θ relative to the incident photon. The probability of Compton interaction is proportional to the electron density of the material concerned and is independent of E_o for energies ranging between 10-150 keV. Above 150 keV, the probability decreases approximately as $1/ E_o$

When the incident X-ray photon has sufficient energy E_o to eject an electron from the atom, the phenomenon is described as photoelectric absorption (Figure 1-4B). The kinetic energy of the ejected electron is given by the difference between the incident X-ray photon energy E_o and the binding energy E_{BE} of the electron shell .The probability of photoelectric absorption is proportional to the cube of the atomic number of the interacting atom and inversely proportional to the cube of the energy, as Z^3/E_o^3. Photoelectric interaction is more likely to occur with higher atomic number elements and lower X-ray energies. In photoelectric effect, ejection of electron from its shell leaves the atom in its excited state which shortly returns to its stable state through one of two possible mechanisms: X-ray fluorescence and Auger effect. The first effect results in the emission of a characteristic X-ray while the latter results in the ejection of another electron (Auger electron) from the atom.

1.7.3 X-ray-Fluorescence (XRF)

X-ray fluorescence (XRF) is defined as the emission of characteristic "secondary" (or fluorescent) X-rays from a material that has been excited by bombarding with high-energy particles or X-rays. The phenomenon is widely used for elemental analysis since it is quick, non-destructive and also offers simultaneous detection of multiple elements based on characteristic XRF signals.

According to the Bohr Theory of atoms, electrons in an atom are arranged in shells surrounding the nucleus. The shells are designated as K, L, M, N … corresponding to n = 1, 2, 3, 4 with K-shell being the innermost shell followed by the second innermost L-shell and so on. Other discrete energies exist within each shell which is due to different subshells (orbitals of identical n but differing l) within each shell. Photoelectric absorption of primary X-ray photons by an atom typically results in the ejection of electrons from the K-shell. The vacancy left behind by the ejected electron will be filled up by an electron from the outer shell (L-shell or M-shell) with less binding energy, producing characteristic X-ray photons with energy equal to the difference in electron binding energies of the two corresponding electron shells. The process is illustrated in Figure 1-5:

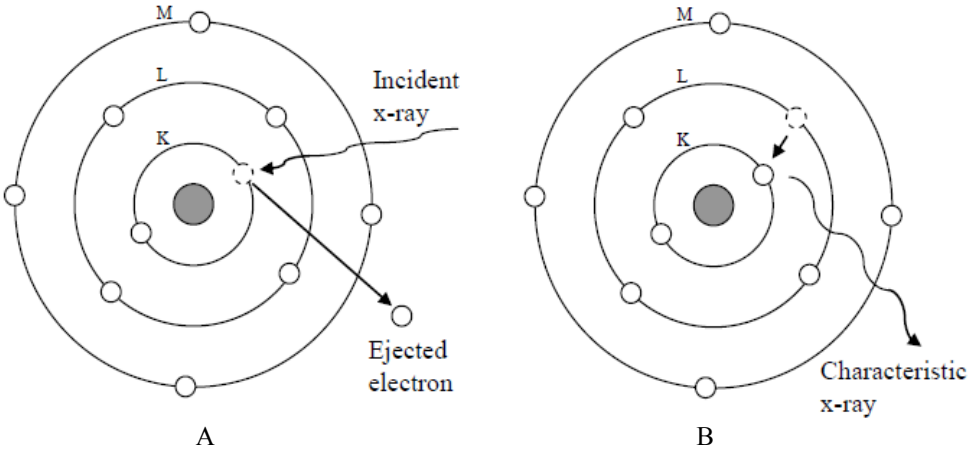

Figure 1-5 A typical XRF phenomenon. Incident X-ray photon ejects K-shell electron (A) L-shell electron fills the K-shell vacancy resulting in the emission of secondary X-rays (B).

The most common electron transition occurs from the L-shell to the K-shell and the corresponding X-ray energy is referred to as K_{α}. This is further classified into $K_{\alpha 1}$ and $K_{\alpha 2}$ depending on the L-subshell responsible for the transition. In a typical XRF spectrum, $K_{\alpha 1}$ and $K_{\alpha 2}$ show up as pronounced peaks superimposed on the bremsstrahlung as shown in Figure 1-6.

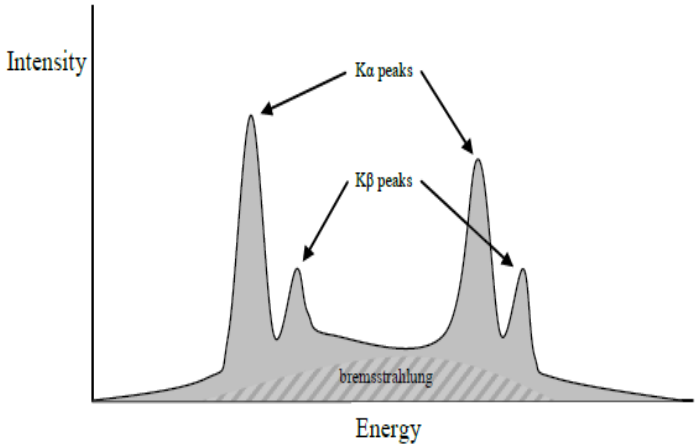

Figure 1-6 Typical XRF spectrum with K-peaks.

The transition from M-shell to K-shell refers to the K_β energies ($K_{\beta 1}$ and $K_{\beta 2}$). Similarly, M-shell to L-shell and N-shell to L-shell transitions yield L_α ($L_{\alpha 1}$ and $L_{\alpha 2}$) and L_β ($K_{\alpha 1}$ and $K_{\alpha 2}$) X-ray photons respectively. Figure 1-7 shows the energy levels involved in the production of K and L-line X-rays:

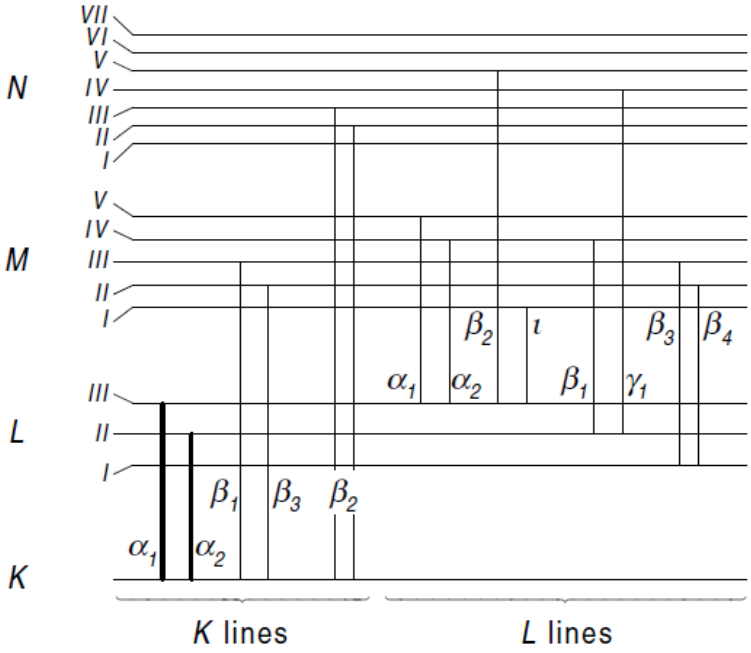

Figure 1-7 Main lines in the K and L spectra.

Since each element can be characterized by a unique set of energy levels, the energy of these characteristic X-rays are specific to every element. This is in accordance with Moseley`s law which describes the relation between atomic number (Z) and energy (E) of a spectral line according to $E\ (keV) = K\ (Z-1)^2$ where $K = 1.042\times10^{-2}$ for the K-shell and 1.494×10^{-3} for the L-shell For example, the $L_{\alpha 1}$ XRF peak of gold (Z = 79) occurs at 8.40 keV while the $L_{\alpha 1}$ XRF peak of lead (Z = 82) occurs at 10.55 keV. As a result, using high resolution X-ray detectors,

characteristic XRF peaks can be detected and used to identify the element. In addition, if background correction is made, the area under the corresponding XRF peak can be used to quantify the amount of the element present in the sample.

As described in section 1.7.2, ionizations followed by photoelectric absorption do not always result in X-ray emissions. The Auger effect competes with the production of fluorescent X-rays. The fluorescence yield of an atomic shell or sub shell is defined as the probability that a characteristic X-ray photon is emitted when one of the outer electrons fills the vacancy in an inner shell. Mathematically, the ratio of the number of emitted X-rays to the total number of ionizations is the fluorescence yield ω_i where i designates the shell involved. Fluorescence yield increases with atomic number and is greater than 95% for K X-rays of elements with Z >78. For a given element, the fluorescence yield decreases from the K series to the L and M series. The fluorescence yield can be approximated by $\omega_i = Z^4/(A_i+Z^4)$ where A_i is approximately 10^6 for the K shell and 10^8 for the L shell.

1.8 Energy Dispersive X-ray Fluorescence Detection System

A basic XRF system consists of four essential components:

1. A X-ray source
2. A sample
3. A detector
4. A data acquisition and collection system

Figure 1-8 illustrates a typical energy dispersive XRF (EDXRF) system where the X-ray tube and detector are arranged in reflection mode:

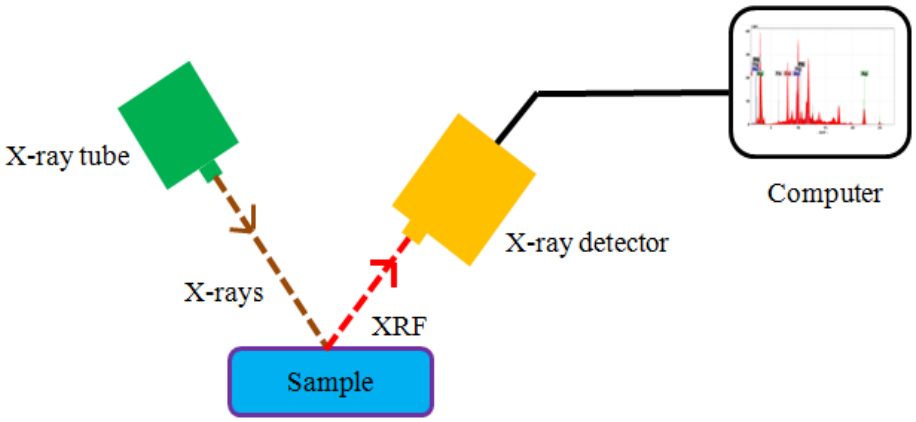

Figure 1-8 EDXRF detection system.

A polychromatic beam of X-rays from the X-ray tube excites the atoms in the sample resulting in the emission of secondary X-rays (XRF) that are characteristic of the elements present in the sample. The detector collects the emitted X-rays and sends electrical pulses to the data acquisition system in order to produce a spectrum showing the intensity (counts) of X-rays with respect to the energy of the X-ray photons. The process is often referred to as energy dispersive XRF or EDXRF. One or more peaks for each element present in the sample are observed in a typical XRF spectrum. The elements can be identified by looking up the corresponding energy value from a standard XRF chart. Figure 1-9 shows a complete setup of the EDXRF system used in our experiments:

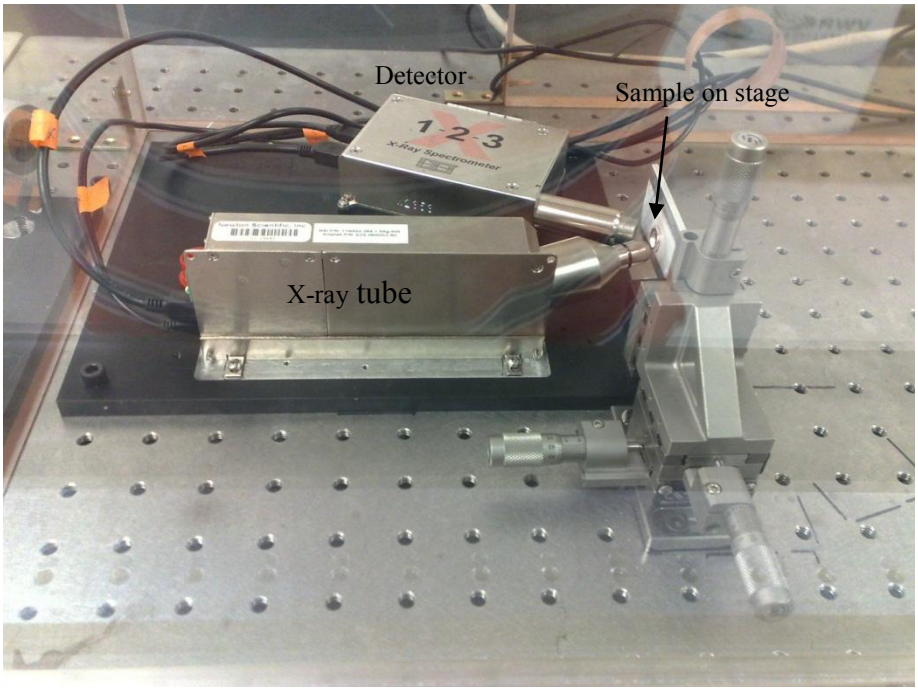

Figure 1-9 Complete EDXRF detection system.

1.8.1 X-ray Tube

In the following experiments Amptek`s (Bedford, MA) Mini-X X-ray tube is used which is a self-contained, packaged, miniature X-ray tube system. It includes the X-ray tube, the power supply, the control electronics and the USB communication to the computer. A grounded anode together with variable current and voltage via USB allows ease of operation. Mini-X features a 40 kV/100 μA power supply, a silver (Ag) transmission target, and a beryllium end window and generates X-ray photons with energies ranging between 0-40 keV. A flashing red light emitting diode (LED) and a beeper acts a warning for the user when X-ray is turned on. The Mini-X is provided with a collimator to facilitate its use in XRF applications. It consists of a brass collimator with an aluminum insert and a cover that screws into the Mini-X. The collimator has a

2 mm diameter hole, reducing the focal spot size to 2 mm. Without the collimator the X-ray beam spreads into a 120°cone, whereas, the collimator reduces the cone to about 10°. In addition, a set of filters with varying materials and thickness is also available to tune the generated X-ray spectrum.

1.8.2 X-ray Detector

The detector used is Amptek`s X123. It is a compact, integrated system consisting of the X-ray detector and preamplifier, digital pulse processor (DP5), multi-channel analyzer (MCA) and a power supply. The complete architecture of X-123 is shown in Figure 1-10:

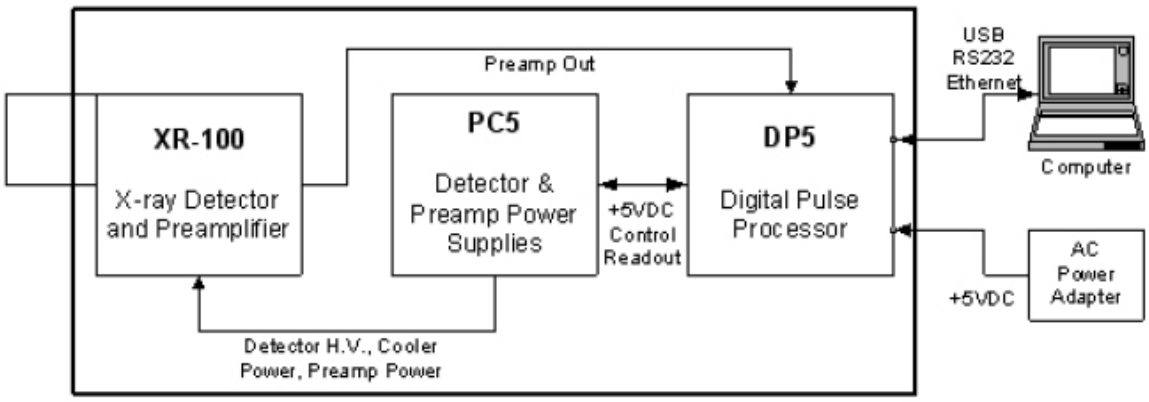

Figure 1-10 X-123 architecture.

The typical detector is a Si-PIN photodiode: X-rays interacting in the silicon create an average of one electron/hole pair for every 3.62 eV of energy lost in the silicon, which is the input signal. The detector is mounted on a thermoelectric cooler along with the input field effect transistor (FET) and coupled to a custom charge sensitive preamplifier. The thermoelectric

cooler reduces the electronic noise in the detector and preamplifier. The digital pulse processor digitizes the preamplifier output, applies real-time digital processing to the signal, detects the peak amplitude (digitally), and bins this value in its histogramming memory, generating an energy spectrum. The spectrum is then transmitted over the DP5's interface to the user's computer.

The energy resolution of a detector is its ability to resolve X-ray photons of different energy (or wavelength). The resolution is generally measured as the full width of the peak at half maximum intensity (FWHM), and is given by FWHM/H_0 where H_0 is the highest energy peak. The energy resolution for X123 for the 5.9 keV peak of ^{55}Fe is 145 eV FWHM to 260 eV FWHM depending on detector type and shaping time constant.

1.8.3 Calibration

The key to XRF measurements lies in precisely identifying the energy at which the XRF peak occurs. This can be achieved through accurate calibration of the detector prior to measurements. Once an X-ray photon impinges on the detector, it sends out an electrical pulse to the MCA. MCA will allocate X-ray photons to their appropriate channel depending on the energy. The data recorded is an array of numbers, each number representing the total count of X-rays for that energy (intensity). The number placement in the array represents the channel number, in ascending order. Figure 1-11 shows the MCA where each box represents a channel and the number inside the box denotes the count of X-rays for a specific energy

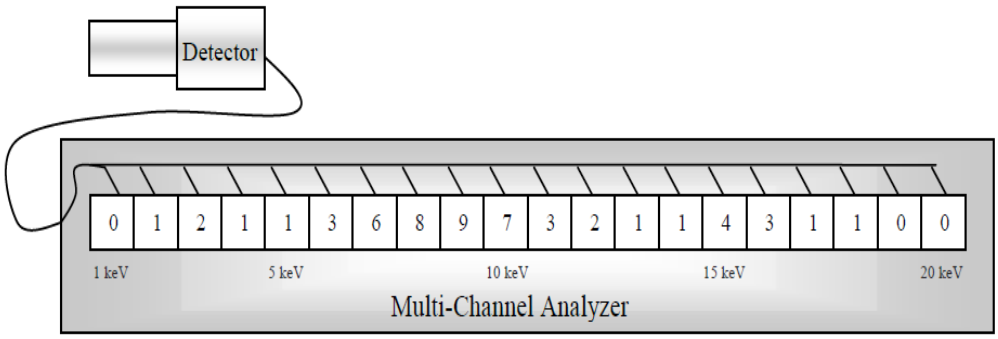

Figure 1-11 Multichannel analyzer.

During calibration, specific energy values are assigned to the correct channel in the MCA. This is done by collecting the XRF signal from a standard sample whose XRF peak energies are known. Once the channels, where the X-rays are allocated are identified, the known energy values can be assigned to those channels. The calibration process consists of identifying at least two channels with known energy values and then applying a curve fitting technique to those data points. Typically a linear fit is used as shown in Figure 1-12:

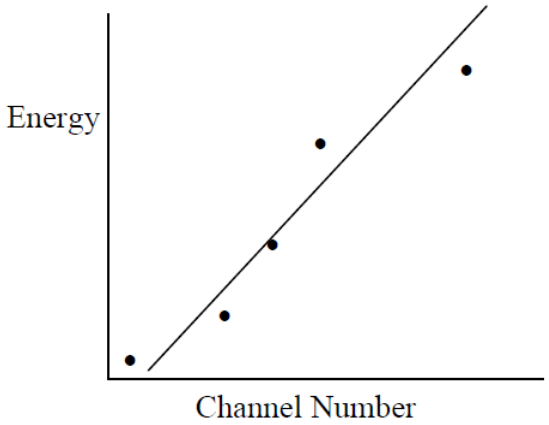

Figure 1-12 Linear fit for MCA calibration.

For calibrating our instrument a standard stainless steel (SS316) sample has been used. SS316 consists of iron (Fe), molybdenum (Mo) and manganese (Mn) among other elements. The sample is fixed onto a holder at a distance of 2 cm from the tube and the detector and is exposed to X-rays at 40 kV and 100 μA for 2 min using the setup in Figure 1-9.

The channel scale is converted to an energy scale using the ADMCA software provided with the system. First, the full scale range (in this case 40 keV) of the detector is set by adjusting the gain of the amplifier to 38. Since the XRF spectrum of standard SS316 sample is known, energy values can be assigned to appropriate channels. An automatic calibration is performed by ADMCA using a linear fitting technique.

1.8.4 Data Acquisition and Analysis

XRF spectrum is collected and analyzed using Amptek`s ADMCA software package. The software also provides full control for Amptek signal processors and X-ray spectrometers. Features such as peaking time, gain, total count, input count, etc. can also be controlled. The spectrum is displayed in real time showing discrete energy peaks. Data analysis includes calculation of centroid, FWHM, net area, and other quantities. Simple arithmetic manipulation, e.g. subtracting a “blank” or “background” spectrum, scaling to match previous data, etc can be performed easily using ADMCA.

1.8.5 Safety Measures

The setup is housed inside a custom designed lead acrylic chamber with 1 mm lead equivalent thickness that is capable of stopping X-rays with energies of up to 100 keV from reaching the exterior. The Mini-X has also a hardware interlock in order to prevent accidental exposure. This interlock must be shorted (enabled) in order for the Mini-X to produce X-rays. Figure 1-13 (right) and 1.-13 (left) show the enabled and disabled configurations, respectively, for the interlock system.

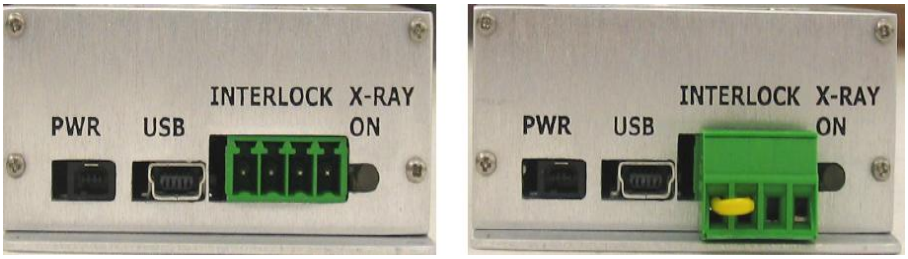

Figure 1-13 Mini-X interlock enabled (right) and disabled (left).

The interlock allows interfacing of external safety mechanisms. A safety lock (not shown in the figure) consisting of a reed switch is installed on the door of the chamber and wired to the interlocks of the X-ray tube. The external circuit is powered by a 5 V d.c. power supply. When the door is open, the magnetic switch keeps the interlocks in open circuit configuration and therefore the X-ray tube cannot be turned on. Once the door is closed, the interlock is shorted and X-ray production can resume.

CHAPTER 2:X-RAY FLUORESCENCE DETECTION OF MULTIPLE CANCER BIOMARKERS WITH NANOPARTICLES

2.1 Introduction

Detecting DNA and protein biomarkers with high sensitivity allows early detection of cancers. Although many cancer biomarkers with certain specificity have been found, it is clear that no single biomarker is likely to distinguish lethal cancer from indolent ones at early stages due to lack of tumor specificity. Limitations of existing techniques for cancer biomarker detection have already been mentioned in section 1.3.The interaction of incoming X-rays with atoms generates characteristic X-ray fluorescence (XRF) signals, which can be used to quantify trace elements in tissues such as bones and also identify cancers with high sensitivity and specificity.[12-19] Though XRF has shown great potential for tissue imaging, it has not been applied to biomarker detection by intentionally introducing nanoparticles. This work describes an XRF based technique for multiplexed biomarker detection using a panel of metal and alloy nanoparticles. These nanoparticles are modified with ligands of biomarkers to establish a one-to-one correspondence, and immobilized on a substrate that has been modified with ligands through ligand-biomarker interaction, after forming complexes with target biomarkers in three strand or sandwich configurations (Figure 2-1).

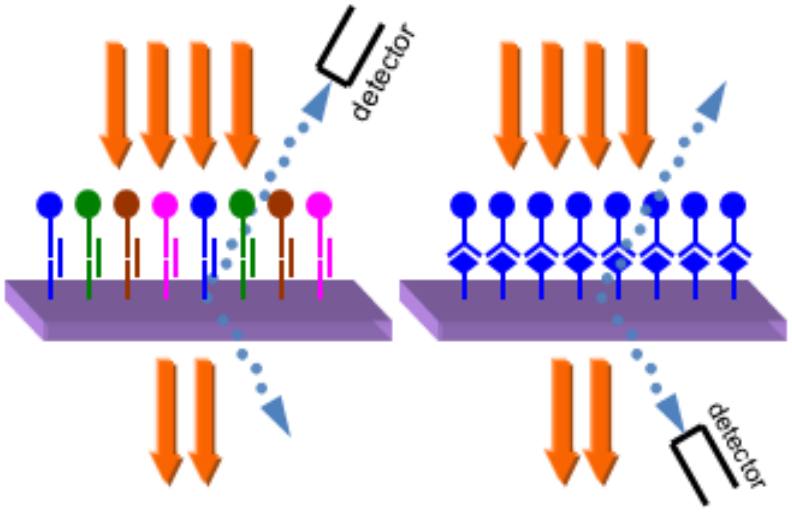

Figure 2-1 Biomarker detection based on XRF of composition-encoded nanoparticles, where three-stranded detection of oligonucleotides and sandwich detection of protein are carried out in reflection mode, and transmission mode, respectively.

The nature and amount of multiple biomarkers can be detected at high sensitivity by determining the presence and amount of according nanoparticles with characteristic XRF. The high penetrating power and non-destructive nature of X-rays also allow quantitative imaging of multiple biomarkers, where results can be obtained instantaneously with high spectral resolution. The nanoparticles are very stable under physiological conditions even without silica or polymeric coating, and can be used for either *in vitro* detection or *in vivo* imaging, or biomarker profiling in tissue samples.

2.2 Experimental Section

2.2.1 Synthesis of Nanoparticles

Metallic nanoparticles of metals and alloys such as indium, bismuth, tin, and lead-tin alloy nanoparticles are made by thermal decompositions of organometallic precursors in ethylene glycol in presence of a surfactant (polyvinyl-pyrrolidone or PVP) at 200°C under nitrogen protection. After reacting for 30 min, reactions are quenched in 200 ml of ethanol pre-cooled at 0°C. Nanoparticles are separated from un-reacted precursors by centrifugation, washed by ethanol, and dried. The morphologies of nanoparticles are confirmed by using transmission electron microscopy (TEM). The average diameter of the synthesized nanoparticles was 30 nm.

2.2.2 Surface Modifications

The as-synthesized nanoparticles are surface-oxidized by heating at 110°C for 10 min in ambient condition, and aminized by incubating in 5% alcoholic solution of (aminopropyl)triethoxy-silane (APTES) for 1 h. After removing excess silane by centrifugation, aminized nanoparticles are suspended in dimethyl sulfoxide (DMSO) containing 5% N-succinimidyl (4-iodoacetyl) aminobenzoate (SIAB) for 20 min. After removing excess SIAB, nanoparticles are incubated with thiolated probe single strand DNA (ssDNA) in phosphate buffer solution (PBS, pH 7.0) at room temperature for 3 h. Amine-modified nanoparticles are then incubated with disuccinimidyl suberate (DSS) in DMSO for 1 h. After removing excess DSS, nanoparticles are incubated with antibody inside PBS for 3 h. Solid substrates (i.e., aluminum

plates) are modified with capture ssDNA or antibody using similar methods as described for the modification of the nanoparticles.

2.2.3 XRF Detection

A Mini-X X-ray tube (Amptek, Bedford, MA) operating at a voltage of 40 kV and tube current of 15 μA is used to generate primary X-rays. The tube is fitted with a brass collimator to reduce beam size to 2 mm in diameter. An X-ray spectrometer (Amptek X-123) with thermoelectrically-cooled Si-PIN photodiode is used to analyze XRF emissions. The spectrometer contains detector, digital pulse processor, and multichannel analyzer, interfaced with computer for data acquisition and analysis. XRF signals from the X-ray irradiated nanoparticles are detected in both transmission and reflection modes (Figure 2-1). In transmission mode, X-ray tube and detector are aligned in the same line; while in reflection mode, the tube and the detector are fixed on a mounting plate with an angle of 45° between them. The tube-sample distance and sample-detector distance are kept at 3 and 2 cm, respectively. The detector gain and peaking time are adjusted to keep dead time below 60%. The whole setup is enclosed in a lead containing acrylic chamber with 1 mm of lead equivalent thickness. The primary 40 kV X-rays can excite electrons with binding energies below 40 keV, thus only *L* line emissions can be excited in case of high atomic number nanoparticles (i.e., lead and bismuth). Background spectra are obtained using fresh aluminum plate that does not contain immobilized nanoparticles.

2.3 Results and Discussions

The detection is carried out in three stranded configuration (DNA) or sandwich configuration (protein). Ligand-modified aluminum plates are immersed in PBS solutions containing target single strand DNA (ssDNA) at pH 7.0 for 3 h. The capture and probe DNA will bind specifically to the target DNA through the bonding between complementary base pairs and thereby form the three stranded configuration. Prior to X-ray exposure, the aluminum plates are washed with PBS (pH 7.0) for three times in order to remove any unbound or non-specifically bound nanoparticles. Following this, the plates are dried in air and tested using the XRF setup of Figure 1-9. Figure 2-2(A) shows lead $L_{\alpha 1}$ line (10.55 keV) and lead $L_{\beta 1}$ line (12.61 keV) from lead-tin alloy nanoparticles (60% lead and 40% tin by mass) immobilized on an aluminum plate after detecting 100 nM DNA, where the two L peaks have different intensities due to difference in fluorescence yields.

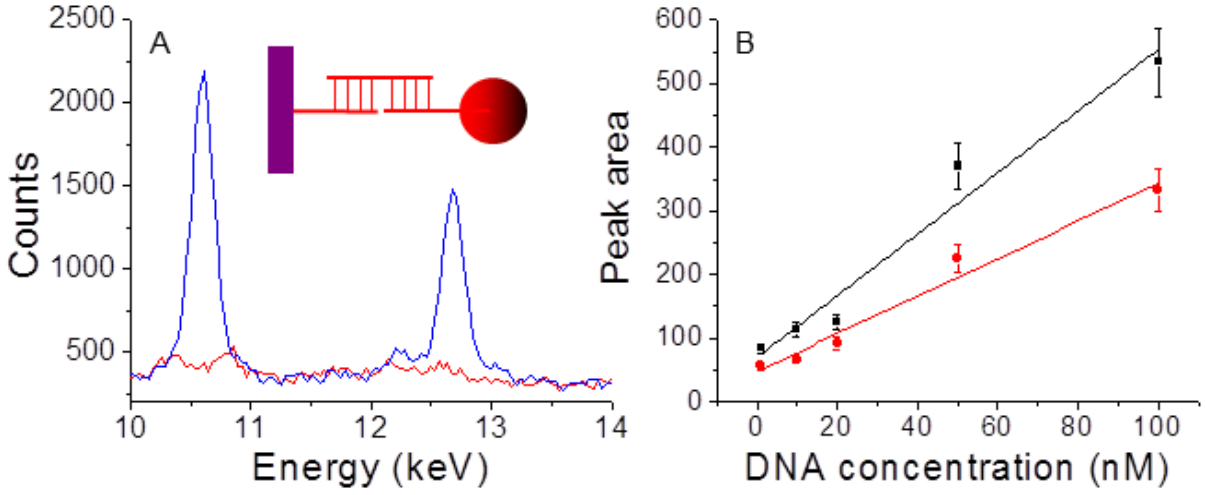

Figure 2-2 XRF spectrum of lead-tin alloy nanoparticles after detecting 100 nM ssDNA (A), where red and blue lines are background and signal, respectively; the peak areas of lead $L_{\alpha 1}$ (black) and $L_{\beta 1}$ (red) as a function of ssDNA concentration (B).

The intensity ratio of $L_{\beta 1}/ L_{\alpha 1}$ lines is determined to be ~0.7, which is close to the ratio of their fluorescence yields (~1.0).[20] The quantitative measure of target DNA concentration is obtained from the area under the XRF peaks after removing background. Figure 2-2(B) shows linear dependences of peak area on DNA concentration for both peaks in the range of 1 to 100 nM, which is obtained after removing background, and integrating area under each peak. The minimum concentration of ssDNA for which the XRF peaks are discernible above background is 1 nM. The top line (black) represents the area under the $L_{\alpha 1}$ peak and the bottom line (red) represents the area under the $L_{\beta 1}$ peak. The slope of each line is a measure of the detection sensitivity for the according L line, and is found to be higher for the larger $L_{\alpha 1}$ peak compared to the smaller $L_{\beta 1}$ peak. A similar method has been used to detect ssDNA using indium, tin or bismuth nanoparticles (not shown). Providing other conditions (nanoparticle diameter, collection time, X-ray flux, and detector-sample distance) are identical, lead-tin alloy and bismuth nanoparticles provide the highest detection sensitivities compared to other nanoparticles due to their higher fluorescence yields.

The sensitivity of detection can be enhanced by stacking substrates with immobilized nanoparticles, and detecting characteristic X-ray emissions in transmission mode. Simulated results are shown in Figure 2-3 for bismuth nanoparticles. Several aluminum plates that have immobilized bismuth nanoparticles after detecting DNA have been stacked on top of each other, forming layers, followed by X-ray exposure. Figure 2-3 inset shows intensity of $L_{\alpha 1}$ peak as function of the number of stacked aluminum plates when only four plates are used.

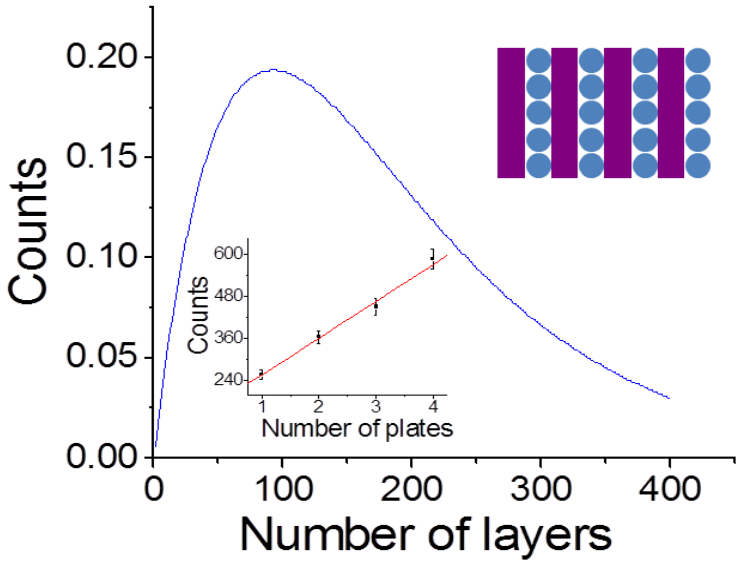

Figure 2-3 Intensity of bismuth $L_{\alpha 1}$ peak as a function of the number of layers of aluminum plates containing immobilized ssDNA conjugated with bismuth nanoparticles; four aluminum plates are stacked together to enhance signal intensity in transmission mode (inset).

A linear relation exists when total number of layers is four as shown in Figure 2-3 (inset). The limit on the number of stacking plates has been calculated according to the following: (1) X-ray absorbance by aluminum and bismuth nanoparticles is based on Lambert-Beer law, and (2) generation of characteristic X-ray emission is proportional to thickness (layers) of bismuth nanoparticles on aluminum plates. Assuming that primary X-ray beam is monochromic and has a uniform energy of 40 keV, the net intensity I of fluorescence emission can be derived using:

$$I = \omega . n(d_1+d_2).\exp\{- n (\mu_1 d_1+\mu_2 d_2)\}$$

where ω is fluorescence yield of bismuth $L_{\alpha 1}$ (0.37), n is number of stacking nanoparticle-aluminum layers, d and μ are thickness (or diameter) and total X-ray absorption coefficients of aluminum (1) and bismuth (2), respectively. The solid curve in Figure 2-3 shows simulated results, where the thickness of aluminum plate is 0.15 mm, the diameter of bismuth nanoparticles is 10 nm, and bismuth nanoparticles form a monolayer on the aluminum plate.

After reaching a certain maximum (80 stacked plates), the fluorescence emission decreases due to increased self-absorption and scattering of the secondary X-rays by the thicker layers of aluminum plates, meaning that the maximum number of layers will be 80, which corresponds to a sensitivity of 0.0125 nM for DNA detection.

Multiple ssDNAs have been detected using bismuth, lead-tin, tin, and indium nanoparticles at the same time, where an aluminum plate is modified with a mixture of four capture ssDNAs at equal amounts. Figure 2-4 shows characteristic XRF peaks of four different nanoparticles after detecting four types of target ssDNAs, where lead (10.55, 12.61 keV), bismuth (10.84, 13.02 keV), indium (24.21, 27.27 keV), and tin (25.27, 28.48 keV) can be distinguished from background

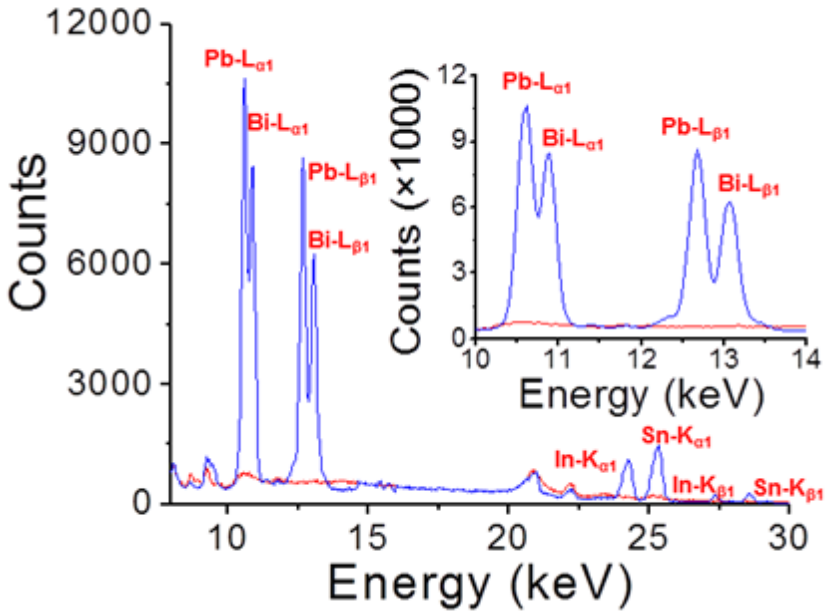

Figure 2-4 XRF spectrum of lead (10.55, 12.61 keV), bismuth (10.84, 13.02 keV), indium (24.21, 27.27 keV), and tin (25.27, 28.48 keV) nanoparticles after detecting four types of ssDNAs at concentrations of 100 nM , where the inset shows lead and bismuth L peaks at higher magnification, where bottom and top lines are background and signal, respectively.

The difference in fluorescence intensity is induced mainly by fluorescence yield, which is higher for elements with higher atomic number. The Si-PIN detector that can resolve 140-260 eV peak at 5.9 keV enables distinction of lead $L_{\alpha 1}$ and $L_{\beta 1}$ (10.55 and 12.61 keV) lines from bismuth $L_{\alpha 1}$ and $L_{\beta 1}$ lines (10.84 and 13.02 keV) as shown in Figure 2-4 (inset). Based on energy resolution of detector, and energy range of detection, the number of possible fluorescence peaks that can be detected will reach ~150, meaning that this method allows simultaneous detection of ~150 different peaks. On the other hand, the number of XRF peaks depends on how many different atoms are available in form of nanoparticles. From the periodic table, ~50 different types of elements could be made into nanoparticles with characteristic X-ray signatures, thus, the detection multiplicity of nanoparticle enabled XRF technique could reach ~50.

The feasibility of *in vivo* protein biomarker detection/imaging using XRF has been studied after immobilizing prostate specific membrane antigens (PSMA) onto substrates. Ligand-modified aluminum plates are immersed in PBS solutions containing antigen at pH 7.0 for 3 h; after washing plates with PBS (pH 7.0), the plates are immersed in PBS solution containing PSMA antibody modified bismuth nanoparticles for 3 h. After removing excess nanoparticles by washing, the plates with immobilized nanoparticles are analyzed by XRF. Figure 2-5 (A) shows the emission lines of bismuth (top) at 10.84 ($L_{\alpha 1}$) and 13.02 ($L_{\beta 1}$) keV above background (bottom), where difference in peak area is induced by difference in fluorescence yields. The areas of both peaks depend linearly on antigen concentration (Figure 2-5(B)), from which the detection limit for PSMA by using bismuth nanoparticles is 1 ng/ml.

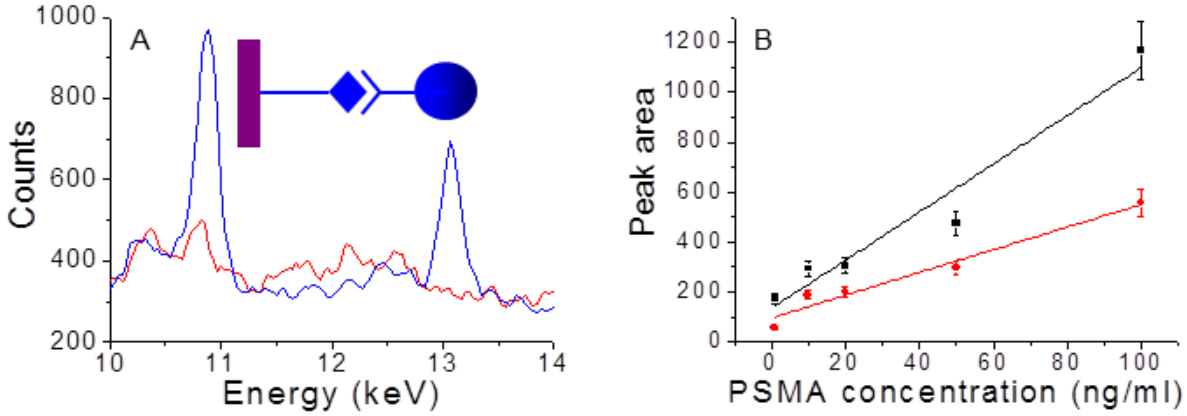

Figure 2-5 XRF spectrum of bismuth nanoparticles after detecting 100 ng/ml of protein biomarker (A), where bottom and top lines are background and signal, respectively; the peak areas of bismuth $L_{\alpha 1}$ (top) and $L_{\beta 1}$ (bottom) as a function of protein concentration (B).

The aluminum plates with DNA-linked bismuth nanoparticles have been coated with 10 mm thick polymethyl methacrylate (PMMA) in order to mimic tissues surrounding tumors. Figure 2-6 shows XRF peaks of bismuth exposed to 40 kV X-rays, where the signal intensity does not decrease appreciably after polymer coating and the peaks can still be identified easily.

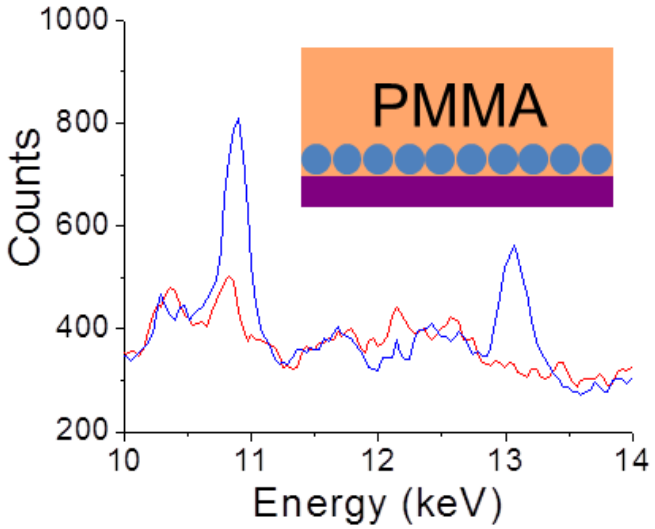

Figure 2-6 XRF spectrum of bismuth nanoparticles immobilized on aluminum plate with 100 ng/ml of protein biomarker and then covered with 10 mm PMMA.

Furthermore, XRF is used to image multiple biomarkers after immobilizing bismuth nanoparticles and lead nanoparticles on a plastic substrate. The patterned areas cover 20×20 mm^2 with 2 mm separation, and are coated with 10 mm thick PMMA as shown in Figure 2-7(left). The sample is mounted on an x-y translational stage. A two-dimensional scan is carried out at 1 mm step size by moving the sample in x-y direction. The peak intensities for bismuth (10.84 keV) and lead (10.55 keV) are recorded at each position and background is removed. Figure 2-7(right) shows the spatial distribution of net XRF intensities on a two dimensional space, where column height represents fluorescence counts after removing background.

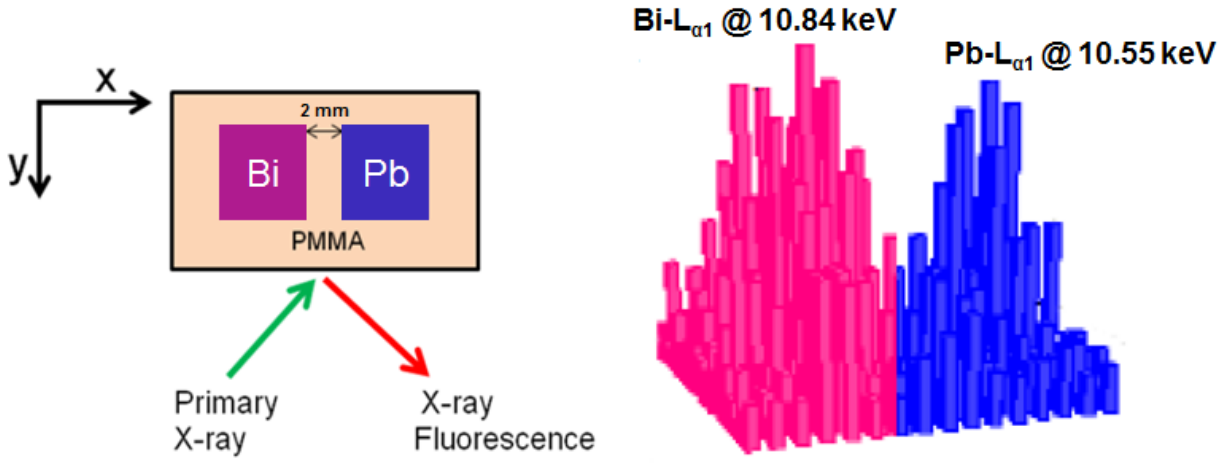

Figure 2-7 Setup for 2D image scan (left); spatially distributed intensities of two discrete areas on a plastic substrate covered with bismuth and lead nanoparticles (right).

Two distinct regions are identified with significant increase in fluorescence intensity, reflecting that X-ray beam hits on bismuth or lead region. In contrast to computed tomography (CT) where thickness contrast is considered, the energy resolving XRF can differentiate nanoparticles based only on the characteristic X-ray energies. This allows more scopes for

multiplexed imaging, and early detection of lethal cancers by indicating functional relation among biomarkers, and identifying biomarkers associated with different stages of disease.

X-ray dose is estimated by using PCXMC, a PC-based Monte Carlo simulation program, in which X-ray photons are followed as they randomly interact with phantoms according to probability distribution of processes such as photoelectric absorption, coherent (Rayleigh) or incoherent (Compton) scattering.[21] This produces a large number of independent photon histories from which the mean values of energy depositions can be estimated and used to calculate doses. A total of 20,000 photon histories have been generated at tube voltage of 40 kV. The thicknesses of silver target and beryllium window are 1.5 and 500 μm, respectively. The anode angle and focus-sample distance are taken as 13°, and 3.0 cm, respectively. The beam width and height of collimated beam are taken as 2 mm. The current-time product of 1.8 mAs is obtained at tube current (15 μA) and exposure time (120 s). In case only beryllium window is used as filter, the Monte Carlo simulation in PCXMC results in a total body dose of 0.47 μGy and an effective dose of 0.72 μGy for an average adult (70 kg). These are lower than the average radiation doses in regular medical procedures such as an abdominal X-ray (1.4 mGy) or an abdominal CT scan (8.0 mGy).

2.4 Conclusion

This method has the potential to detect multiple cancer biomarkers inside human body. Nanoparticles with suitable surface modifications can be taken into body, and conjugated onto tumors through antigen-antibody interaction. The penetrating power of incoming X-rays can be

tuned by using beams of higher energy. The dose absorbed by the body can be further reduced by using monochromatic beams or beams with less background by appropriate filtration. By quantitatively imaging multiple surface biomarkers of cancer cells, the reliability of *in vivo* cancer detection can be hopefully enhanced without much harmful effects on humans. The technique can also be applied for the detection of circulating DNA in blood that is responsible for cancer metastasis.

CHAPTER 3: X-RAY RADIATION ENABLED DETECTION AND ERADICATION OF CIRCULATING TUMOR CELLS WITH NANOPARTICLES

3.1 Introduction

Detecting circulating tumor cells (CTCs) released into the blood stream of patients during cancer development could provide a sensitive and minimally invasive way to monitor cancer progression.[22-25] But, it is challenging to detect CTCs in blood, because CTCs in early-stage cancer patients are extremely rare (1 CTC in 7.5 ml of blood or 1 CTC against 10^3-10^7 nucleated cells in blood).[26] An enrichment step is required prior to CTC detection.[27-28] Many techniques have been used for CTC enrichment such as microfluidic CTC chips,[29-32] magnetic particles,[33-35] microfiltration,[36-38] dielectric separation,[39] and flow cytometry.[40-42] These methods are dependent on physical properties of tumor cells (size, mechanical stiffness, or dielectric property), or surface receptors over-expressed on tumor surfaces. Once collected, CTCs can be detected with fluorescence method,[43-44] photoacoustic method,[45-48] electrical method,[49] flow cytometry, cell counting, and Raman spectroscopy.[50-52] Though these methods have shown the prospects of CTCs in cancer management, existing CTC techniques are limited for few reasons: (1) CTC numbers detected by different methods vary drastically from several to several hundred, which can be partly due to tumor heterogeneity in patient and complex nature of blood, but is more likely due to variation in collection or detection efficiency of different methods; (2) CTC detection has not been seamlessly integrated with treatment, thus patients will have to wait for certain time before treatment starts, which can lead to tumor metastasis to distant organ; (3)

chemotherapy is often used for CTC treatments, but drugs used in chemotherapy are toxic to normal cells, and there is no localized treatment option available for CTCs. If CTCs could be killed locally and non-invasively, damage to normal cells will be minimized, and there is no need to use invasive treatments such as surgery. Nanostructured materials (i.e., golden carbon nanotubes and magnetic nanoparticles) have been used in combination to capture and detect CTCs, but the method needs complicated photoacoustic devices for CTC detection, and tumor killing is not integrated.[45] CTC detections have also been achieved *in vivo* using flow cytometry after labeling CTCs with fluorescent probes that target surface receptors of CTCs,[30] but the method does not take CTC removal or elimination into consideration.

X-ray fluorescence (XRF) has been used to detect multiple DNA and protein biomarkers by using metallic nanoparticles as probes.[53] XRF spectrometry is a widely used analytical method for detecting trace elements in various samples due to its high sensitivity, specificity and simplicity.[54-55] The characteristic X-ray emissions from elements, present in the X-ray irradiated samples, are detected using an X-ray spectrometer. The amount of each element present in the sample can be quantified based on the intensity of according XRF peak or by calculating the area under the peak after removing background. Bismuth nanoparticles are promising candidates for biomarker detection, cancer imaging and therapy due to bismuth's large atomic number (Z = 83) and relatively low toxicity.[56] Meanwhile, superparamagnetic iron oxide nanoparticles are well known for their enrichment capability and biocompatibility and have been widely applied in detection of rare analytes.[57] This work describes an integrated *in-vitro* method that can also be used for *in vivo* CTC management by combining magnetic nanoparticle based capture, XRF based detection and X-ray radiation killing of CTCs. The feasibility of this integrated approach

has been confirmed in this proof-of-concept *in vitro* experiment: superparamagnetic iron oxide nanoparticles and X-ray absorbing bismuth nanoparticles are modified by folic acid (FA) ligands that bind to folate receptors (FR) over-expressed on tumor cell surfaces; after adding both nanoparticles in cell suspension, nanoparticles can bind specifically on surfaces of tumor cells; a micro-magnet allows localization of CTCs in a small area (preferentially underneath the skin in case of *in vivo* detection); an incoming X-ray beam excites the characteristic X-rays of bismuth nanoparticles, signaling the presence of CTCs; subsequently, X-ray intensity can be increased to damage DNA of CTCs and kill CTCs locally as shown in Figure 3-1

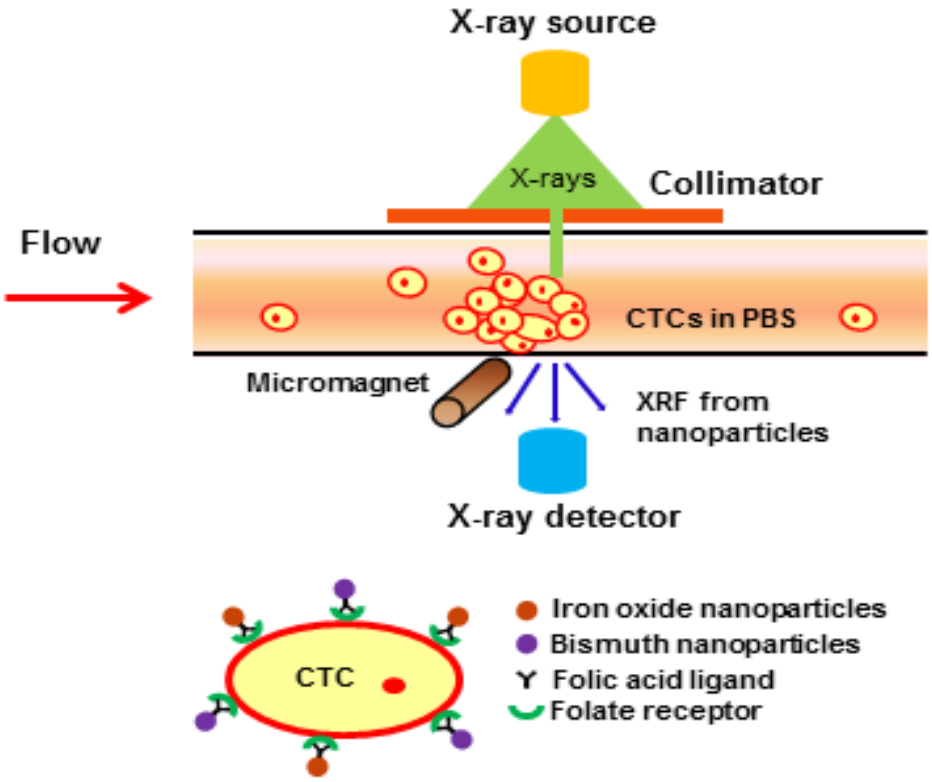

Figure 3-1 Nanoparticle enabled integrated enrichment, detection and killing of circulating tumor cells.

3.2 Experimental Section

HeLa (CLL-2) and MG-63 (CRL-1427) cell lines are obtained from American Type Culture Collection (ATCC, Manassas,VA).3-(4,5-dimethylthiazol-2-yl)-2,5-diphenyltertrazolium bromide (MTT) kit for mammalian cells is supplied by Invitrogen (Carlsbad, CA). Single donor human whole blood containing anticoagulant of ethylenediaminetetraacetic acid (EDTA) is obtained from Innovative Research (Novi, MI). FA is obtained from VWR (West Chester, PA). Hydrated bismuth nitrate ($Bi(NO_3)_3 \cdot 5H_2O$), sodium borohydride ($NaBH_4$), RPMI 1640 culture media, penicillin, streptomycin, fetal bovine serum (FBS), and Dulbecco's phosphate-buffered saline (D-PBS) are from Sigma-Aldrich (St. Louis, MO). Ultrapure water (18.2 $M\Omega cm^{-1}$) from Nanopure System (Barnstead, Kirkland, WA) is used throughout. All the other chemicals are obtained from VWR (West Chester, PA) and used as received.

3.2.1 Synthesis of Nanoparticles

Iron oxide nanoparticles are synthesized as follows: 1 mmol of $Fe(acac)_3$ and 4 mmol of 1,2-dodecanediol are dissolved into a mixture of 10 ml of benzyl ether, 3 ml of oleic acid and 1 ml of oleylamine. The mixture is then dehydrated at 110 °C under argon flow for 1 h, and heated up to 200 °C for 30 min, and at 290 °C for 2.5 h. After cooling to room temperature, 30 ml of anhydrous ethanol is added in the mixture to separate nanoparticles. The nanoparticles collected by centrifugation (7000 rpm, 10 min) are washed with ethanol and dispersed in hexane. After precipitated with acetone, the nanoparticles are dispersed in 1 mol/l ammonia in isopropanol,

sonicated for 30 min, centrifuged, and washed with acetone, toluene and ethanol to remove oleic acid and oleylamine.

Bismuth nanoparticles are made as follows: 0.1 mmol of Bi $(NO_3)_3$ and 0.5 mmol of poly (vinylpyrroldone) (PVP) are dissolved in 10 ml of N,N-dimethylformamide (DMF). The mixture is degassed with argon for 15 min under stirring. 0.3 ml of 1 mol/l $NaBH_4$ in water is mixed with 10 ml of DMF and added in the mixture of $Bi(NO_3)_3$ and PVP under vigorous stirring and argon flow for 5 min. The nanoparticles are precipitated by adding acetone, followed by centrifugation, washing with acetone and drying in vacuum. A JEOL 1011 transmission electron microscope (TEM) operated at 100 kV is used to derive the size and shape of the synthesized nanoparticles.

3.2.2 Conjugation of Nanoparticles with Folic Acid

The conjugation of FA with iron oxide nanoparticles and bismuth nanoparticles is carried out as follows:[58] both nanoparticles are washed twice in ethanol, centrifuged, dried at 110 °C for 1 h, and vacuum-dried overnight to remove adsorbed water. 15 mg of dried nanoparticles are dispersed in 3 mmol/l of (3-aminopropyl)-triethoxysilane (APTES) in 5 ml toluene. The mixture is sonicated and incubated at 60 °C for 4 h. The suspension is centrifuged, and the precipitates are sonicated in toluene for 10 min, and washed with toluene and ethanol. The precipitates are then added to the mixture of 1 ml of 10 mmol/l FA solution in 500 µL of dimethylsulfoxide (DMSO), 1.5 ml of 15 mmol/l N-hydroxysuccinimide (NHS), and 1.5 ml of 75 mmol/l 1-Ethyl-3-(3-dimethylaminopropyl) carbodiimide (EDC) solution in water, using triethylamine as a catalyst. After adjusting pH to 9 and incubation at 37 °C for 4 h, the suspension is

centrifuged, and precipitate is washed with deionized water and vacuum-dried overnight. FA-modified nanoparticles are redispersed in PBS to 1 mg/ml, and stored in refrigerator. The hydrodynamic diameter of FA conjugated nanoparticles in PBS is measured by dynamic light scattering (DLS) with PD2000 DLS detector. The covalent bonding of FA with the nanoparticles is confirmed using Fourier transform infrared spectroscopy (FTIR).

3.2.3 Cell Culture and Nanoparticles Treatment

Human adenocarcinoma HeLa cells and human osteosarcoma MG-63 cells are cultured in 75 cm^2 flasks that contain 15 ml RPMI-1640 medium supplemented with 10% FBS and 5% penicillin at 37 °C with 5% CO_2. When cells become 80% confluence, an equimolar mixture of 100 μg/ml of FA-conjugated iron oxide nanoparticles in PBS (~10^{13} particles/ml) and 100 μg/ml of FA conjugated bismuth nanoparticles in PBS (~10^{11} particles/ml) is added to the petri dish containing the cultured cells (~1×10^5). After incubating for 24 h (37 °C and 5% CO_2), the cells are rinsed five times in PBS to remove any unbound or non-specifically bound nanoparticles. The cells are then detached from flasks by incubating with trypsin-EDTA solution at 37 °C for 5 min, followed by centrifugation at 1000 rpm for 8 min, before being redispersed in PBS and introduced into an *in vitro* circulating system designed to mimic human blood flow.

3.2.4 Setup for CTC Capture, Detection and Killing

A Mini-X X-ray tube (Amptek, Bedford, MA) with a silver anode operating at 30 kV and 15 μA is used to produce primary X-rays. The tube is fitted with a series of brass and tungsten collimators to reduce outgoing beam size from 2 mm to 400 μm in diameter. An X-ray spectrometer (Amptek X-123) with Si-PIN photodiode is used to analyze XRF emissions in the transmission mode. The X-ray spectrometer contains a solid-state detector, a digital pulse processor and a multichannel analyzer, which are interfaced with a computer for data acquisition and analysis. A 25 μm thick silver filter and a 250 μm thick aluminum filter are used in combination to reduce background and improve signal-to-noise ratio (SNR) in low energy region (0-15 keV) of the XRF spectrum. A neodymium-iron-boron micro-magnet obtained from BJA Magnetics (Leominster, MA) with diameter of 300 μm, length of 2.5 mm and field strength of 0.5 mT is attached onto one side of a polyethylene tube of 1 mm inner diameter. The distance between X-ray source and the tube, and that between the tube and detector are 2 and 1 cm, respectively. HeLa cells ($\sim 1\times10^5$) containing FA conjugated bismuth nanoparticles and FA conjugated iron oxide nanoparticles at a nanoparticle concentration of 100 μg/ml are dispersed in 1 ml of PBS. The cell-nanoparticle conjugates are pumped through the tube with a pump at a pulsatile flow rate of 0.1 cm/s (close to that in human body), and are captured by the micro-magnet on the internal wall of tube just underneath the X-ray source. The captured CTCs are exposed to X-rays for 10 min. The XRF peaks from bismuth nanoparticles at 10.84 and 13.02 keV are used to determine the presence of CTCs. The XRF emissions from iron oxide nanoparticles are not used for CTC detection, because the magnet attached to the side of the tube

also gives off characteristic iron peaks in the XRF spectrum. To kill captured HeLa cells through radiation induced DNA damage, the X-ray dose is increased by increasing the exposure time to 60 min and the tube voltage to 40 kV. A photograph of the whole setup is shown in Figure 3-2:

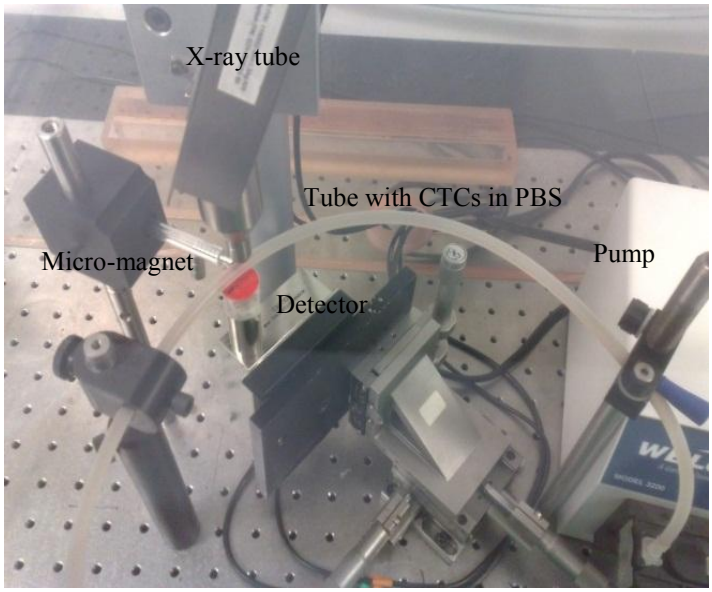

Figure 3-2 Setup for CTC enrichment, detection and killing using X-rays and nanoparticles.

To evaluate the performance of our method in detecting CTCs in whole blood, the flowing PBS is replaced with human blood spiked with HeLa or MG-63 cells at a concentration of 10^4 cells/ml. The cultured cells have been incubated for 24 h with FA conjugated bismuth nanoparticles and iron oxide nanoparticles at a nanoparticle concentration of 100 μg/ml followed by PBS wash for five times before adding to the whole blood. The spiked blood samples are diluted (10x) with PBS to ensure a steady flow inside the tube by preventing any agglomeration or coagulation. The captured cells are exposed to X-rays for 10 min at 30 kV and 15 μA and XRF counts for the bismuth peak at 10.84 keV are recorded. To serve as control, a background spectrum is also collected using only diluted blood samples.

3.2.5 Comet Assay

In order to test DNA damage, X-ray irradiated HeLa cells in 1 ml of 1X PBS are added into 2% low melting point agarose at a 1:1 volume ratio at 37 °C. 300 μL of the cell-agarose suspension is dropped onto each of three 4×3 cm^2 GelBond slides and allowed to settle at 37 °C for 10 min. The agarose is solidified by placing GelBond slides at 4 °C for 10 min. The irradiated cells are lysed by immersing slides in lysis buffer (10 mmol/l Tris-HCl, 100 mmol/l Na_2EDTA, 2.5 mol/l NaCl, 1% Triton X-100) at pH 10 and 4 °C for 1 h. The slides are placed in an electrophoresis chamber filled with alkaline buffer (0.3 mol/l NaOH and 1 mmol/l Na_2EDTA) for 40 min. The electrophoresis is carried out for 30 min by applying an 18V dc voltage across the chamber at 1 V/cm and 300 mA. Short strands of damaged DNA diffuse out of cells and migrate towards the anode. The slides are neutralized twice for 10 min in fresh buffer (0.4 mol/l Tris-HCl at pH 7.5) and stained with 5 μg/ml of ethidium bromide (EB) aqueous solution for 30 min. The EB-labeled cells on GelBond slides are observed with epi-fluorescence microscope (Olympus BX51M) at magnification 10X and images are recorded using a computer. Images of over 100 randomly selected non-overlapping cells are analyzed for each sample using CometScore software (TriTek Corp., Sumerduck, VA).

3.2.6 MTT Assay

X-ray irradiated HeLa cells are transferred into the microwells of a 96-well sterile microplate (BD Falcon) containing 100 μL of media. After incubation for 24 h, the medium in each well is removed and replaced with 100 μL of fresh culture medium. 10 μL of the 12 mmol/l

MTT stock solution is added in each well and into a negative control (100 μL of medium without nanoparticles). After incubation at 37 °C for 4 h, 100 μL of sodium dodecyl sulfate–hydrochloric acid solution is added and mixed thoroughly using pipette. After incubating at 37 °C inside a humidified chamber for 6 h, each sample is mixed with pipette and optical absorbance at 570 nm is recorded.

3.2.7 Statistical Analysis

Seven independent experiments (n = 7) have been carried out for each data set and the results are expressed as mean ± standard error of the mean (SEM). Statistical analyses were performed using SPSS 16.0 (SPSS Inc, Chicago, Illinois). One-way analysis of variance or ANOVA and least significance difference or LSD tests were applied to compare the results from samples treated by different methods. $p < 0.05$ was considered statistically significant.

3.3 Results and Discussions

3.3.1 Nanoparticle Characterization

Figure 3-3A and 3-3B are the TEM images of nanoparticles made using colloidal methods, where the average diameters of bismuth nanoparticles (Figure 3-3A) and iron oxide nanoparticles (Figure 3-3B) are 30 and 10 nm, respectively.

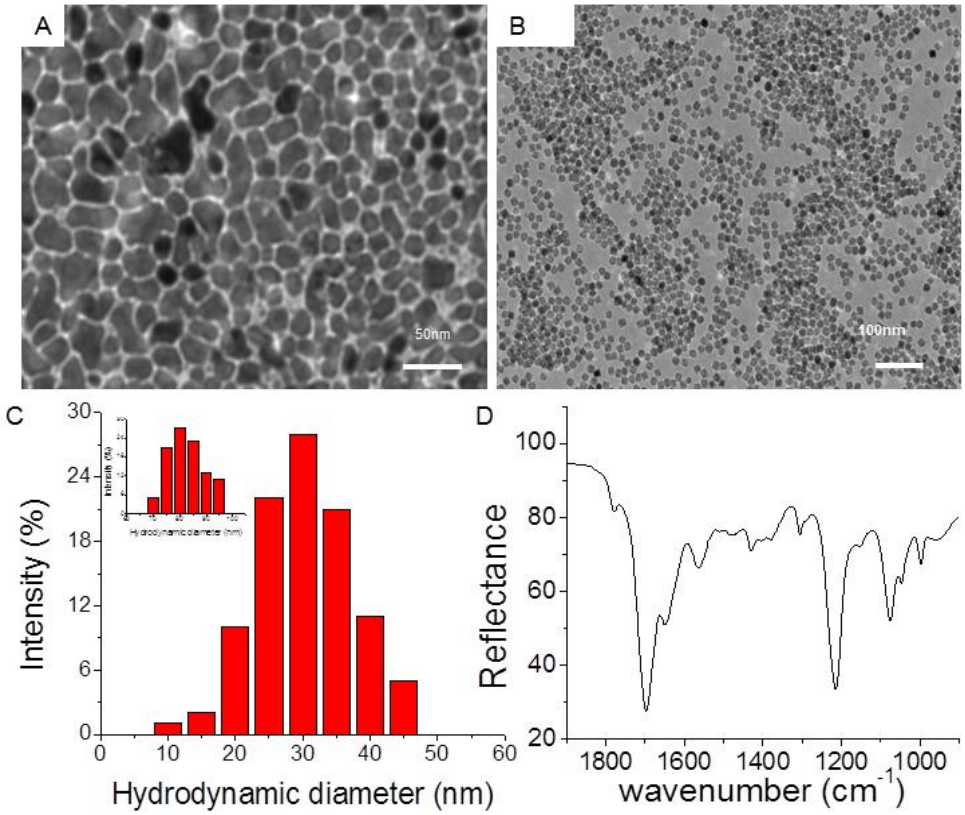

Figure 3-3 Characterization of nanoparticles. TEM images of bismuth nanoparticles (A) and iron oxide nanoparticles (B); DLS measurements of iron oxide nanoparticles in PBS (inset shows bismuth nanoparticles in PBS) (C); FTIR spectrum of bismuth nanoparticles after conjugation with folic acid (D).

Figure 3-3 C shows DLS measurements from FA conjugated iron oxide nanoparticles in PBS with a size range of 10-45 nm and a mean hydrodynamic diameter of 30 nm. Figure 3-3 C inset shows FA conjugated bismuth nanoparticles in PBS with a size range of 70-95 nm and a mean hydrodynamic diameter of 80 nm. These results demonstrate that nanoparticles form small agglomerates, which are uniformly distributed in PBS. The FTIR spectrum in Figure 3-3D for FA conjugated bismuth nanoparticles shows the presence of C-N peak (1000-1250 cm^{-1}) and NH_2 scissoring peaks (1550-1650 cm^{-1}), indicating successful conjugation of FA with bismuth

nanoparticles. The conjugation of FA with iron oxide nanoparticles has also been confirmed (data not shown) using FTIR.

3.3.2 CTC Capture and Detection

Figure 3-4 shows the XRF spectrum from magnetically captured HeLa cells (~1×10^5 cells/ml PBS) after exposure to X-rays for 10 min at 30 kV and 15 µA, where the peaks of bismuth L-subshell (red) from bismuth nanoparticles can be detected at 10.84 and 13.02 keV against background (black) with a SNR of ~5 and 2.5 respectively.

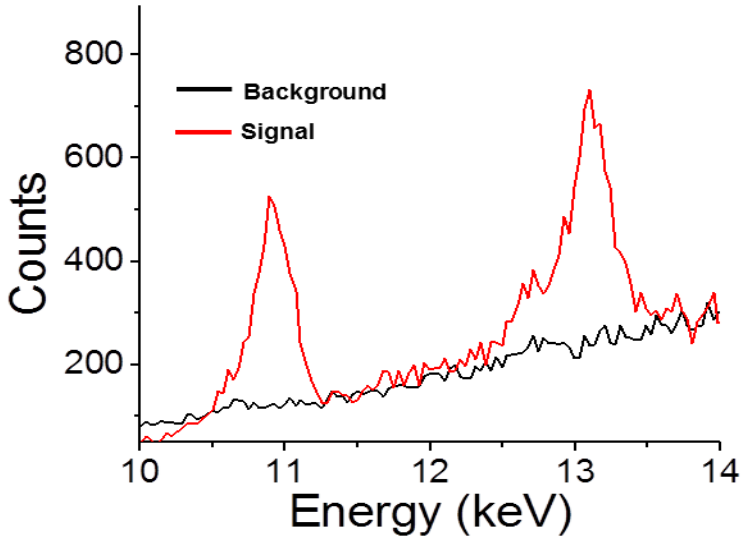

Figure 3-4 XRF spectrum obtained at 30 kV and 15 µA after 10 min exposure of magnetically captured HeLa cells with folic acid conjugated iron oxide nanoparticles and bismuth nanoparticles.

The targeting specificity of FA conjugated nanoparticles is confirmed by measuring XRF intensity of bismuth for HeLa cells and MG-63 cells. Both cell lines, after incubating with FA

conjugated nanoparticles and unmodified nanoparticles, are washed five times in PBS followed by 10 min X-ray exposure at 30 kV and 15 μA. Figure 3-5 shows XRF counts for the bismuth peak at 10.84 keV.

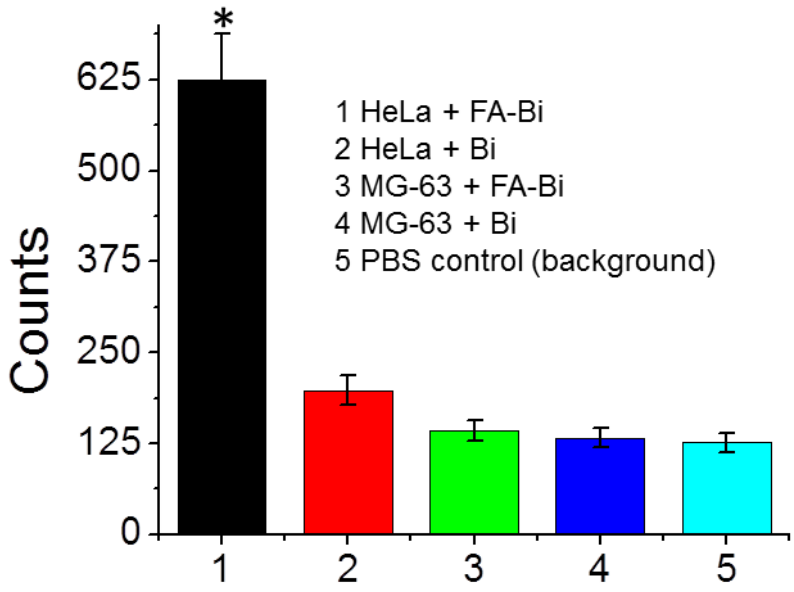

Figure 3-5 Bismuth XRF peak intensity at 10.84 keV of unmodified bismuth nanoparticles (Bi) and folic acid modified bismuth nanoparticles (FA-Bi) combined with HeLa cells and MG-63 cells , * denotes $p < 0.05$ when compared with PBS control.

HeLa cells combined with FA conjugated bismuth nanoparticles have the strongest XRF peak while HeLa cells with unmodified bismuth nanoparticles give off signal close to background (PBS control). This confirms that FA conjugated bismuth nanoparticles can combine with FRs on surface of HeLa cells through strong covalent bonds while unmodified nanoparticles are easily removed after PBS wash. To justify whether FA conjugated bismuth nanoparticles can combine with other cells, MG-63 cells are taken as a second control because of their low level of FR expression compared to HeLa cells. Results show that XRF counts from MG-63 cells, with both FA conjugated bismuth nanoparticles and unmodified bismuth nanoparticles, are at similar

level as the background obtained from PBS solution. This confirms that FA conjugated nanoparticles only combine with those cancer cells that over-express FRs.

The sensitivity of detection is obtained by measuring XRF signals for serially diluted CTC samples (varied from 10^2, 10^3, 10^4, 10^5 CTCs/ml) in PBS. The measured XRF signals at 10.84 keV are plotted as a function of the number of CTCs per ml of PBS. Figure 3-6A reveals that the detection sensitivity is ~100 CTCs/ml PBS for 40 min X-ray irradiation at 30 kV and 15 µA.

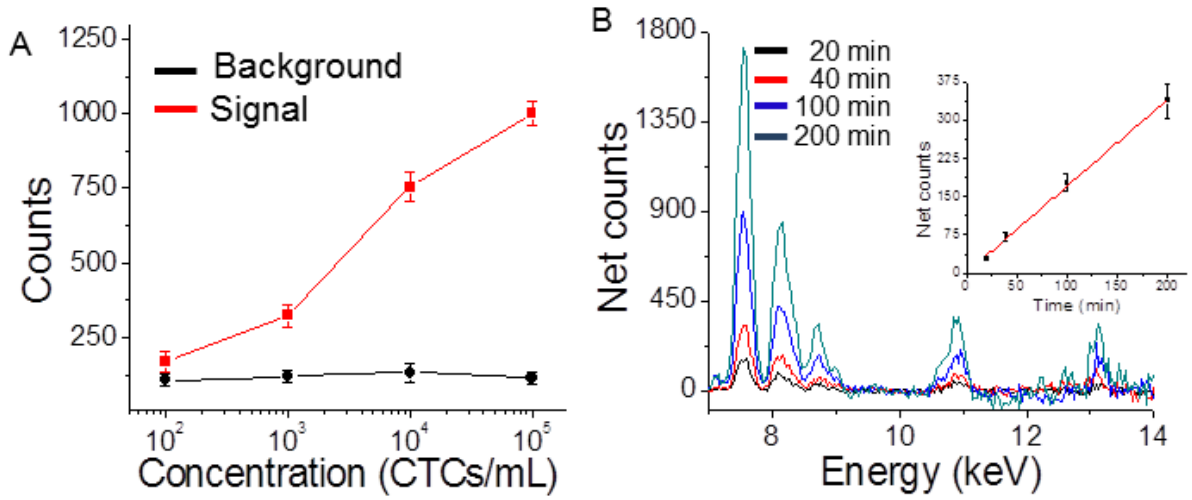

Figure 3-6 XRF counts for bismuth peak at 10.84 keV as a function of the number of CTCs in 1 ml PBS (A); Net XRF spectrum for HeLa cells conjugated with folic acid modified bismuth nanoparticles collected at 20, 40, 100 and 200 min using 30 kV and 15 µA (B) where inset shows the linear relation between net counts and the collection time.

The sensitivity can be further improved by increasing the exposure time. Figure 3-6B shows the net XRF spectra (background removed) collected from HeLa cells (~1×10^2 cells/ml PBS) combined with FA conjugated nanoparticles for 20, 40, 100 and 200 min exposures, respectively. Net counts at 10.84 keV are seen to increase linearly with increase in detection time

(Figure 3-6B inset).The sensitivity can also be enhanced if incoming X-rays can be precisely focused onto the captured CTCs and outgoing X-rays can be oriented in-line with the detector.

The feasibility of the proposed method for clinical applications has been tested using human blood spiked with CTCs. Results show that the XRF counts of bismuth at 10.84 keV for diluted blood sample is ~150 (background), while the corresponding values for blood samples spiked with MG-63 cells and HeLa cells are ~180 and ~550, respectively as shown in Figure 3-7.

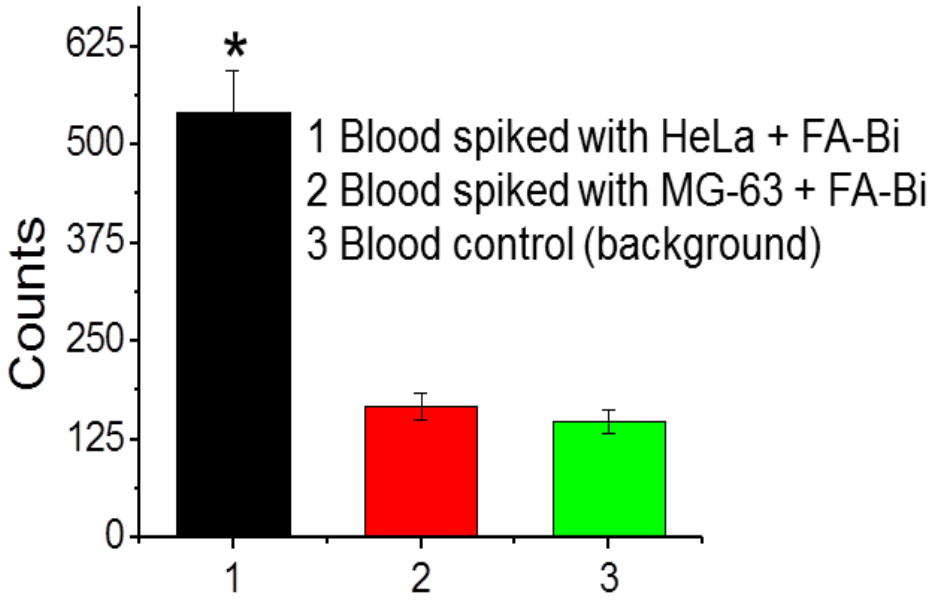

Figure 3-7 XRF counts at 10.84 keV for whole blood, blood spiked with 10^4 MG-63 cells/ml, and 10^4 HeLa cells/ml, where both types of cell contain folic acid conjugated bismuth nanoparticles and iron oxide nanoparticles.* denotes $p < 0.05$ when compared with blood control.

Although, the blood samples were spiked with high concentration of CTCs (10^4 cells/ml), the results clearly indicate the promising capabilities of the method in selectively detecting CTCs with high levels of FR expressions in whole blood.

3.3.3 CTC Killing Through Radiation Induced DNA Damage

Nanoparticles of high atomic number elements can enhance radiation-induced damage when specifically attached on or internalized into tumor cells. Specifically targeted gold nanoparticles can achieve a nucleus dose enhancement factor of up to 79 and localize ionizing energy at tumor cells, causing irreversible DNA damages that can eventually lead to cell death.[59-61] Comet assay is often used to quantify DNA damage by providing complementary damage information to those provided by conventional viability assays (MTT).[62-63] The combined effect of bismuth nanoparticles and X-rays on DNA damage is studied using comet assay on magnetically captured, and X-ray irradiated HeLa cells. Since the total photoelectric absorption cross-section of iron for 40 kVp X-rays is ~4 times lower than that of bismuth, the effect of iron oxide nanoparticles on X-ray induced DNA damage can be ignored. Figure 3-8A shows an optical image of comets from X-ray irradiated (60 min at 40 kV and 100 μA) HeLa cells that have been incubated with a mixture of functionalized iron oxide nanoparticles and bismuth nanoparticles at 100 μg/ml for 24 h prior to X-ray exposure. The presence of long tails means significant DNA damage.

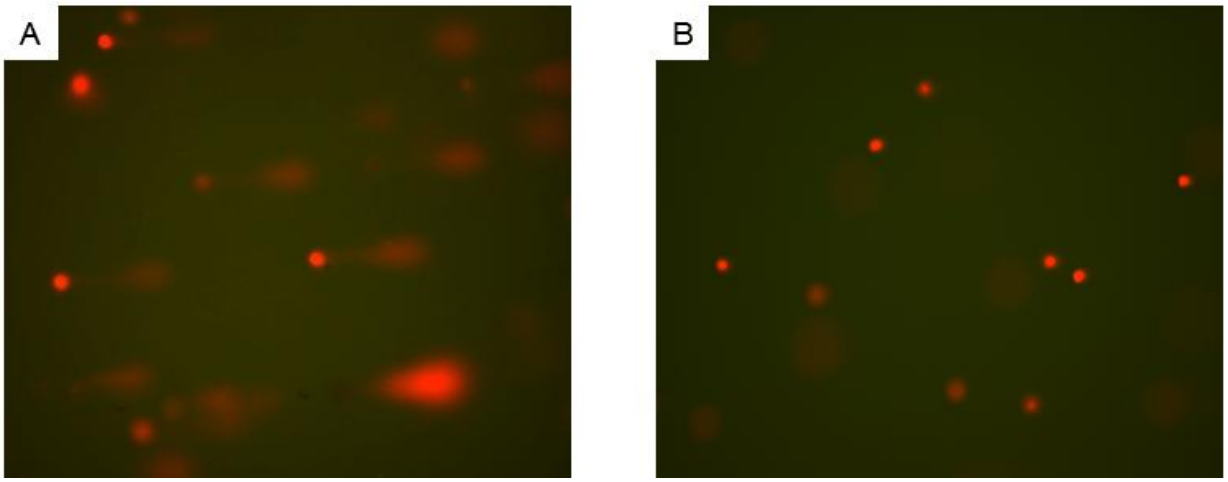

Figure 3-8 Optical micrograph of comets from X-ray irradiated HeLa cells containing folic acid conjugated iron oxide nanoparticles and bismuth nanoparticles using 40 kV and 100 µA X-rays for 60 min (A); Optical micrograph of comets from HeLa cells with folic acid conjugated iron oxide nanoparticles and bismuth nanoparticles without X-ray exposure (B).

Three sets of control samples are also tested. In the first set, HeLa cells without nanoparticles are exposed to X-rays followed by gel electrophoresis at the same condition. Tails are observed in the resulting comets (not shown) after doing the comet assay. For the second control, HeLa cells are used that contain a mixture of functionalized nanoparticles but are not exposed to X-rays. Figure 3-8B shows the absence of DNA tails from such cells after electrophoresis, suggesting that DNA damage is primarily due to X-rays and not the nanoparticles. Third set of control samples contain untreated HeLa cells without any nanoparticles or X-ray exposure. DNA damage in each sample is quantified by determining the percentage of DNA in tail (damaged) and those in entire comet (total), where the amount of DNA is derived as summation of pixel intensities in the tail or the entire comet.

Figure 3-9A compares the level of DNA damages in HeLa cells, where the percentages of DNA in tails are 82.1% with X-rays and nanoparticles, 63.9% with X-rays alone, 16.9% with

nanoparticles alone, and 10.1% with untreated control. In most cases, the X-ray induced DNA damages are irrecoverable, eventually leading to cell death as confirmed by other viability assays. For each set of HeLa cells mentioned above, MTT assay is carried out after incubation for 6 h following X-ray irradiation. This is done in order to confirm cell death induced by DNA damage.

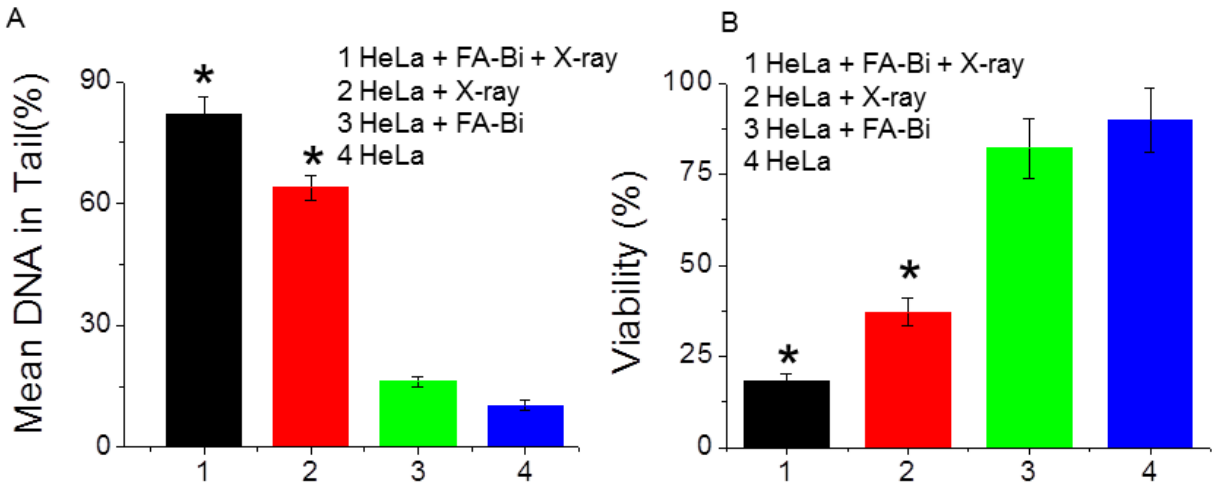

Figure 3-9 Mean percentage of DNA in the tail of comets under different conditions (A), * denotes p <0.05 when compared with untreated control (HeLa cells); Results of MTT assay performed on HeLa cells under different conditions (B). * denotes p <0.05 when compared with untreated control (HeLa cells).

Figure 3-9B shows the results of MTT tests where more than 80% of HeLa cells, which combined with FA conjugated nanoparticles, are killed when exposed to X-rays for 60 min at 40 kV and 100 μA; however, only about 60% HeLa cells are killed when no nanoparticles is used, suggesting the dose enhancement is provided by the X-ray absorbing nanoparticles. As for HeLa cells treated with functionalized bismuth nanoparticles but not exposed to X-rays, less than 25% cells are killed. Meanwhile, only 20% HeLa cells are dead in the untreated control. The MTT

results are consistent with those from comet assay, indicating that X-rays can effectively kill captured CTCs, which can be enhanced in presence of bismuth nanoparticles..

3.4 Conclusion

An integrated approach that combines *in vitro* collection, detection and killing of CTCs using bismuth nanoparticles, iron oxide nanoparticles and X-ray radiation have been demonstrated. The method uses FA modified nanoparticles for selectively targeting CTCs with high levels of FR expression and offers detection capabilities as low as 100 cells/ml in a buffer solution. The detection limit can be further improved by increasing the collection time or by using X-ray focusing optics and appropriate filters to reduce background noise and increase SNR. Use of X-rays allows simultaneous detection and eradication of CTCs, thus, providing a novel strategy for management of cancer metastasis.

Results clearly show the potential use of the technique for selective detection and on-demand killing of CTCs in whole blood, indicating future clinical applications. However, several issues need to be considered before the method can be put to clinical use. Inherent toxicities and aggregation of both iron oxide nanoparticles and bismuth nanoparticles under *in vivo* conditions are needed to be reduced with appropriate surface coatings. For example, FA conjugated iron oxide nanoparticles that are modified with dextran and poly (ethylene glycol) (PEG), have shown enhanced stability and biocompatibility.[64] Issues such as the circulation time of these nanoparticles and their excretion from the body should be studied using particles with different size and surface properties. In addition, appropriate tuning of X-ray parameters such as

beam energy, filtration and exposure times are necessary to minimize radiation damage to normal cells and alleviate patient sufferings. Future studies will focus on the effectiveness of the proposed method under *in vivo* conditions using mice experiments.

CHAPTER 4: CYTOTOXICITY OF BISMUTH NANOPARTICLES

4.1 Introduction

Being considered as one of the least toxic heavy metal, bismuth has been widely used in industry, biological and medical sciences. Bismuth compounds are most commonly used for treating gastrointestinal disorders,[65] eradication of Helicobacter pylori in peptic ulcers,[66-68] treatment of syphilis and tumors,[69] reduction of the renal toxicity of cisplatin.[70] Recently, bismuth nanoparticles have drawn great attention in biological sciences such as bioimaging,[56, 71] biosensing,[72] biomolecular detection,[73-74] and X-ray radiosensitizing.[53] The increasing biological applications promote serious concerns about the toxicity of bismuth nanoparticles, due to their small size and intimate contact with cellular components such as plasma membrane, organelles, DNA and proteins. Thus, the cytotoxicity of bismuth nanoparticle should be extensively and carefully addressed before their further biological applications. For instance, the toxicity of gold (Au) and iron oxide (Fe_3O_4) nanoparticles are well established and are generally considered non-toxic or less toxic and can be used directly; while cadmium selenide (CdSe) semiconductor nanoparticles are moderately toxic and have to be surface-modified to reduce the toxicity by minimizing direct contact with cellular components or reducing the release of toxic cadmium ions (Cd^{2+}).[75]

Due to the intimate contact with cells or tissues *in vivo*, the cytotoxicity of nanoparticles are largely determined by the physical property of these nanoparticles, such as atomic number, particle diameter, and surface modifications. The use of various surface modification techniques

to decrease nanotoxicity is the goal of nanotoxicity researches.[76-78] Nanoparticles with positively charged surfaces can enter cell membrane and cause cell damage due to strong electrostatic interactions. For *in vivo* applications, nanoparticles are modified with neutral polymers such as polyethylene glycol (PEG) in order to reduce damage to cells while enhancing circulation time in bloodstream.[79] Meanwhile, silica modified nanoparticles have shown low toxicity levels in both *in vivo* and *in vitro* experiments.[80-82]

Previous studies have revealed that several mechanisms are responsible for nanoparticle-induced cellular damage.[83-84] Generation of reactive oxygen species (ROS) is the dominant mechanism of cellular damage for most nanomaterials due to their higher chemical reactivities. Release of metal ions from nanoparticle dissolution is another important mechanism for toxicity of some nanoparticles (eg. Ag, CdTe, CuO).[85-88] Inhibiting the DNA repair by displacement of zinc ions (Zn^{2+}) from the zinc finger protein of DNA repair enzymes also leads to increased DNA damage.[89] Multiple cytotoxicity assays (such as membrane integrity, enzyme activity, reproduction capability, and DNA damage) are needed to elucidate these mechanisms mainly because these toxicity assays always give inconsistent toxicity results due to their unique detection principles. For instance, 3-(4,5-dimethylthiazol-2-yl)-2,5-diphenyltetrazolium bromide (MTT) tests detect integrity of cell membrane and the activity of enzyme in mitochondria, reflecting the degree of damage on mitochondria function; glucose-6-phosphate dehydrogenase (G6PD) assay detects levels of G6PD leaking from damaged cell membranes; Ethidium homodimer-1 (EthD-1) stain detects cells membrane integrity, and Calcein acetoxymethyl ester (Calcein AM) stain detects intracellular esterase activities. Considering the different cytotoxicity

mechanisms of nanoparticles that affect cells, it is imperative that the combined use of these toxicity assays could provide comprehensive information on nanoparticle cytotoxicity.

This work focuses on *in vitro* cytotoxicities of bismuth nanoparticles by combining three different assays (MTT, G6PD and Calcein AM/EthD-1) as shown in Figure 4-1.

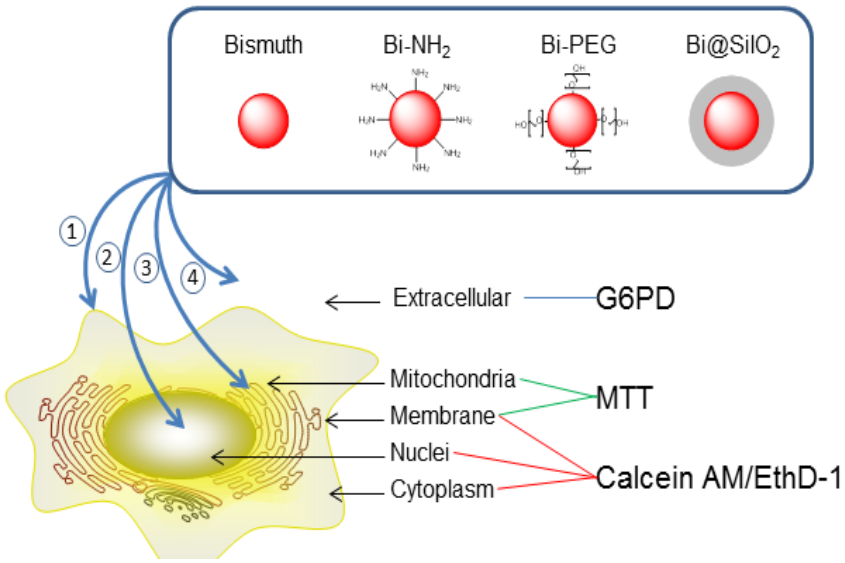

Figure 4-1 Cytotoxicity study of bismuth nanoparticles using multi-end point assays: where nanoparticles combine with membrane (1), enter nucleus (2), enter cell and affect mitochondrion (3), or stay outside of cells (4).

Various surface modifications and different concentration of nanoparticles are used to test the toxicity levels on two kinds of mammalian cells (HeLa cell and MG-63 cell) The results are cross-compared to those derived from CdSe/ZnS quantum dots and Fe_3O_4 nanoparticles. Our results show that bismuth nanoparticles are more toxic than previously reported bismuth compounds. HeLa cells are more vulnerable to cytotoxicity of various surface modified bismuth nanoparticles than MG-63 cells; and cytotoxicities of surface modified bismuth nanoparticles are

in descending order of amine modified nanoparticles (Bi-NH_2), bare bismuth nanoparticles (Bi), silica modified nanoparticles (Bi@SiO_2), and PEG modified nanoparticles (Bi-PEG).

4.2 Experimental Section

Vybrant MTT cell proliferation kit, vybrant cytotoxicity assay kit, and live/dead viability/cytotoxicity kit are purchased from Invitrogen (Carlsbad, CA). Polyethylene glycol-terminated silane (PEG-silane, 472−604 g/mol) is from Gelest (Tullytown, PA). Bi $(CH_3COO)_3$, $BiCl_3$, $NaBH_4$, RPMI 1640 media, penicillin, streptomycin, fetal bovine serum (FBS), and Dulbecco's phosphate-buffered saline (D-PBS) are from Sigma-Aldrich (St. Louis, MO). Anhydrous dimethyl sulfoxide (DMSO), toluene, polyvinylpyrrolidone (PVP), tetraethylorthosilicate (TEOS), 3-aminopropyltriethoxysilane (APTES), iron oleate, octadecence, diphenylether, sodium oleate, and mecaptoacetic acid (MAA) are from VWR (West Chester, PA). Ultrapure water (18.2 MΩcm-1) from Nanopure System (Barnstead, Kirkland, WA) is used. Synergy HT multi-mode microplate reader from Biotek (Winooski, VT) is used for absorbance and fluorescence measurements. HeLa (Cat # CRL-2) and MG-63 (Cat # CRL-1442) cell lines are from American Type Culture Collection (ATCC, Manassas, VA).

4.2.1 Synthesis of Nanoparticles

Bismuth and iron oxide nanoparticles are synthesized as described in section 3.2.1. Cadmium selenide nanoparticles are made as described in an earlier study.[90] Briefly, 1 mmol of

TOPSe and 1.35 mmol of dimethylcadmium are dissolved in 5 ml of trioctylphospine (TOP), and rapidly injected in a vigorously stirred mixture of 10 g of trioctylphosphine oxide (TOPO) and 5 g of hexadecylamine (HDA) heated to 300 °C. Injection results in an immediate nucleation of nanoparticles, which have a broad absorption maximum around 450 nm. Further growth occurs at 250-310 °C depending on the desired size. For the synthesis of CdSe/ZnS core-shell nanoparticles, 2.5 ml of crude solution of CdSe nanoparticles is mixed with 5 g of TOPO and 2.5 g of HDA, and heated to 220 °C. The amount of Zn:S stock solution necessary to obtain the desired shell thickness is calculated from the ratio between core and shell volume using bulk lattice parameters of CdSe and ZnS. This amount is then added drop wise to the vigorously stirred solution of CdSe nanoparticles.

A JEOL 1011 transmission electron microscope (TEM) operated at 100 kV is used to image nanoparticles. Bismuth nanoparticles are found to have an average diameter of 20 nm while the silica coated bismuth nanoparticles have an average thickness of 10 nm where the bismuth core is 20 nm. TEM images also show that Fe_3O_4 nanoparticles and CdSe/ZnS quantum dots have an average diameter of 20 and 10 nm, respectively.

4.2.2 Surface Modification of Nanoparticles

In order to conjugate with PEG, bismuth nanoparticles are modified by adding 20 µl PEG silane and 1 mg of bismuth nanoparticles into 180 µl of toluene. After reacting under sonication for 3 h at the room temperature, unreacted PEG saline is removed by centrifugation and washing three times with toluene. In order to make amine conjugated nanoparticles, bismuth or iron oxide

nanoparticles are mixed with 5% 3- APTES in toluene for 2 h, followed by removal of extra silane by centrifugation and washing with toluene. CdSe/ZnS quantum dots are modified with MAA by mixing 35 µl of MAA with 1 mg of CdSe/ZnS nanoparticles in 500 µl of chloroform under sonication for 2 h, followed by washing with toluene for three times. The unreacted MAA are removed by dialysis against double deionized water using 3.5 K molecular-weight cutoff (MWCO) membrane for 12 h. The stock solutions of bismuth nanoparticles (Bi), silica encapsulated bismuth nanoparticles (Bi@SiO_2), amine modified bismuth nanoparticles (Bi-NH_2), PEG modified bismuth nanoparticles (Bi-PEG), carboxylic acid modified CdSe/ZnS (CdSe/ZnS-COOH), carboxylic acid modified iron oxide (Fe_3O_4-COOH) and amine modified iron oxide (Fe_3O_4-NH_2) nanoparticles are homogeneously dispersed in sterilized phosphate buffer saline (PBS) at pH = 7.4 before they are ready to use.

4.2.3 Treatment of Cells with Nanoparticles

Human adenocarcinoma HeLa cells and human osteosarcoma MG-63 cells are cultured and treated with nanoparticles as described in section 3.2.3. After the cell monolayer becomes 80% confluence, HeLa cells and MG-63 cells are incubated with Bi, Bi-NH_2, Bi-PEG, Bi@SiO_2, amine modified Bi@SiO_2 (Bi@SiO_2-NH_2), CdSe/ZnS-COOH, Fe_3O_4-COOH and Fe_3O_4-NH_2 with final concentrations of 0.5, 5, and 50 nM, respectively. After 24 h, the media are removed and all wells are washed three times with PBS prior to performing any toxicity assay.

4.2.4 Cytotoxicity Assays

MTT assay is carried out as described in section 3.2.6. G6PD assay is carried out by following the standard protocol. A 50 µl of 2× resazurin/reaction mixture is added to each well, along with fully lysed cells control and live cell control. All samples are assayed in six duplicates. 1 µl of 100× cell lysis buffer is added to lysed-cell control wells to kill cells. The microplate is incubated at 37 °C for 30 min prior to measuring fluorescence intensity at 580 nm with 530 nm excitation. Calcein AM/EthD-1 assay is carried out as following: 100 µl of D-PBS is added into each well to wash cells in order to dilute serum-containing esterase, which can lead to false positive. A 100 µl of dual fluorescence Calcein AM/EthD-1 assay reagents is added into each well and incubated for 30 min at room temperature before fluorescence measurement. A cell-free control is used to measure background fluorescence and these signals were subtracted before later calculations. The percentages of live cells and dead cells are calculated by the equation provide by Invitrogen. A fluorescence microscope from Olympus (BX51M) is used to take fluorescent images.

4.2.5 Statistical Analysis

The data are presented as mean ± standard deviation (SD) of six independent experiments, and the error bars in each figure represent the standard error of these six independent experiments. Some data are subjected to statistical analysis by one-way analysis of variance (ANOVA) followed by Dunnett's method for multiple comparisons. A value of p

<0.05 is considered significant. SPSS 16.0 software is used for the statistical analysis and Origin 8.5 software was used for the graph plotting.

4.3 Results and Discussions

4.3.1 Calcein AM/EthD-1 Assay

Calcein AM/EthD-1 dual-fluorescent assay can stain the live cells green and the dead cells red simultaneously, providing more comprehensive information of cytotoxicity determination than traditional single-fluorescent assay. Figure 4-2A-D shows representative fluorescent micrographs of HeLa cells after incubating with 100 ml of 50 mM surface-modified bismuth nanoparticles for 24 h in Calcein AM/EthD-1. These figures show that most of the HeLa cells treated by Bi (Figure 4-2A) or Bi-NH_2 (Figure 4-2B) are stained as red (dead), while most of the HeLa cells treated by either Bi@SiO_2 (Figure 4-2C) or Bi-PEG (Figure 4-2D) are stained green (live).

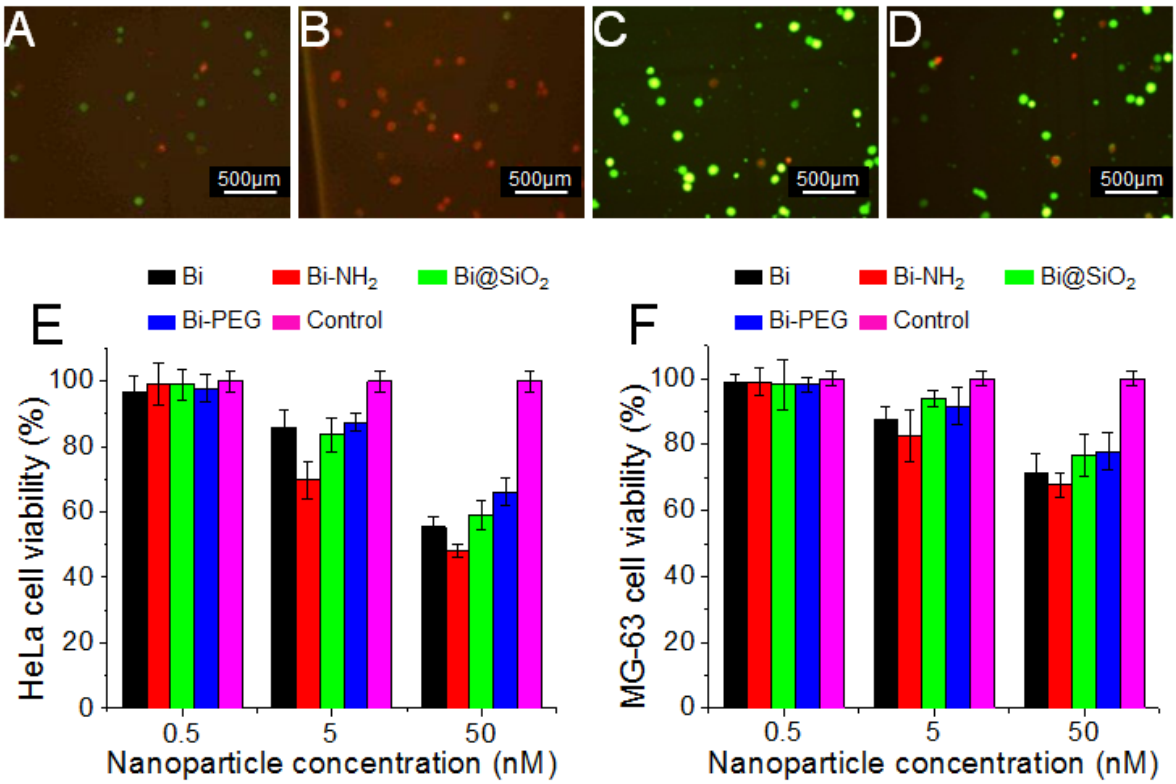

Figure 4-2 Calcein AM/EthD-1 dual-fluorescence stain of HeLa cells that are treated by bismuth nanoparticles (A), amine modified bismuth nanoparticles (B), silica coated bismuth nanoparticles (C), and PEG modified bismuth nanoparticles (D); HeLa cell viability after exposing to bismuth nanoparticles (E); MG-63 cell viability after exposing to bismuth nanoparticles (F).

Figure 4-2E and 4-2F show a nanoparticle concentration-dependent cell viability of both HeLa and MG-63 cells. When the cells are treated by low concentration nanoparticles (0.5 nM), no significant decrease in viability is observed when compared with untreated control (p <0.01). But after exposure to high concentration (50 nM) of nanoparticles, the viabilities of both cells decreased sharply. To eliminate the errors induced by the natural death of cells, a ratio between the nanoparticle-treated cell and untreated control is taken as the viabilities, assuming the viability of untreated control is 100%, despite the fact that normal cell metabolism processes still produce a small number of dead cells. Figure 4-2E shows that for HeLa cells, Bi kills 3.2%,

15%, and 45% of the cells at nanoparticle concentrations of 0.5, 5, 50 nM, respectively; Bi@SiO_2 kills 2.3%, 17%, and 41% of the cells at these concentrations; Bi-PEG kills 2.5%, 13%, and 34% of the cells; and Bi-NH_2 kills 2.2%, 31%, and 52% of the cells at these nanoparticle concentrations, respectively. These data clearly show that all the surface modified bismuth nanoparticles are of low cytotoxicity when the concentration is low (0.5 nM), and the cytotoxicities increase when the nanoparticle concentration increases. Meanwhile, a significant difference in the cytotoxicity is observed when the HeLa cells are exposed to 50 nM bismuth nanoparticles with different modifications. At high nanoparticle concentration (50 nM), Bi-NH_2 kills over 50% of the HeLa cells, while Bi-PEG kills only 34% HeLa cells, indicating the significant effects of surface modifications on the cytotoxicity of bismuth nanoparticles. According to the results above, the toxicities of these nanoparticles on HeLa cells are in the order of Bi-NH_2> Bi >Bi@SiO_2 >Bi-PEG.

Figure 4-2F shows that for MG-63 cells, low concentrations of bismuth nanoparticles kill ~1% MG-63 cells, showing extremely low cytotoxicities. High concentration (50 nM) of bismuth nanoparticles kill 29%, 33%, 24%, 22% of MG-63 cells for Bi, Bi-NH_2, Bi@SiO_2, and Bi-PEG, respectively. The level of cytotoxicity offered by these nanoparticles to MG-63 cells are of the same order as those offered to HeLa cells (Bi-NH_2> Bi > Bi@SiO_2 > Bi-PEG). However, less MG-63 cells are killed than HeLa cells when both cells are exposed to bismuth nanoparticles having the same concentration and the same surface properties. An observation of the higher viability of MG-63 cells than HeLa cells could be 16%, 19%, 15%, 18% more when they are exposed to 100 ml of 50 nM Bi, Bi-NH_2, Bi@SiO_2, and Bi-PEG, respectively, indicating that the

HeLa cell is more sensitive to the nanotoxicity for all the surface modified bismuth nanoparticles than MG-63 cells.

4.3.2 G6PD Assay

G6PD leaking assay is performed to test the membrane integrity by measuring the leaked G6PD levels. Figure 4-3A and 4-3B show the percentage of dead HeLa cells and MG-63 cells, respectively, for three different concentrations of nanoparticles.

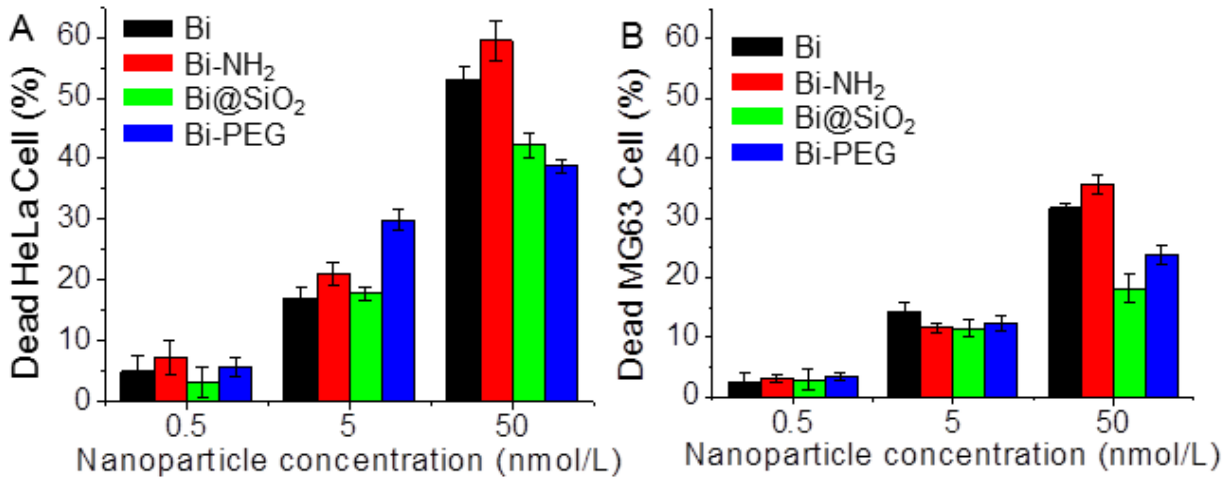

Figure 4-3 Percentage of dead cells from G6PD assay of bismuth nanoparticles treated HeLa cells (A) and MG-63 cells (B), where nanoparticle concentration is 0.5, 5, and 50 nM, and incubation time is 24 h.

For HeLa cells (Figure 4-3A), low concentration (0.5 nM) of all the surface modified bismuth nanoparticles show low toxicity by killing 5.4%, 7.2%, 3.5%, 6.1% of the cells for the Bi, Bi-NH_2, Bi@SiO_2, and Bi-PEG, respectively. High concentration (50 nM) of bismuth nanoparticles kill 53%, 59%, 42%, 39% of the cells for Bi, Bi-NH_2, Bi@SiO_2, and Bi-PEG, respectively. For MG-63 cells (Figure 4-3B), these nanoparticles kill 31%, 35%, 18%, 24% of

the cells at 50 nM nanoparticle concentration, which is lower than the number of HeLa cells killed by the same concentration of bismuth nanoparticles.

4.3.3 MTT Assay

MTT assay detects the cytotoxicity of nanoparticles by determining the plasma membrane integrity and mitochondrial function, which reflect the metabolism activity. Figure 4-4A shows that the viabilities of HeLa cells decrease when the bismuth nanoparticle concentrations increase and a dose (or nanoparticle concentration) dependence can be clearly seen.

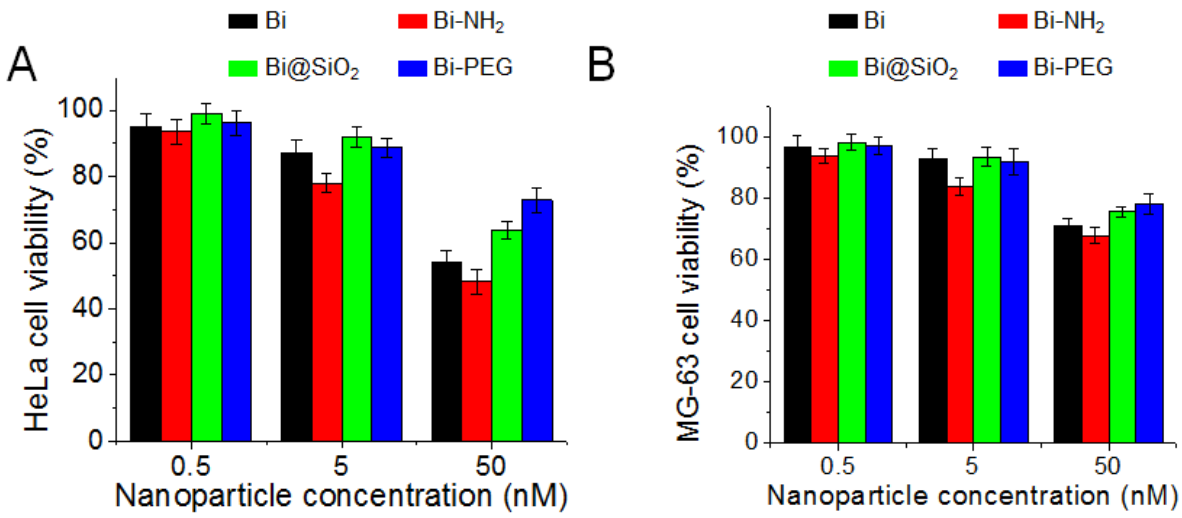

Figure 4-4 MTT assay on bismuth nanoparticles treated HeLa cells (A) and MG-63 cells (B), where nanoparticle concentration is 0.5, 5, and 50 nM, and incubation time is 24 h.

When treated with 50 nM nanoparticles, Bi-NH_2 shows the highest toxicity by killing 52% of the HeLa cells, while Bi@SiO_2 and Bi-PEG kill 37% and 28% of the cells accordingly.

This result shows that Bi-NH_2 has higher cytotoxicity than bismuth nanoparticles with other surface modifications, and corresponds to the results obtained from Calcein AM/EthD-1 analysis. Figure 4-4B shows that the viability of MG-63 cells treated with Bi–NH_2 is lower than those treated with bismuth nanoparticles with other surface properties. PEG-modified bismuth nanoparticles have shown lowest toxicity for both HeLa cells and MG-63 cells, because PEG has extremely low sticking energy to cells.

4.3.4 Comparison of Toxicity between Surface Modified Bi, CdSe/ZnS, and Fe_3O_4 Nanoparticles

The nanotoxicity of bismuth nanoparticles on HeLa cells and MG-63 cells are compared to those of CdSe/ZnS and Fe_3O_4 nanoparticles as shown in Figure 4-5:.

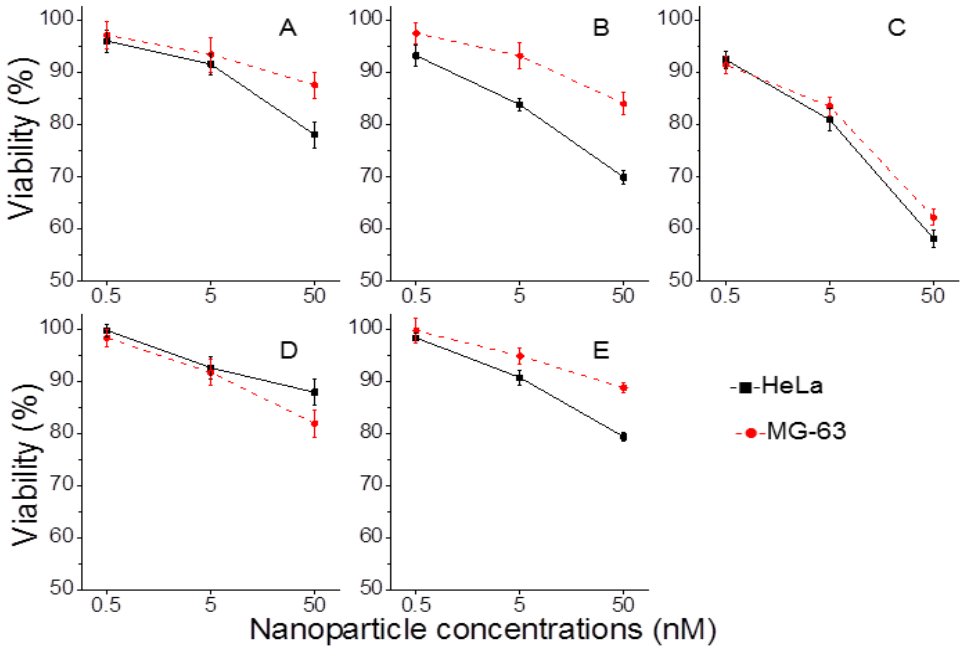

Figure 4-5 Cytotoxicity of $Bi@SiO_2$ (A), $Bi@SiO_2$-NH_2 (B), CdSe/ZnS-NH_2 nanoparticles (C), Fe_3O_4-COOH (D), and Fe_3O_4-NH_2 (E) on HeLa cell and MG-63 cell at nanoparticle concentration of 0.5, 5 and 50 nM, where Calcein AM/EthD-1 assay is used to test cytotoxicity.

$Bi@SiO_2$ is reacted with APTES to make $Bi@SiO_2$-NH_2. For 100 ml of 50 nM nanoparticles exposure, Calcein AM results show that $Bi@SiO_2$ (Figure 4-5A) and $Bi@SiO_2$-NH_2 (Figure 4-5B) kill ~22% and ~29% HeLa cells, respectively, while CdSe/ZnS-NH_2 (Figure 4-5C).demonstrate killing of 43% HeLa cells

Fe_3O_4-COOH (Figure 4-5D) or Fe_3O_4-NH_2 (Figure 4-5E) shows a relatively low cytotoxicity by killing ~7% and ~20% HeLa cells, respectively. For nanoparticles of different core, the cytotoxicities are in the order of CdSe/ZnS > $Bi@SiO_2$ > Fe_3O_4 and the toxicity of $Bi@SiO_2$ varied significantly according to the surface modifications. The high cytotoxicities of CdSe/ZnS-NH_2 have been reported by others, which are mainly attributed to the release of toxic Cd^{2+}. For different surface modification of the same nanoparticles, Fe_3O_4-NH_2 is more toxic than

Fe_3O_4-COOH to HeLa cells by killing 13% more HeLa cells. Similarly, Bi@SiO_2-NH_2 is more toxic than Bi@SiO_2. Thus, amine group modification can increase cytotoxicity of nanoparticles more than other surface modifications.

A dose-dependent cytotoxicity is also observed for MG-63 cell. As expected, the CdSe/ZnS nanoparticles give strongest cytotoxicity when compared with iron oxide and bismuth nanoparticles. 50 nM Fe_3O_4-COOH kills 6% more MG-63 cells than 50 nM Fe_3O_4-NH_2 does, indicating Fe_3O_4-NH_2 is less toxic than Fe_3O_4-COOH. This result is opposite to the toxicity derived from the HeLa cells, which could be explained by cell-type-dependent cytotoxicity of nanoparticles.[91] The adhesion of nanoparticles on cell surface is a prerequisite for nanoparticles entering cells via endocytosis. Different proteins or cytokines are excreted on surface of HeLa cells and MG-63 cells. Proteins on HeLa cells tend to adhere to carboxyl group, while those on MG-63 cells tend to adhere to amine group. This adherence of nanoparticles on cell surface mediates the penetration of nanoparticles, thus accelerating cell death by releasing ROS.

Our results show that CdSe/ZnS-NH_2 is the most toxic among three types of nanoparticles by killing ~21% more HeLa cells than Bi@SiO_2 and ~36% and ~ 23% more than Fe_3O_4-COOH and Fe_3O_4-NH_2 nanoparticles, respectively. This is in accordance with previous reports that CdSe/ZnS nanoparticle is more toxic than Fe_3O_4 nanoparticle at the same surface modification.[75, 86, 92-94] The higher toxicity of CdSe/ZnS is mainly due to releasing of Cd^{2+} ions and formation of ROS after being digested into the cytoplasm.[91] The lower toxicity of Fe_3O_4 is perhaps because the released iron ions (Fe^{3+}) are transferred and utilized by red blood cells. The toxicity of bismuth is relatively low, mainly because released bismuth ions (Bi^{3+}) are the least toxic among all heavy metals.

Silica encapsulated bismuth nanoparticles cannot be treated as silica nanoparticles, because culture medium diffuses into porous silica shell, and takes out bismuth ions. Bi@SiO_2 and Bi-PEG can significantly reduce inherent toxicity of the bare bismuth nanoparticles. Bi-PEG has the lowest toxicity due to low zeta potential and reduced interaction with receptors. Because most receptors, that mediate specific interactions between cells and their extracellular milieu, are located on plasma membrane,[95] the non-adhesive Bi-PEG cannot be internalized through mediation of receptors, and has low cytotoxicity.[96] The cytotoxicity of insulin-immobilized CdS nanoparticles was greatly suppressed by using PEG as spacer.[79]

The difference between G6PD leaking and MTT can be explained by the fact that cell metabolic activity is less affected even though plasma membrane is damaged. If this phenomenon exists in differently modified nanoparticles, it means that surface modified nanoparticles can damage the cells, yet cannot damage mitochondria of cells. Therefore, the mechanism of nanoparticle-cell interaction can be revealed at least partially by combining multiple *in vitro* assays that have different end-points. Bi-PEG treated cells have shown different viability in MTT assay and G6PD assay, suggesting that Bi-PEG affects less on cell mitochondria. Because Bi-PEG does not have strong affinity to proteins secreted on cell surface, most of Bi-PEG nanoparticles are expelled outside cell membrane. Bi@SiO_2 can enter cell membrane, and have effect on activity of intracellular esterase, while it has less effect on mitochondria, indicating that the toxicity of Bi@SiO_2 is less related to metabolic function. Bi-NH_2 shows similar viability in MTT and G6PD assay, suggesting that damage to mitochondria function is consistent with damage to plasma membrane, and cytotoxicity of Bi-NH_2 is mainly due to compromised metabolic function.

4.4 Conclusion

The cytotoxicity of bismuth nanoparticles is studied on HeLa cells and MG-63 cells by combining three assays (MTT, G6PD, and Calcein AM/EthD-1). HeLa cell is more susceptible to cytotoxicity of bismuth nanoparticles than MG-63 cell. For same surface modifications, bismuth nanoparticles are less toxic than CdSe/ZnS at the same nanoparticle concentration and has similar toxicity as iron oxide nanoparticles. Surface modifications have significant impact on cytotoxicity of bismuth nanoparticles. The cell viability (from MTT, G6PD, and Calcein AM/EthD-1) is in sequence of Bi-NH_2, Bi, Bi@SiO_2, and Bi-PEG (from lowest to highest). The combined use of complementary toxicity assays can therefore provide more information on cytotoxicity of nanoparticles. The results are useful in applying appropriate surface modification procedures to reduce inherent toxicity of bismuth nanoparticles for potential clinical applications in humans.

CHAPTER 5: ON-CHIP IMAGE BASED RADIATION BIODOSIMETER FOR IN-SITU RADIATION MONITORING USING THREE DIMENSIONAL MICROTISSUE

5.1 Introduction

Fast and accurate determination of radiation-induced damage to living cells, in a field setting, is highly desirable. Although a variety of radiation dosimeters including ion chamber, quartz fiber dosimeter, film dosimeter and polymer gel dosimeters can be used to detect the type and dose of radiation over a certain period of time, they cannot provide information on individual biological response to radiation. Biological dosimeter (i.e., biodosimeter) uses biomaterials such as cells to monitor radiation doses received by an individual, and can provide important information on bio-response of radiation exposure, which is highly complementary to physical dosimeters. Rapid biodosimetry in field settings can help to distinguish those who need urgent medical treatments after radiation injuries.[97] Moreover, monitoring responses of mammalian cells to radiation is highly crucial in cancer radiation therapy to avoid inducing secondary cancers from over-exposure to X-rays.

The gold standard of biodosimetry is dicentric assay that is often performed in peripheral blood lymphocytes to examine characteristic chromosome damage, but dicentric assay takes a long time for microscopic scoring of a sufficient number of damaged cells, especially in the case of low radiation dose where damaged cells are hard to find.[98] Other techniques, including micronucleus, translocation, premature chromosome condensation assay, and molecular biomarker methods (gamma-H2AX assay) have been proposed recently to detect radiation

damages,[99-102] but most of them require highly-trained personnel and well-equipped facilities (i.e., microscope), and are invasive in nature. In addition, different cells resist differently to the same radiation dose due to different radiation susceptibility. Therefore, it is imperative to derive radiation effects from multiple types of mammalian cells.[103] But, existing biodosimetry techniques have low throughput, are complicated, expensive, laborious and time-consuming when handling multiple cell types, and need to be carried out in centralized laboratory settings, which limit their uses in field-deployable detections in places such as nuclear power plants, medical or military facilities where continuous dose monitoring is necessary to ensure personal safety.

In vitro grown mammalian cells could be used to construct low-cost, facile, non-invasive, sensitive, potentially high-throughput and field-deployable biodosimeters. However, cells from two-dimensional (2D) monolayer cultures are too sensitive to environmental changes even in the absence of radiation, which make them unsuitable as responsive components in biodosimeters. Instead, cells in three-dimensional (3D) aggregates are in an environment close to physiological condition and can closely mimic the tissue architectures and functions in humans; meanwhile, these aggregated cells have shown higher stability than those from 2D culture.[104] At last, although many traditional techniques including spinning, hanging drop, micro-spheroid chips, and liquid-overlay methods have been used to make 3D microtissues, these techniques are laborious, and have low throughput, and low uniformity in terms of density, shape and size.[105-107] Photolithography based microfabrication techniques can generate size- and geometry-controlled microstructures, which can be used to make 3D microtissues with uniform size at high yield and low cost.[108]

This work describes a new microtissue based on-chip biodosimeter that can accurately monitor the response of individuals to ionizing radiation in field settings by capturing instant images using camera phones and then wirelessly transmitting those images to a remote location for analysis. The biodosimeter is based on two techniques: *in vitro* 3D microtissue and high-resolution digital camera of mobile phone to monitor cell death in real time for rapid determination of radiation exposure.[109-111] An array of microtissues is exposed to X-ray radiation that causes cell death; after staining, dead cells can be identified from the color that is visible to the naked eyes. Images of the microtissues are taken by camera of a mobile phone, and transmitted wirelessly to a computer, where the color intensity of each microtissue is analyzed to determine the amount of dead cells. The use of an array of micro-tissues greatly eliminates errors during measurements, and allows multiple cell types to be used for studying biological response to radiation. This method has high sensitivity, enabling low dose of ionizing radiation to be detected over a large area.

5.2 Experimental Section

5.2.1 Fabrication of On-chip Biodosimeter

The micropost mold is fabricated using reported photolithography technique.[112] The depth and width of microposts are 1,000 and 800 μm, respectively. In order to generate 3D microtissue array, microwells are cast from the mold as shown in Figure 5-1

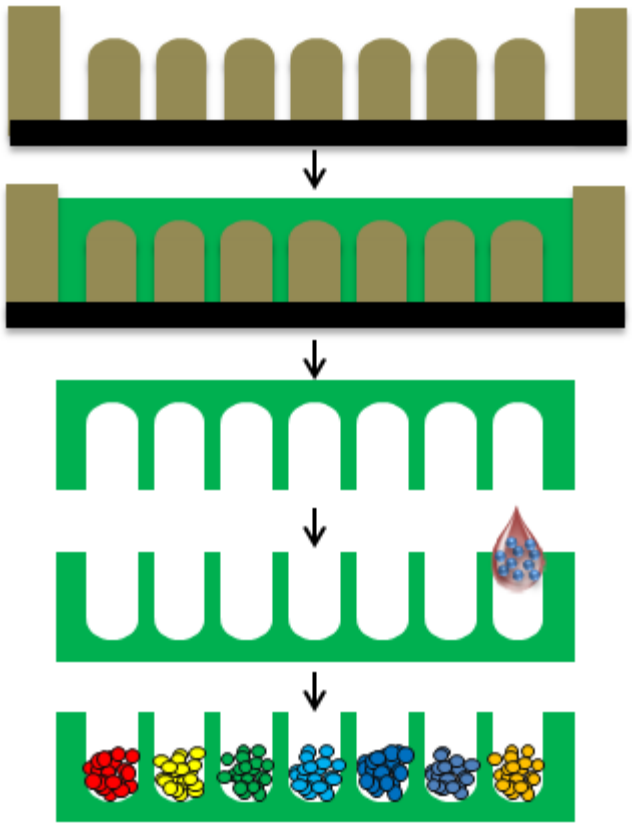

Figure 5-1 Fabrication of three dimensional microtissues in agarose gel.

A 2% low melting agarose (85 °C) is melt and poured on a tray and the micromold is placed on top until agarose is set. The mold is carefully removed leaving microwells in agarose film. HeLa cells (American Type Cell Culture, Manassas, VA) are cultured in 2D cell culture plate filled with RPMI 1640 media for 1-2 days until 80% confluence is achieved. The cells are detached from substrate using 0.25% trypsin-EDTA and are counted using a hemocytometer after centrifugation at 1000 rpm for 5 min. In the next, 2×10^5 cells in media are seeded in a 9×9 array of microwells, where approximately 2.4×10^3 cells can occupy one well. The use of agarose as a substrate minimizes cell-substrate interaction, and the cell-to-cell adhesion drives spontaneous self- assembly of cells into 3D microtissues within an hour.

5.2.2 X-ray Exposure

A Mini-X X-ray tube (Amptek, Inc., Bedford, MA) operating at tube voltage of 40 kV and current of 100 μA is used to generate primary X-rays. The surface dose rate, at a distance of 5 cm from the tube, is measured using a handheld radiation dosimeter (Mirion RAD-60, Freshwater Systems, Greenville, SC) and is found to be 0.4 Gy/h. The 9×9 array (surface area of ~1 cm^2) of microwells loaded with HeLa cells is then fixed at a distance of 5 cm from X-ray source, which is fitted with a collimator resulting in an output cone angle of 10º for the emerging beam. The X-ray beam covers an area of ~2.4 cm^2 on the exposed surface that is sufficient to uniformly irradiate the entire array. After X-ray irradiation for different times ranging from 1 min to 1 h, trypan blue, a non-fluorescent dye that stains dead cells blue while leaving live cells unaltered, is added into microwells to stain cells in the microtissue. High throughput radiation detection and monitoring is achieved by introducing three cell lines (HeLa, MG-63, and LNCaP) into a single biodosimeter. By controllably pipetting 1 μl of cell suspension into each microwell using a small volume tip, an array of different microtissues is made on the same biodosimeter for high throughput applications.

5.2.3 Cell Viability

Cell viability is monitored in real time for dosimeters containing HeLa, MG-63 and LNCaP cells, respectively. This is done by measuring the color intensity of each microwell from images taken every 30 min following a 1 h X-ray exposure (0.4 Gy). The images are analyzed with Image Pro Plus 6.0 (Media Cybernetics, Bethesda, MD) software, which can correct

background and obtain color intensity of an area of interest. In addition, MTT assay is performed on the three cell lines at 30 min intervals after exposure to 0.4 Gy X-rays. MTT assay can detect live or dead cells by measuring the integrity of cell membrane.

5.3 Results and Discussions

Figure 5-2A-D shows the optical micrographs of 3D microtissues at various stages of formation taken at different time (1, 10, 30 and 60 min) after seeding HeLa cells into microwells.

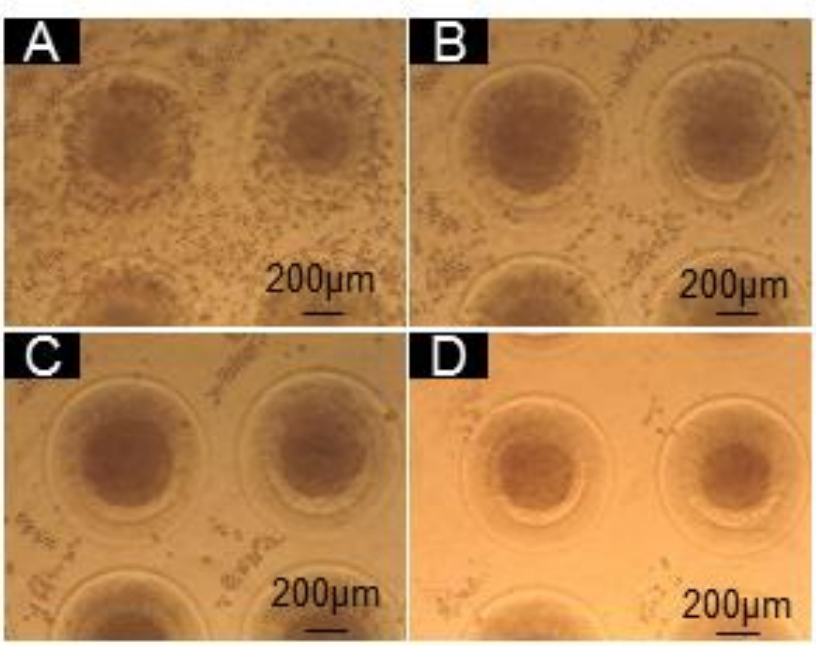

Figure 5-2 Various stages of a microtissue formation taken at 1, 10, 30 and 60 min after seeding HeLa cells into microwells (A-D).

Most cells float in suspension just after seeding (1 min); about 50% and 80% of cells settle gravitationally in microwells after 10 and 30 min, respectively; almost all cells aggregate

after 1 h of incubation. The initial cell aggregate becomes denser in 1-2 days, and the microtissue is stained using ethidium bromide (EB). Figure 5-3A shows a fluorescence image of a single microtissue containing HeLa cells The optical micrograph is taken by using Olympus BX-51M microscope under ultraviolet (465 nm) excitation, where the spherical shape of microtissue can be seen clearly. In order to determine cell viability in the cultured microtissue, dual fluorescence staining is carried out with Calcein AM/EthD-1, where EthD-1 stains dead cells red by penetrating into membrane-damaged cells and combining with DNA in nuclei, and keeps live cells unstained; while Calcein AM stains live cells green leaving dead cells unaltered. Figure 5-3B shows a fluorescence image of a microtissue where live HeLa cells (not exposed to X-rays) appear green in color. The absence of red color indicates that all cells are alive in microtissue.

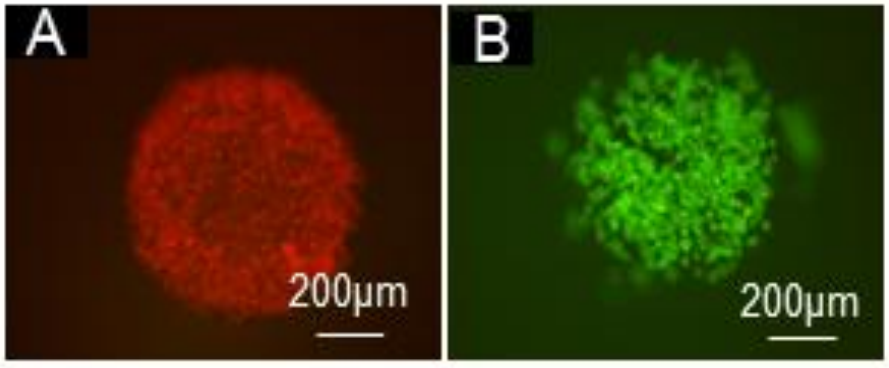

Figure 5-3 Fluorescent image of HeLa microtissue stained with EB (A) and CAM/EthD-1 (B).

Due to limited nutrition and oxygen available to cells inside microtissue, the growing speed of microtissue is slower than that of monolayer (doubling time of 24 h).[113] But, cells in microtissue can stay alive in fresh culture medium for over 96 h outside incubator, making microtissue very attractive for field-deployable radiation detection. One feasible way of having

even longer lifetime is to culture cells in the normal monolayer format, and form microtissue just few hours before they are used in biodosimeters.

Figure 5-4A shows a photograph of microwells taken with the camera (5 MP resolutions) of an iPhone 4, where HeLa cells are stained with trypan blue after formation of microtissue. The absence of blue color shows that most of cells in microtissue are alive. Figure 5-4B shows the image of 1 h X-ray irradiated microtissues that have been seeded with the same number of HeLa cells followed by trypan blue staining. The blue color of microtissue in each microwell is clear to the naked eye, and the color intensity of image is proportional to the number of dead cells.

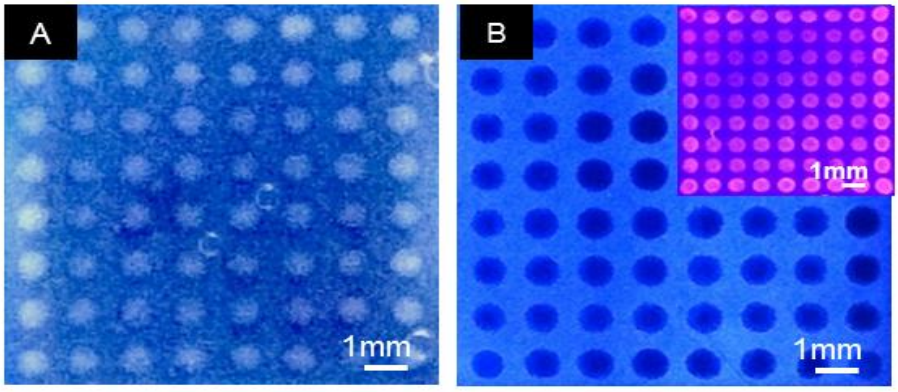

Figure 5-4 Optical images of HeLa microtissues in microwells stained with trypan blue, not exposed to X-ray (A), exposed to X-rays for 1 h (B) where the inset picture shows microwells stained with EthD-1 after X-ray exposure.

The inset picture in Figure 5-4B shows the fluorescence image of microtissues after EthD-1 staining taken with phone camera under an UV light, where dead cells appear red.

Figure 5-5A shows that the intensity of blue color increases and saturates to a value of ~100 after 9 h following a 1 h X-ray irradiation of the HeLa cells; under the same conditions, it takes 11 h and 14 h for MG-63 and LNCaP cells, to reach the same color intensity, respectively.

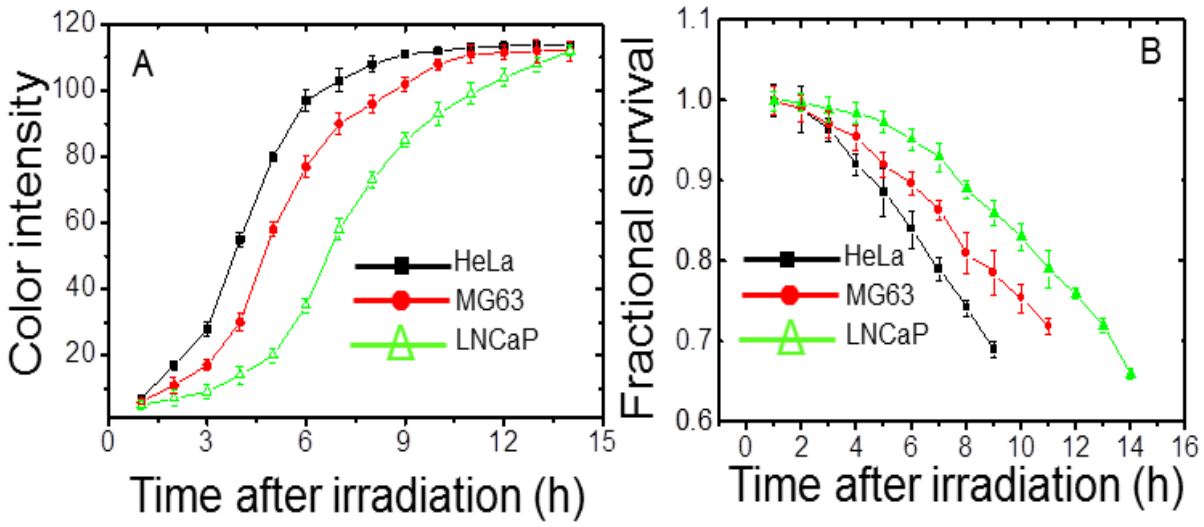

Figure 5-5 The intensity of blue color from trypan blue measured at different times after 1 h X-ray irradiation of microtissues containing different cell lines (A); corresponding survival fraction of the cell lines obtained from MTT assay (B). Error bar represents the standard error of 5 independent experiments.

To correlate the color intensity of trypan blue with cell viability, MTT assay is performed on the three cell lines Following a 1 h X-ray irradiation, ~30% HeLa cells are dead after 9 h (Figure 5-5B). However, ~28% MG-63 and ~33% LNCaP cells die after 11 h and 14 h, respectively. Results confirm that different cell lines respond differently towards the same X-ray dose with HeLa and LNCaP cells being the most and the least sensitive to X-rays, respectively. This can be explained in terms of the difference in cell cycle: HeLa cells double every 24 h; whereas MG-63 and LNCAP cells double every 26 h and 60 h. After X-ray induced DNA damage, cells will not die until they are in mitotic period where damaged DNA fails to

duplicate.[114] Thus, quantifying blue color of trypan blue stained microtissues over time allows in-situ real time monitoring of radiation responses.

Figure 5-6A is an optical micrograph of an array of microtissues, where three microwells in top row contains HeLa, MG-63 and LNCaP cells (left to right), and three empty wells in bottom row are controls. The compact arrangement allows all cells to be irradiated simultaneously with an uniform X-ray dose. After irradiating for varying times, cells in microwells are stained with trypan blue followed by imaging with phone camera.

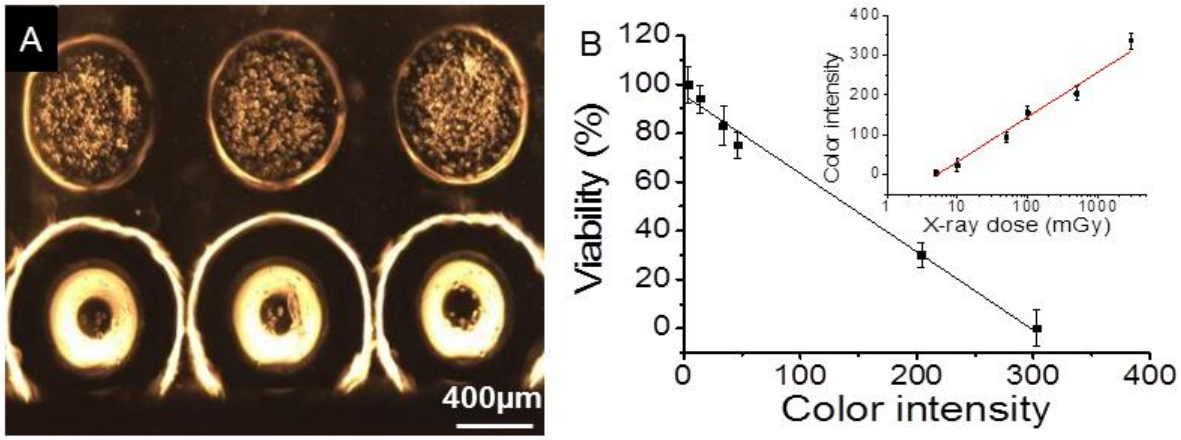

Figure 5-6 An optical microscope image showing controlled cell seeding in microwells (A), where the top row contains HeLa, MG-63 and LNCaP cells (from left to right), and the bottom row has no cells; HeLa cell viability against the color intensity of trypan blue stain, inset shows the variation of color intensity for trypan blue stain with X-ray dose (B).

Figure 5-6B shows that the increase in intensity of the blue color is proportional to the decrease in viability of HeLa microtissue. Similar results are obtained for MG-63 and LNCaP microtissues. The linear relation between color intensity and X-ray dose is also plotted accordingly. The current detection limit of our biodosimeter for HeLa microtissue is estimated to be ~5.0 mGy from the calibration curve. For microtissues of MG-63 and LNCaP cell lines, the

detection limits are estimated to be ~8.0 and 9.5 mGy, respectively. The limit of detection depends on the type of cell, because some cells are more sensitive to radiation than others.

Figure 5-7 shows cell death at different X-ray irradiation doses for three different types of microtissues where the percentage of dead cells directly correlates with the intensity of blue color from trypan blue stain after X-ray exposure. At higher doses more cells die, resulting in more intense blue color. Also, any given dose of X-rays kills more HeLa cells than MG-63 or LNCap cells, under the same conditions.

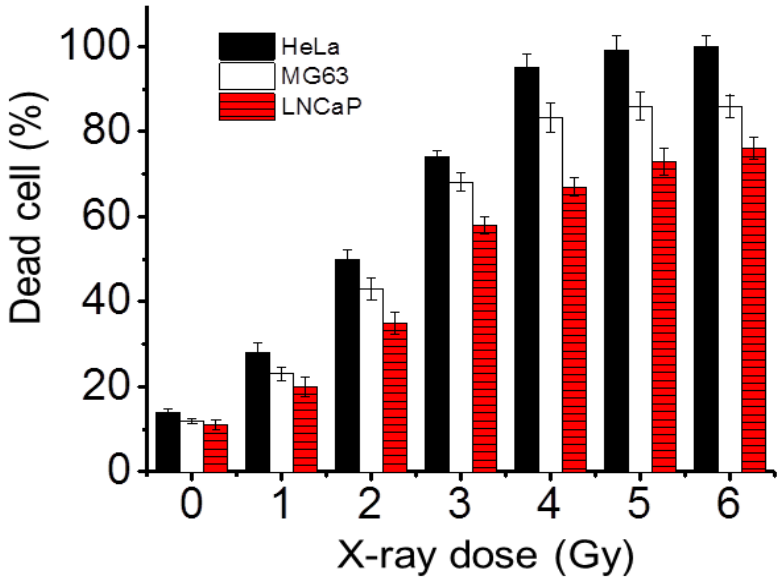

Figure 5-7 Percentage of dead cells for three different cell types after exposure to different X-ray doses.

In contrast to conventional radiation dosimeters, microtissue based biodosimeters can directly monitor the effect of both cumulative and continuous radiation exposures on mammalian microtissues. In case of cumulative exposure, the total dose is fractionated to 1 h/day (0.4 Gy/day) for 8 days, whereas for continuous exposure the whole dose (3.2 Gy) is applied

continuously for 8 h in one fraction. Figure 5-8 shows the continuous irradiations kill more cells in the HeLa microtissue than the cumulative irradiations, especially when the irradiation time is higher than 3 h. The difference in cumulative and continuous exposures is mainly caused by self-repairing of small amounts of DNA damage.[115] Cumulative exposure provides time for the damaged DNA to self-repair between exposures while in case of continuous exposure the damage accumulates faster than it can be repaired.

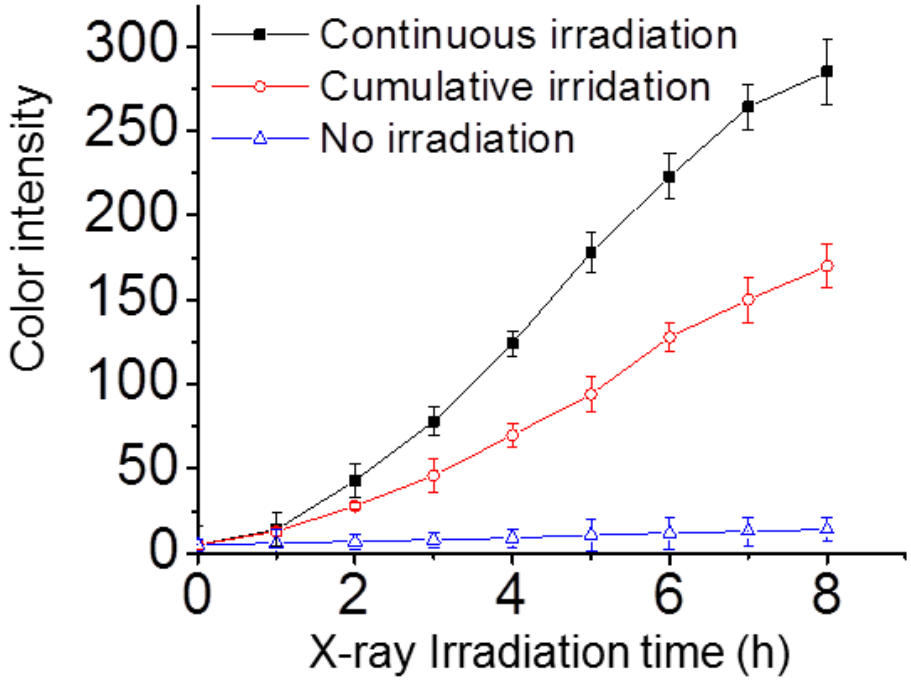

Figure 5-8 Color intensity of trypan blue stained HeLa microtissue for continuous and cumulative X-ray exposures. Error bar is the standard error of 5 independent experiments.

5.4 Conclusion

An image-based on-chip radiation biodosimeter using 3D microtissues has been built and used to detect cellular response of continuous and cumulative ionizing radiations. The 3D microtissues of multiple cell types, with defined structures and dimensions, can be fabricated at high yield and low cost, and can be conveniently imaged with the camera of a mobile phone. The color changes of microtissues upon exposure to ionizing radiations are detected and quantified, which allow facile and rapid transmission of radiation information to determine radiation responses of individuals in field settings. The biodosimeter will be highly useful for monitoring how human cells respond to X-ray exposure and will help in improving existing X-ray radiation therapy for cancer treatment.

CHAPTER 6: ANALYTICAL STUDY OF NANOPARTICLE ENHANCED X-RAY RADIATION THERAPY

6.1. Introduction

Radiotherapy aims to maximize radiation dose delivered to tumors with minimum damage to surrounding healthy tissues. The promising ability of gold nanoparticles as effective radiosensitizers for localized tumor dose enhancements have been extensively explored due to high X-ray absorption cross-section of gold compared to biological tissues.[116-123] Previous experiments with mice have shown significant increase in dose to tissue volumes in presence of gold nanoparticles.[124] Monte Carlo simulations have been performed extensively to investigate various parameters such as photon energy, particle size, concentration and location that govern radiosensitizing properties of gold nanoparticles.[125-129] A recent study also shows how geometry of nanoparticles affect X-ray dose enhancements.[130] Other theoretical studies reveal that targeted gold nanoparticles can enhance dose to endothelial cells surrounding a tumor by over 200 times depending on their concentration and energy of the irradiating X-ray photons.[131] Dose enhancement is often attributed to photoelectrons and Auger electrons generated from X-ray irradiated nanoparticles. Photoelectrons are highly energetic, have a long range (up to hundreds of microns) in surrounding water, and deposit a small fraction of their energy near the nanoparticle. On the other hand, Auger electrons have lower energy and shorter range (typically less than 1 μm), allowing most of their energy to be deposited close to the nanoparticle. Energy deposition by electrons will hydrolyze water molecules surrounding cells and their nuclei, producing free radicals that will induce DNA damage, eventually leading to cell death. Cell

nucleus that contains DNA is thus considered to be the most sensitive to radiation exposure.[132-134] Due to major contributions from short range Auger electrons, dose enhancement to nuclei is significantly different than that to entire cell. A recent theoretical study indicates that nucleus dose enhancement factor (nDEF) or the ratio of dose delivered to nucleus with and without gold nanoparticles can be as high as 73 for endothelial cell nuclei.[135] Experiments have also shown that gold nanoparticles can be internalized inside cancer cells, which makes nanoparticle location control a feasible choice for dose enhancement and subsequent radiotherapy.[136] In addition, although gold nanoparticles have been the prime choice for radiosensitizers due to their high biocompatibility, ease of conjugation to tumor targeting agents, and high X-ray absorption coefficients, nanoparticles of other heavy metals such as bismuth and platinum can also serve as promising alternatives to gold in radiotherapy.[137-142] However, there is no systemic investigation over potential benefits by controlling location and materials of nanoparticles relative to cancer cells in X-ray radiation therapy.

An analytical approach developed by Ngwa et al.[131] is used to derive radiosensitizing abilities of bismuth, gold and platinum nanoparticles at diagnostic X-ray conditions (50, 110 or 300 kVp). For each type of nanoparticles, doses delivered to endothelial cells and their nuclei are derived for particle sizes ranging between 2 to 400 nm in diameter, and concentrations ranging between 7 to 350 mg of nanoparticle per gram of tumor tissue. The contributions from both photoelectrons and Auger electrons are derived. Unlike previous studies, this work primarily focuses on dependence of dose enhancements on material composition and size, as well as location of nanoparticles using diagnostic X-ray sources (instead of using brachytherapy sources). In addition, the variation of nDEFs with respect to nanoparticle location has been

emphasized and discussed in context of photoelectron and Auger electron generation. Although Auger electron cross sections are derived from a previous Monte Carlo simulation due to lack of such data, the theoretical results from this investigation can provide useful insights in choice of nanoparticles in terms of nanoparticle nature, size and targeting location to achieve maximum efficacy in nanoparticle enhanced X-ray radiation therapy of cancer.

6.2. Methods

A slab of tumor endothelial cells with dimensions of 2 μm (thickness) × 10 μm (length) × 10 μm (width) has been considered in the following simulations (Figure 6-1).[131]

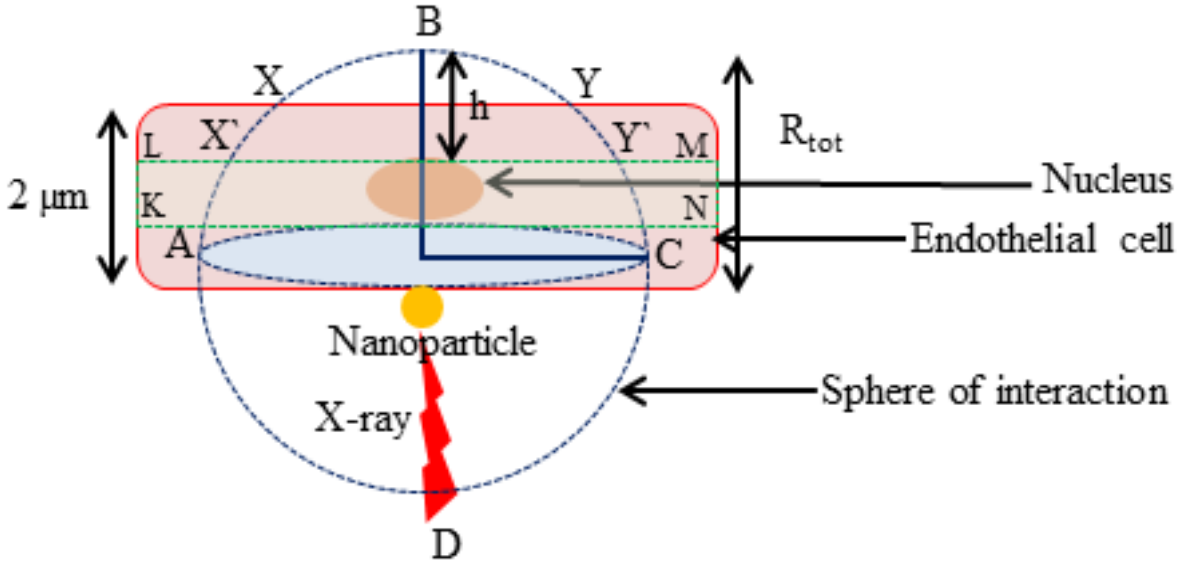

Figure 6-1 Slab model of endothelial cell lining a tumor.

The radius of sphere with nanoparticle in center is equal to the range of emitted photoelectrons generated by X-ray irradiation. Calculations are performed for spherical

nanoparticles attached to the outer surface of a tumor endothelial cell. Nanoparticles of a wide range of diameters are used to establish a relation between nanoparticle size and dose enhancements. Concentration of nanoparticles is expressed in terms of mass of nanoparticles per unit mass of tumor tissue, and corresponds to values found in previous theoretical and experimental studies. An arbitrary dose D_w (2 Gy) is taken as dose absorbed by cell without nanoparticle, which is also the dose absorbed by water inside the cell. The photon flux or the number of photons per unit area of nanoparticle that corresponds to D_w is calculated using:

$$D_w = \sum_E \Phi E_p \left(\frac{\mu_{en}}{\rho}\right)_E \quad \text{……………………………………………………………}(1)$$

where Φ is photon flux (photon/cm^2), E_p is the energy of a single photon (J), and $\left(\frac{\mu_{en}}{\rho}\right)_E$ is mass absorption coefficient of water (cm^2/g) at a given energy E. The number of photons (N_{ph}) incident on nanoparticle is derived by multiplying photon flux with cross-sectional area of nanoparticle; $N_{ph} = \Phi \times \pi r^2$, where r is radius of nanoparticle. The probability P of photoelectric interaction of incident photons with nanoparticle is given by $P \sim \left(\frac{\mu_{PE}}{\rho}\right)_E \rho_{NP} d_{NP}$ where $\left(\frac{\mu_{PE}}{\rho}\right)_E$ is the photoelectric absorption coefficient of nanoparticle at an energy E, ρ_{NP} is density of nanoparticle, and $d_{NP} = \frac{4r}{3}$ is the mean distance that the photons will travel through a spherical nanoparticle when incident upon it. X-ray photons generated from a 50 kVp source have a mean energy E ~29 keV. At E = 29 keV, $\left(\frac{\mu_{PE}}{\rho}\right)_{29keV} = 32.74$ cm^2/g for bismuth resulting in $P \sim 8.54 \times 10^{-3}$ for $\rho_{Bi} = 9.78$ g/cm^3 and r = 200 nm. Since the number of photoelectric interactions is equal to the number of emitted photoelectrons, the number of emitted photoelectrons per nanoparticle is derived from $N_{PE} = N_{ph} \times P$.

The next step is to determine the number of nanoparticles that attach on cell surface at given nanoparticle concentrations. The total mass of nanoparticles m_{total} in the entire volume of cell for a given concentration C (mg/g), is given by $m_{total} = C \times V_{EC} \times \rho_{EC}$, where V_{EC} (2×10^{-10} cm^3) and ρ_{EC} (1 g/cm^3) are the volume and density of cell, respectively. The mass of nanoparticle is obtained as $m_{NP} = \frac{4}{3}\pi r^3 \rho_{NP}$. Therefore, for any concentration C of nanoparticles, the number of nanoparticles that attach to cell is:

$$N_{NP} = \frac{m_{toal}}{m_{NP}} = \frac{CV_{EC}\rho_{EC}}{\frac{4}{3}\pi r^3 \rho_{NP}} \quad \text{.....(2)}$$

The total number of emitted photoelectrons can now be calculated as $N_{PEtotal} = N_{PE} \times N_{NP}$.

To evaluate the range of emitted photoelectrons, the kinetic energy E_{KE} of emitted photoelectrons must be known, which is given by $E_{KE} = E\text{-}E_{edge}$, where E_{edge} is relevant photoelectric absorption edge of nanoparticle. The average L-edge of bismuth is 15 keV giving E_{KE} = 14 keV. As emitted photoelectrons interact with their surroundings, they will deposit kinetic energy in a sphere of interaction centered on the nanoparticle. The radius of interaction sphere defines the range R_{tot} of photoelectrons and is given by:

$$R_{tot} = 0.0431(E_{KE} + 0.367)^{1.77} - 0.007 \quad \text{.....(3)}$$

At E_{KE} =14 keV, R_{tot} is 4.81 μm. For electron with kinetic energy between 20 eV to 20 MeV, Cole has derived an empirical relation[143] between electron energy loss $\frac{dE_{KE}}{dx}$ (keV/μm) and range R_{tot} (μm):

$$\frac{dE_{KE}}{dx} = 3.316(R_{tot} - x + 0.007)^{-0.435} + 0.0055(R_{tot} - x)^{0.33} \quad \text{.....(4)}$$

where x is the distance between the point where the photoelectron is generated and the point where it has traveled to. The total energy deposited by single photoelectron in cell volume is

obtained by integrating differential energy loss from surface of nanoparticle (r) to maximum range (R_{tot}) of photoelectrons (Figure 6-1):

$$E_{EC} = \int_{r}^{R_{tot}} \frac{H_{ABC} - C_{XBY}}{S_{ABCD}} \times \frac{dE_{KE}}{dx} \text{ dx} \quad \text{.....(5)}$$

where:

$$H_{ABC} = Area\ of\ hemisphere\ ABC = 2\pi {R_{tot}}^2$$

$$C_{XBY} = Area\ of\ hemispherical\ cap\ XBY = 2\pi(R_{tot} - t)$$

$$S_{ABCD} = Surface\ area\ of\ entire\ sphere\ ABCD = 4\pi {R_{tot}}^2$$

t = cell thickness.

Assuming a homogenous distribution of nanoparticles, and the dose delivered to the total volume of the sphere around the nanoparticle, the total energy deposited to cell by photoelectrons can be derived by multiplying E_{EC} with the total number of emitted photoelectrons, i.e., $E_{ECtotal} = E_{EC} \times N_{PEtotal}$. This calculation does not take into account the hemispherical shell in the blood vessel and the spherical shell beyond the cell. Dose contributions from nanoparticles on the opposite side of blood vessel are relatively small and therefore have not been considered. The dose delivered to the entire cell by photoelectrons, following nanoparticle and X-ray interactions, is obtained by dividing energy deposited in cell by the mass (volume×density) of cell: $D_{NP}(PE) = \frac{E_{ECtotal}}{V_{EC} \times \rho_{EC}}$. DEF due to photoelectrons is given by:

$$\text{DEF (Photoelectrons)} = \frac{Absorbed\ dose\ with\ nanoparticle}{Absorbed\ dose\ without\ nanoparticle} = \frac{D_W + D_{NP}(PE)}{D_W} \quad \text{.....(6)}$$

A DEF of 1.0 refers to 0% enhancement; while a DEF of 2.0 refers to 100% enhancement. At the nanoparticle concentration of 7 mg/g, DEF is 1.307, meaning that adding 7 mg of bismuth nanoparticles per gram of a tumor tissue increases X-ray dose by 65% when only the

photoelectrons are considered for energy deposition. The calculations are repeated for a series of nanoparticle concentrations ranging from 7-350 mg/g, and radius ranging from 1-200 nm. DEFs due to photoelectrons are calculated for gold and platinum nanoparticles using the same approach.

In order to derive contributions from Auger electrons, Auger electron spectra obtained from Monte Carlo simulations for tumors loaded with gold nanoparticles at 7 mg/g and irradiated with a 50 kVp X-ray source is used.[127] The energy deposited by Auger electrons in the cell is determined as described for photoelectrons. Average number of Auger electrons generated per absorbed X-ray photon (at 7 mg/g nanoparticle concentration) is 0.56 as derived from the Auger spectra.[127] Number of source photons and number of Auger electrons obtained for each source photon are multiplied to obtain the total number of emitted Auger electrons. Assuming a linear relation between the number of Auger electrons per source photon and nanoparticle concentration, the number of Auger electrons per source photon for any concentration can be derived simply by using the value at 7 mg/g as described by Ngwa et al.[131] For simplicity, the average number of Auger electrons per source photon generated from bismuth nanoparticles and platinum nanoparticles are also taken as 0.56 when irradiated by the same 50 kVp source. This is reasonable approximation assuming that the difference in Auger electron spectra of platinum (Z = 78), gold (Z = 79) and bismuth (Z = 83) is negligible due to their similar atomic numbers and therefore similar Auger yields when exposed to the same X-ray beam.

Both photoelectrons and Auger electrons can cause radiolysis of surrounding water, leading to formation of free radicals (mostly hydroxyl radicals). But free radical chain reaction can be terminated by scavengers such as lipids in cell membranes, or enzymes inside cell. It has

been found that mean diffusion length of free radicals is in the range of 200 nm in presence of 10^{-5} M scavengers in aqueous solution. Thus, to ensure maximum DNA damage caused by photoelectrons and Auger electrons, it is necessary to position nanoparticle as close to nucleus as possible. The slab model, used to calculate dose enhancement in cell, is slightly adjusted to include a nucleus that occupies 10% of cell volume (Figure 6-1).[135] The nucleus has a diameter of 0.5 μm and a thickness of 1.0 μm, and is located at the center of 2 μm thick slab. The boundary conditions in equation (5) are adjusted to include only the dose deposited by electrons within 1 μm thick slab (KLMN) section containing the nucleus. Energy deposited within 1 μm thick slab section containing nucleus is calculated as:

$$E_{slab} = \int_r^{R_{tot}} \frac{H_{ABC} - C_{X'BY'}}{S_{ABCD}} \times \frac{dE_{KE}}{dx} dx - \int_r^{R_{tot}} \frac{H_{ABC} - C_{ABC}}{S_{ABCD}} \times \frac{dE_{KE}}{dx} dx \quad \text{.....(7)}$$

For a centrally located nucleus inside a 2 μm slab $C_{X'BY'} = Area\ of\ spherical\ cap\ X`BY` = 2\pi R_{tot}(R_{tot} - t + 0.5\ \mu m)$, C_{ABC} = *Area of spherical cap ABC* = $2\pi R_{tot}(R_{tot} - t + 1.5\ \mu m)$ with t = 2 μm being the cell thickness. Plugging in parameters for 1.9 nm diameter bismuth nanoparticles gives E_{slab}=1.45 keV. The average dose deposited in the slab section containing the nucleus is given by:

$$D_{slab} = \frac{Volume_{nucleus}}{Volume_{slab}} \times \frac{E_{slab}}{mass_{nucleus}} \quad \text{..... (8)}$$

The mass of nucleus is calculated from product of its volume and density (1.0 g/cm^3). The nDEF is obtained as follows:

$$nDEF = \frac{D_{slab} + D_w}{D_w} \quad \text{.....(9)}$$

where D_W = 2 Gy is arbitrary dose delivered to water. Plugging in values yields nDEF = 1.02 for photoelectrons and 8.24 for Auger electrons when the concentration of the particles is 7 mg/g.

6.3. Results and Discussions

Figure 6-2A shows variation of dose enhancement factor (DEF) due to photoelectrons as a function of nanoparticle concentrations for 400 nm diameter bismuth, gold and platinum nanoparticles irradiated by a 50 kVp X-ray source. For any given concentrations, bismuth nanoparticles yield the highest enhancement factor, while gold and platinum nanoparticles provide similar enhancements. This is in accordance with differences in X-ray absorption cross sections of bismuth, gold and platinum. At a concentration of 350 mg/g, bismuth nanoparticles provide 1.25 and 1.29 times higher dose enhancements than gold nanoparticles and platinum nanoparticles, respectively.

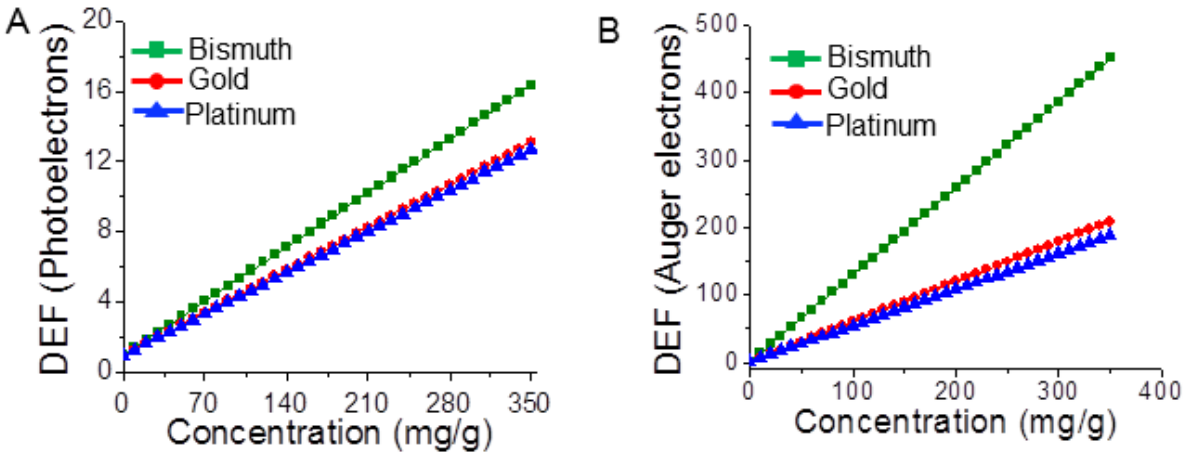

Figure 6-2 Cellular dose enhancements for different nanoparticles as a function of local nanoparticle concentration due to photoelectrons (A), Auger electrons (B) for 400 nm diameter nanoparticles irradiated by a 50 kVp external beam X-ray source.

Figure 6-2B shows variation of dose enhancement due to Auger electrons with nanoparticle concentrations. Although, DEFs due to Auger electrons increase linearly with

nanoparticle concentration, they are considerably higher than those from photoelectrons at the same concentration This is attributed to the short range (less than 1 μm) of Auger electrons, which causes them to deposit most of their energies in the vicinity of the X-ray irradiated nanoparticle. As a result of the near particle energy deposition, dose contribution within several hundred nanometers from nanoparticle is dominated by Auger electrons. Auger electrons from bismuth nanoparticles provide ~2 and 2.4 times higher enhancement than gold nanoparticles and platinum nanoparticles at 350 mg/g. Total DEFs are calculated by summing contributions from photoelectrons and Auger electrons. Table 6-1 summarizes total DEFs for three nanoparticle concentrations for each of the three types of nanoparticles having a diameter of 400 nm.

Table 6-1. Dose enhancements in endothelial cell due to photo/Auger electrons.

Nanoparticle (400 nm)	DEF (Photoelectrons)			DEF (Auger electrons)			DEF (Total)		
	7 mg/g	18 mg/g	350 mg/g	7 mg/g	18 mg/g	350 mg/g	7 mg/g	18 mg/g	350 mg/g
Bismuth	1.31	1.79	16.36	9.99	24.13	450.65	11.3	25.91	467.00
Gold	1.24	1.62	13.08	5.15	11.68	208.63	6.39	13.30	221.71
Platinum	1.23	1.60	12.73	4.74	10.62	188.01	5.97	12.22	200.71

Figure 6-3A shows effect of nanoparticle size on dose enhancement due to photoelectrons alone at 7 mg/g for three different types of nanoparticles. Enhancement factor remains constant with increase in particle size from 2-400 nm. Figure 6-3B shows enhancement factor due to Auger electrons decreases with increase in particle size. Following an ionizing event, photo or Auger electrons must escape nanoparticle before causing damage to surrounding cells; however, the percentage of electrons emitted from nanoparticle upon X-ray excitation strongly depends on

particle size, with a majority of low energy and short range Auger electrons being more readily absorbed within nanoparticle of increasing size.

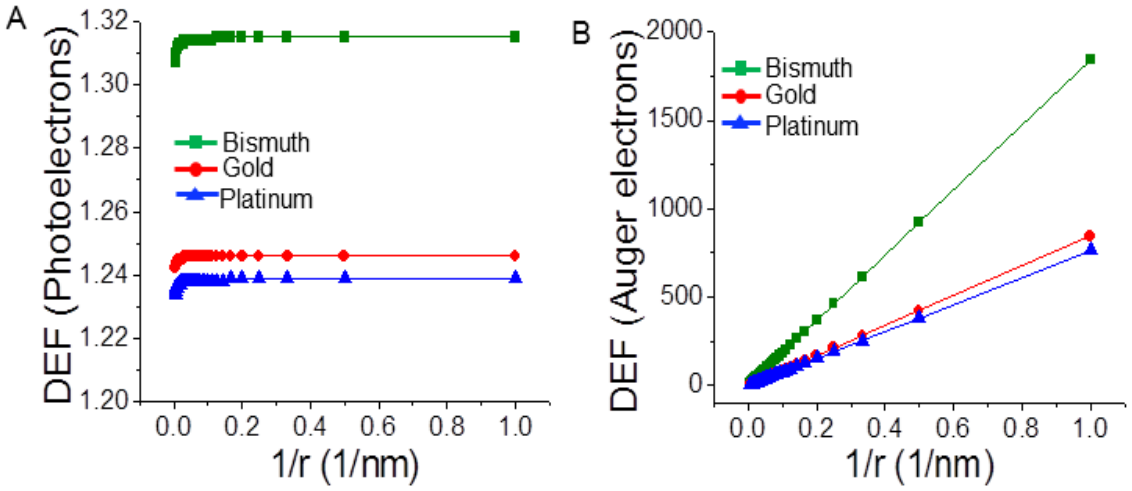

Figure 6-3 Cellular dose enhancements for different nanoparticles as a function of nanoparticle radius due to photoelectrons (A), Auger electrons (B) for 7 mg of nanoparticles per gram of tumor irradiated by a 50 kVp external beam X-ray source.

Because more Auger electrons can escape from smaller nanoparticles, the overall energy deposited to surrounding cell is higher for smaller nanoparticles, resulting in higher dose enhancements.[132] On the other hand, the percentage of energy escaping as photoelectrons and characteristic X-rays remains unchanged with increase in particle size, thereby, maintaining an almost constant dose enhancement.[125] As shown in Figure 6-3A and 6-3B, for any given size (and concentration), bismuth nanoparticles provide the maximum dose enhancement, while platinum nanoparticles have slightly lower DEFs than gold nanoparticles. The total enhancement including both Auger and photoelectrons with respect to particle size is calculated by summing the individual contributions from Auger electrons and photoelectrons.

Figure 6-4A and 6-4B show variations in nDEFs with concentrations for photoelectrons and Auger electrons, respectively, when irradiated by an external 50 kVp X-ray source Since smaller nanoparticles have high Auger electron yield (due to low self-absorption), the nanoparticle diameter used to calculate nDEF is chosen to be 1.9 nm instead of 400 nm in order to emphasize influence of Auger electrons. Bismuth nanoparticles provide the highest nDEFs for a given nanoparticle concentration, size and location.

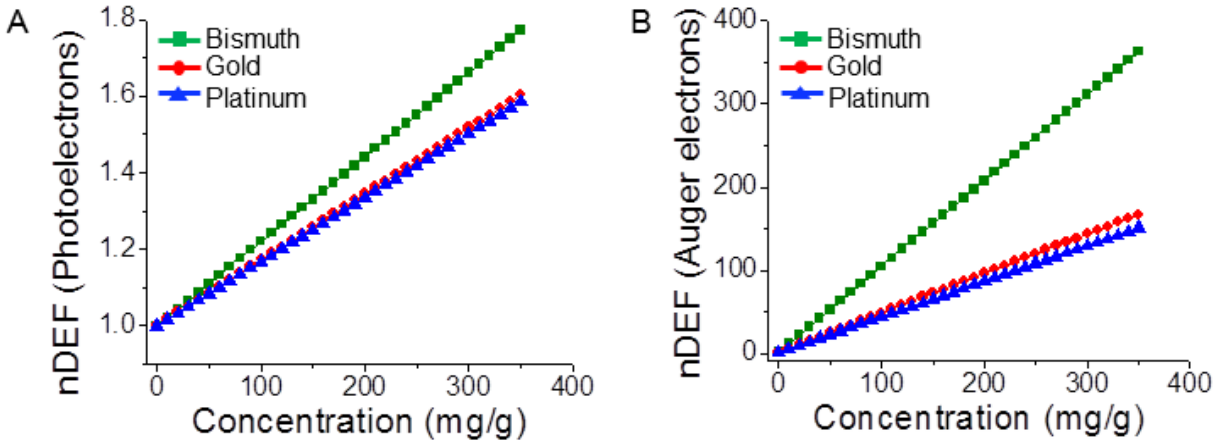

Figure 6-4 Nucleus dose enhancements for different nanoparticles as a function of local nanoparticle concentration due to photoelectrons (A), Auger electrons (B) using nanoparticles with 1.9 nm diameter where the cell exposed to 50 kVp X-rays has a nucleus occupying 10% of the cellular volume.

The total nDEFs can be obtained by adding nDEF values for photoelectrons and Auger electrons. Table 6-2 summarizes nDEFs due to photoelectrons and Auger electrons for a centrally located nucleus using three different concentrations with nanoparticle diameter of 1.9 nm.

Table 6-2. Dose enhancements in nucleus due to photo/Auger electrons.

Nanoparticle (1.9 nm)	nDEF (Photoelectrons)			nDEF (Auger electrons)			nDEF (Total)		
	7 mg/g	18 mg/g	350 mg/g	7 mg/g	18 mg/g	350 mg/g	7 mg/g	18 mg/g	350 mg/g
Bismuth	1.02	1.31	1.77	8.24	19.61	362.92	9.26	20.92	364.69
Gold	1.01	1.24	1.61	4.33	9.55	167.25	5.34	10.79	168.86
Platinum	1.01	1.23	1.59	4.00	8.70	150.75	5.01	10.29	152.34

The location dependent variation of nDEF is studied for photoelectrons and Auger electrons. The zero position is taken as the location where nanoparticle is closest to the nucleus or just inside the nucleus. Figure 6-5A and 6-5B show how nDEF varies as the nanoparticle is moved away from the nucleus, with regards to the energy distributions from photoelectrons and Auger electrons, respectively..

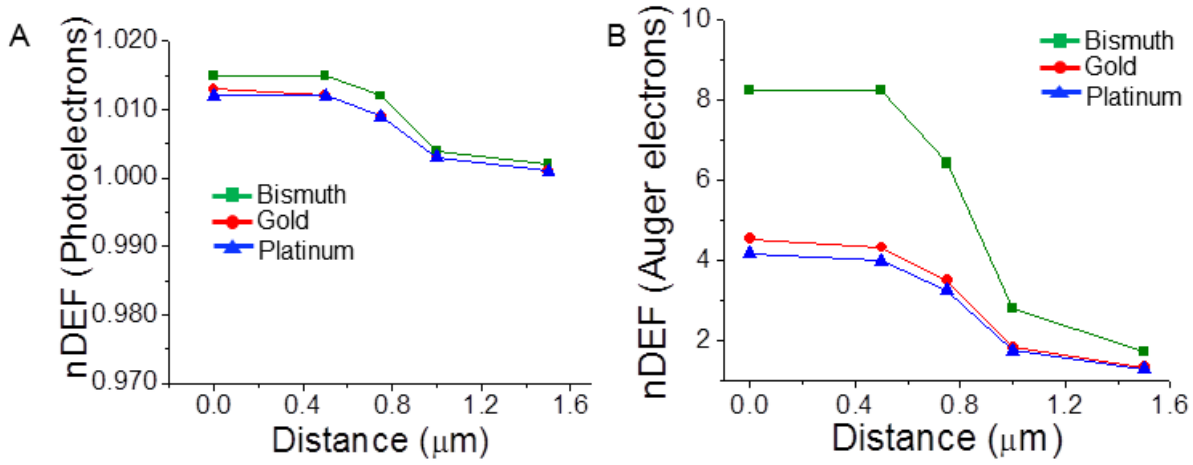

Figure 6-5 Nucleus dose enhancements for different nanoparticles as a function of distance between the nanoparticle and nucleus, due to photoelectrons (A), Auger electrons (B) for 1.9 nm diameter nanoparticles (at 7 mg/g) when irradiated by a 50 kVp external beam X-ray source where the nucleus occupies 10% of the cellular volume. Zero distance refers to the position when the nanoparticle is just inside the nucleus.

The concentration of nanoparticles is chosen to be 7 mg/g. The long-range photoelectrons deposit their energy relatively uniformly over the entire cell volume with nDEF remaining fairly constant as the nanoparticle is moved away from the nucleus. In contrast, short range Auger electrons deposit more energy closer to the nanoparticles; therefore, the highest nDEFs are achieved for nanoparticles that are located closest to the nucleus. Results summarized in Table 6-1 and 6-2, confirm that for any given nanoparticle concentration, size or location, bismuth nanoparticles offer significantly higher dose enhancements for both cell and nucleus compared to gold nanoparticles and platinum nanoparticles when irradiated by a typical low energy 50 kVp diagnostic X-ray source.

Figures 6-6A-C show how the cellular dose enhancements due to photoelectrons alone depend on energy of irradiating X-ray sources at different particle concentrations for bismuth, gold and platinum nanoparticles, respectively. For each type of particle, the diameter is taken as 400 nm. Figure 6-6D shows the results obtained at nanoparticle concentration of 350 mg/g. In addition to the 50 kVp source, X-ray sources with ratings of 110 kVp (average energy ~40 keV)[144] and 300 kVp (average energy ~100 keV)[125] are used to study the energy dependence of cellular dose enhancements. Our results are consistent with earlier studies[125] that used Monte Carlo simulations and reveal a general trend of increasing dose enhancement with decreasing energy of X-ray sources for a given nanoparticle type.

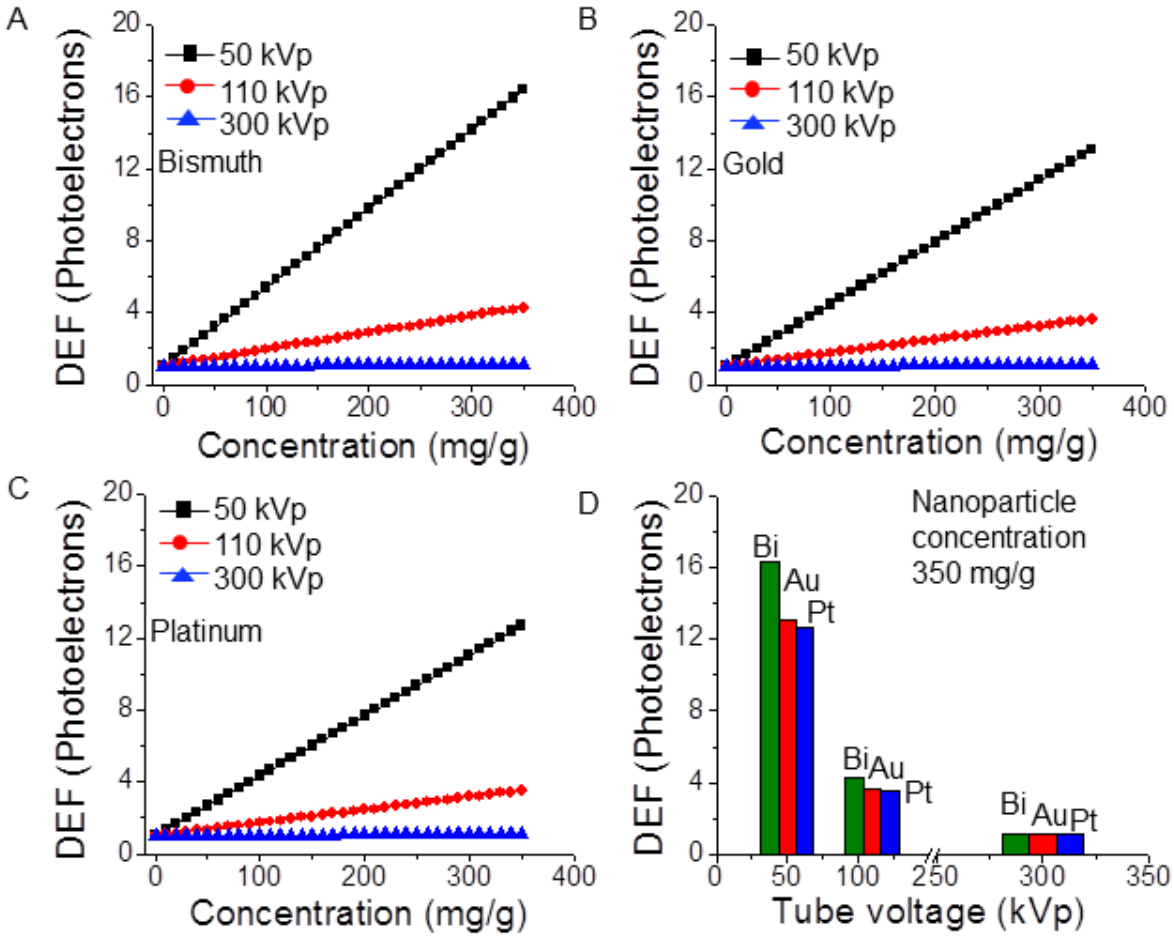

Figure 6-6 Endothelial cell dose enhancement factor (DEF) as a function of local nanoparticle concentration due to photoelectrons alone at different X-ray tube voltages for bismuth (A), platinum (B) and gold (C) nanoparticles; endothelial cell dose enhancement factor (DEF) due to photoelectrons alone for three different X-ray sources when the nanoparticle concentration is 350 mg/g (D).

The k-edge energies of bismuth, gold and platinum are 91, 81 and 78 keV, respectively. The 50 kVp and 110 kVp sources have average energies below k-edge while 300 kVp source has an average energy above k-edge of particles. An abrupt increase in photoelectric absorption coefficients is observed only when the average energy of the primary X-ray photons matches k-edge energies or when a monochromatic X-ray source with the same energy as k-edge of

nanoparticles is used. Low energy diagnostic X-ray sources are therefore ideal for nanoparticle enhanced therapeutic applications, particularly for treatment of surface cancers. However, treating deeply buried cancers would still require high energy X-ray beams that can penetrate deeper inside the body.

6.4 Conclusion

In this work, an analytical approach is adopted to obtain dose enhancements for tumor cells and their nuclei using bismuth, gold and platinum nanoparticles. Energy depositions from both photoelectrons and Auger electrons, generated by X-ray irradiation of nanoparticles have been considered. The dependence of dose enhancements on nanoparticle material composition, location, size, and concentration, as well as the energy of irradiating X-ray photons, are derived based on the mathematical model. Maximum dose enhancements are achieved in the case of bismuth nanoparticles; smaller nanoparticles coupled with low energy external beam X-ray sources can greatly enhance dose delivered to cell or nucleus with maximum enhancements being obtained for particles that are located closest to the nucleus. While, this study indicates the use of bismuth and platinum as a potential alternative to gold in nanoparticle aided radiation therapy of cancer, further studies are warranted to investigate X-ray induced DNA damage, toxicity and biocompatibility of these particles before the proposed method can be put into practical use.

CHAPTER 7: SUMMARY AND FUTURE WORK

7.1 Summary

A novel strategy has been developed for cancer detection and treatment using X-rays and nanoparticles. Multiple DNA and protein biomarkers have been detected based on characteristic X-ray fluorescence of a panel of metal and alloy nanoparticles, which are modified with ligands of biomarkers to create a one-to-one correspondence and immobilized on ligand-modified substrates after forming complexes with target biomarkers in three strand or sandwich configurations. By determining the presence and concentration of nanoparticles using X-ray fluorescence, the nature and amount of biomarkers can be detected with limits of 1 nM for DNA and 1 ng/ml for protein. Multiplexed biomarker detection allows early and accurate detection of cancer, thereby greatly increasing the reliability of prognosis. By combining high penetrating ability of X-rays, this method can allow quantitative imaging of multiple biomarkers *in-vivo*.

A new nanoparticle-enabled technique for integrated enrichment, detection and killing of circulating tumor cells or CTCs, *in-vitro*, has been demonstrated by using magnetic nanoparticles and bismuth nanoparticles, X-ray fluorescence spectrometry, and X-ray radiation. Results show that the method is capable of selectively detecting CTCs with high specificities, at concentrations ranging from 100-100,000 cells/ml in the buffer solution and achieving detection limit of ~100 CTCs/ml. Further improvements can be made to reach lower detection limits Detection of CTCs in whole human blood has also been demonstrated. Moreover, in this integrated approach, the dose of primary X-rays can be tuned to kill more than 80% of the localized CTCs by radiation

induced DNA damage where the killing effect is significantly enhanced by the use of X-ray absorbing metallic nanoparticles. Being highly selective to cancer cells, the method causes no damage to normal healthy cells, thus making *in vivo* personalized CTC management possible.

In-vitro cytotoxicity of bismuth nanoparticles is studied by three complementary assays (MTT, G6PD, and Calcein AM/EthD-1). Concentration dependent cytotoxicities have been observed for bismuth nanoparticles and surface modified bismuth nanoparticles. The bismuth nanoparticles are non-toxic at concentrations of 0.5 nM or lower. Nanoparticles at high concentration (50 nM) kill 45%, 52%, 41%, 34% HeLa cells for bare nanoparticles, amine terminated bismuth nanoparticle, silica coated bismuth nanoparticle, and polyethylene glycol (PEG) modified bismuth nanoparticle, respectively; which indicates cytotoxicity in terms of cell viability is in the descending order of amine terminated bismuth nanoparticles, bare bismuth nanoparticles, silica coated bismuth nanoparticles, and PEG modified bismuth nanoparticles. HeLa cells are more susceptible to toxicity from bismuth nanoparticles than MG-63 cells. The simultaneous use of three toxicity assays provides useful information on how nanoparticles interact with cells. The findings have important implications for caution of nanoparticle exposure and evaluating toxicity of bismuth nanoparticles for future *in-vivo* applications.

An image-based, on-chip microtissue radiation biodosimeter has been designed and fabricated that can simultaneously monitor radiation responses of multiple mammalian cell types. The microtissue chip is fabricated by molding molten agarose gel onto microfabricated patterns to form microwells, and seeding a variety of cell suspensions into different microwells inside the agarose gel. After X-ray irradiation, the cells are stained with trypan blue dye which changes color upon X-ray irradiation indicating cell death. The camera of a mobile phone is used to

collect images of an array of microtissues, where the subsequent color changes of microtissues upon X-ray irradiation allows accurate determination of cell death. The intensity of the color is directly related to amount of radiation dose and the number of cell deaths. The images can be transferred wirelessly to a lab for further analysis, allowing the biodosimeter to be used for convenient field deployable monitoring of radiation exposure. The biodosimeter can be used for simultaneous and accurate monitoring of radiation responses of multiple mammalian cells in X-ray radiation therapy of cancer.

An analytical approach has been used to calculate dose enhancements to tumor endothelial cells and their nuclei for a series of nanoparticles (bismuth, gold and platinum) located at different locations relative to nuclei by considering contributions from both photoelectrons and Auger electrons. Dose enhancement factors or DEFs depend on material composition, size and location of nanoparticles with respect to the cell and the nucleus. Energy of irradiating X-ray beam affects X-ray absorption by nanoparticles and plays an important role in dose enhancements. For typical diagnostic X-ray sources, bismuth nanoparticles provide higher dose enhancements than gold and platinum nanoparticles for a given nanoparticle size, concentration and location. The highest DEFs are achieved for nanoparticles located closest to the nucleus where energy depositions from short range Auger electrons are at maximum. With nanoparticles ranging in diameter between 2-400 nm, the dose enhancement increases with decrease in particle size. The results will be useful in finding optimized conditions for nanoparticle enhanced X-ray radiation therapy of cancer.

7.2 Future Work

Future study is intended to determine the effectiveness of a class of novel nanoparticles for cancer imaging and therapy in mice using X-rays. In order to develop a system for selective local delivery of nanoparticles to tumors, for effective diagnosis and treatment, the various techniques demonstrated in this dissertation work will be tested *in vivo*. This will help to better understand the complex relationships involved in tumor growth and invasion and how this is affected by X-rays and nanoparticles under *in vivo* conditions. In addition to aiding tumor imaging, these nanoparticles can also act as radiosensitizers localizing X-ray dose within the tumors. Tumors will be grown subcutaneously in mice and, nanoparticles, modified to target specific receptors on the tumor surface, will be injected. X-ray imaging will be performed to study the contrast enhancements provided by different nanoparticles for visualization of tumors. Following X-ray irradiation; tumor size will be monitored for possible therapeutic applications of these internalized nanoparticles. The *in vivo* experiments are expected to validate the findings obtained from the theoretical studies on nanoparticle aided X-ray radiation therapy.

APPENDIX: REFEREED JOURNAL PUBLICATIONS

1. **M. Hossain**, M. Su, Nanoparticle location and material dependent dose enhancement in X-ray radiation therapy, *J. Phys. Chem. C,* **2012,** *116,* 23047.

2. Y. Luo, **M. Hossain**, C. Wang, Y. Qiao, L. Ma, M. Su, Targeted nanoparticles for enhanced X-ray radiation killing of multidrug-resistant bacteria, **2012,** under preparation.

3. **M. Hossain**, Y. Luo, Z. Sun, C. Wang, M. Zhang, H. Fu, M. Su, X-ray enabled detection and eradication of circulating tumor cells with nanoparticles, *Biosens. Bioelectron*., **2012,** *38,* 348.

4. Y. Luo, C. Wang, Y. Qiao, **M. Hossain,** L. Ma, M. Su, In vitro cytotoxicity of surface modified bismuth nanoparticles, *J. Mater. Sci.- Mater. Med.*, **2012,** *23,* 2563.

5. Y. Luo, C. Wang, **M. Hossain,** Y. Qiao, L. Ma, J. An, M. Su, Three-dimensional microtissue assay for high-throughput cytotoxicity of nanoparticles, *Anal. Chem.,* **2012,** *84,* 6731.

6. Y. Luo*, **M. Hossain*,** C. Wang, Y. Qiao, L. Ma, M. Su, On-chip radiation biodosimetry with three-dimensional microtissues, *Analyst,* **2012**, *137*, 3441 [*equal contribution].

7. C. Wang, Y. Hong, M. Zhang, **M. Hossain,** Y. Luo, M. Su, Thermal fingerprint of silica encapsulated phase change nanoparticles, *Nanoscale,* **2012,** *4,* 3237.

8. **M. Hossain**, C.Wang, M. Su, Multiplexed biomarker detection using X-ray fluorescence of composition-encoded nanoparticles, *Appl. Phys. Lett.*, **2010,** *97,* 263704.

9. C. Wang*, **M. Hossain*,** L. Ma, M. Su, Highly sensitive thermal detection of thrombin using aptamer-functionalized phase change nanoparticles, *Biosens. Bioelectron.,* **2010,** *26,* 437 [*equal contribution].

10. C. Wang, L. Ma, **M. Hossain,** M. Zhang, H. Wang, S. Zou, J. Hickman, and M. Su, Visual detections of molecular thin films on plasmonic nanoparticle arrays, *Sensor Actuat B-Chem.,***2010,** *150,* 637.

REFERENCES

1. http://www.cancer.gov/cancertopics/cancerlibrary/what-is-cancer.

2. http://www.who.int/mediacentre/factsheets/fs297/en/.

3. Cao, Y.; DePinho, R. A.; Ernst, M.; Vousden, K., Cancer research: past, present and future. *Nat. Rev. Cancer* **2011,** *11*, 749.

4. Wulfkuhle, J. D.; Liotta, L. A.; Petricoin, E. F., Proteomic applications for the early detection of cancer. *Nat. Rev. Cancer* **2003,** *3*, 267.

5. Heimann, R.; Hellman, S., Clinical progression of breast cancer malignant behavior: what to expect and when to expect it. *J. Clin. Oncol.* **2000,** *18*, 591.

6. nano.cancer.gov/objects/pdfs/Cancer_brochure_091609-508.pdf.

7. Nie, S.; Xing, Y.; Kim, G. J.; Simons, J. W., Nanotechnology Applications in Cancer. *Annu. Rev. of Biomed. Eng.* **2007,** *9*, 257.

8. Fass, L., Imaging and cancer: A review. *Mol. oncol.* **2008,** *2*, 115.

9. Phan, J. H.; Moffitt, R. A.; Stokes, T. H.; Liu, J.; Young, A. N.; Nie, S.; Wang, M. D., Convergence of biomarkers, bioinformatics and nanotechnology for individualized cancer treatment. *Trends Biotechnol.* **2009,** *27*, 350.

10. Wei, F.; Patel, P.; Liao, W.; Chaudhry, K.; Zhang, L.; Arellano-Garcia, M.; Hu, S.; Elashoff, D.; Zhou, H.; Shukla, S.; Shah, F.; Ho, C.-M.; Wong, D. T., Electrochemical sensor for multiplex biomarkers detection. *Clin. Cancer. Res.* **2009,** *15*, 4446.

11. Arellano-Garcia, M.; Hu, S.; Wang, J.; Henson, B.; Zhou, H.; Chia, D.; Wong, D. T., Multiplexed immunobead-based assay for detection of oral cancer protein biomarkers in saliva. *Oral Dis.* **2008,** *14*, 705.

12. Magalhaes, T.; Carvalho, M. L.; Von Bohlen, A.; Becker, M., Study on trace elements behaviour in cancerous and healthy tissues of colon, breast and stomach: Total reflection X-ray fluorescence applications. *Spectroc. Acta Pt. B-Atom. Spectr.* **2010,** *65*, 493.

13. Silva, M. P.; Tomal, A.; Pérez, C. A.; Ribeiro-Silva, A.; Poletti, M. E., Determination of Ca, Fe, Cu and Zn and their correlations in breast cancer and normal adjacent tissues. *X-ray Spectrom.* **2009,** *38*, 103.

14. Hayashi, Y.; Okuyama, F., New approach to breast tumor detection based on fluorescence X-ray analysis. *Ger. Med. Sci.* **2010,** *8*.

15. Banas, A.; Kwiatek, W. M.; Banas, K.; Gajda, M.; Pawlicki, B.; Cichocki, T., Correlation of concentrations of selected trace elements with Gleason grade of prostate tissues. *J. Biol. Inorg. Chem.* **2010,** *15*, 1147.

16. Geraki, K.; Farquharson, M. J.; Bradley, D. A., X-ray fluorescence and energy dispersive X-ray diffraction for the quantification of elemental concentrations in breast tissue. *Phys. Med. Biol.* **2004,** *49*, 99.

17. Börjesson, J.; Mattsson, S., Medical applications of X-ray fluorescence for trace element research. *Powder Diffr.* **2007,** *22*, 130.

18. Nie, H.; Chettle, D.; Luo, L.; O'Meara, J., Dosimetry study for a new in vivo X-ray fluorescence (XRF) bone lead measurement system. *Nucl. Instrum. Meth. B* **2007,** *263*, 225.

19. Todd, A. C.; Chettle, D. R., In-vivo X-ray-fluorescence of lead in bone - review and current issues. *Environ. Health Perspect.* **1994,** *102*, 172.

20. Karabulut, A.; Gürol, A., Measurements of L XRF fluorescence cross-sections and relative intensity ratios for some elements in the atomic range 72 ⩽ Z ⩽92. *Nucl. Instrum. Meth. B* **2006,** *244*, 303.

21. Servomaa, A.; Tapiovaara, M., Organ dose calculation in medical X ray examinations by the program PCXMC. *Radiat. Prot. Dosim.* **1998,** *80*, 213.

22. Kaiser, J., Cancer's circulation problem. *Science* **2010,** *327*, 1072.

23. Sun, Y. F.; Yang, X. R.; Zhou, J.; Qiu, S. J.; Fan, J.; Xu, Y., Circulating tumor cells: advances in detection methods, biological issues, and clinical relevance. *J. Cancer Res. Clin. Oncol.* **2011,** *137*, 1151.

24. Nezos, A.; Msaouel, P.; Pissimissis, N.; Lembessis, P.; Sourla, A.; Armakolas, A.; Gogas, H.; Stratigos, A. J.; Katsambas, A. D.; Koutsilieris, M., Methods of detection of circulating melanoma cells: a comparative overview. *Cancer Treat. Rev.* **2011,** *37*, 284.

25. Liu, M. C.; Shields, P. G.; Warren, R. D.; Cohen, P.; Wilkinson, M.; Ottaviano, Y. L.; Rao, S. B.; Eng-Wong, J.; Seillier-Moiseiwitsch, F.; Noone, A. M.; Isaacs, C., Circulating tumor cells: a useful predictor of treatment efficacy in metastatic breast cancer. *J. Clin. Oncol.* **2009,** *27*, 5153.

26. Yu, M.; Stott, S.; Toner, M.; Maheswaran, S.; Haber, D. A., Circulating tumor cells: approaches to isolation and characterization. *J. Cell Biol.* **2011,** *192*, 373.

27. Zemp, R. J., Nanomedicine: detecting rare cancer cells. *Nat. Nanotechnol.* **2009,** *4*, 798.

28. Pantel, K.; Brakenhoff, R. H.; Brandt, B., Detection, clinical relevance and specific biological properties of disseminating tumour cells. *Nat. Rev. Cancer* **2008,** *8*, 329.

29. Nagrath, S.; Sequist, L. V.; Maheswaran, S.; Bell, D. W.; Irimia, D.; Ulkus, L.; Smith, M. R.; Kwak, E. L.; Digumarthy, S.; Muzikansky, A.; Ryan, P.; Balis, U. J.; Tompkins, R. G.; Haber, D. A.; Toner, M., Isolation of rare circulating tumour cells in cancer patients by microchip technology. *Nature* **2007,** *450*, 1235.

30. He, W.; Wang, H. F.; Hartmann, L. C.; Cheng, J. X.; Low, P. S., In vivo quantitation of rare circulating tumor cells by multiphoton intravital flow cytometry. *Proc. Natl. Acad. Sci. U. S. A.* **2007,** *104*, 11760.

31. Dharmasiri, U.; Njoroge, S. K.; Witek, M. A.; Adebiyi, M. G.; Kamande, J. W.; Hupert, M. L.; Barany, F.; Soper, S. A., High-throughput selection, enumeration, electrokinetic manipulation, and molecular profiling of low-abundance circulating tumor cells using a microfluidic system. *Anal. Chem.* **2011,** *83*, 2301.

32. Wang, S.; Liu, K.; Liu, J.; Yu, Z. T.; Xu, X.; Zhao, L.; Lee, T.; Lee, E. K.; Reiss, J.; Lee, Y. K.; Chung, L. W.; Huang, J.; Rettig, M.; Seligson, D.; Duraiswamy, K. N.; Shen, C. K.; Tseng, H. R., Highly efficient capture of circulating tumor cells by using nanostructured silicon substrates with integrated chaotic micromixers. *Angew. Chem., Int. Ed.* **2011,** *50*, 3084.

33. Bilkenroth, U.; Taubert, H.; Riemann, D.; Rebmann, U.; Heynemann, H.; Meye, A., Detection and enrichment of disseminated renal carcinoma cells from peripheral blood by immunomagnetic cell separation. *Int. J. Cancer* **2001,** *92*, 577.

34. Benez, A.; Geiselhart, A.; Handgretinger, R.; Schiebel, U.; Fierlbeck, G., Detection of circulating melanoma cells by immunomagnetic cell sorting. *J. Clin. Lab. Anal.* **1999,** *13*, 229.

35. Zborowski, M.; Chalmers, J. J., Rare cell separation and analysis by magnetic sorting. *Anal. Chem.* **2011,** *83*, 8050.

36. Zheng, S.; Lin, H. K.; Lu, B.; Williams, A.; Datar, R.; Cote, R. J.; Tai, Y. C., 3D microfilter device for viable circulating tumor cell (CTC) enrichment from blood. *Biomed. Microdevices* **2011,** *13*, 203.

37. Zheng, S.; Lin, H.; Liu, J. Q.; Balic, M.; Datar, R.; Cote, R. J.; Tai, Y. C., Membrane microfilter device for selective capture, electrolysis and genomic analysis of human circulating tumor cells. *J. Chromatogr. A* **2007,** *1162*, 154.

38. Lin, H. K.; Zheng, S.; Williams, A. J.; Balic, M.; Groshen, S.; Scher, H. I.; Fleisher, M.; Stadler, W.; Datar, R. H.; Tai, Y. C.; Cote, R. J., Portable filter-based microdevice for detection and characterization of circulating tumor cells. *Clin. Cancer Res.* **2010,** *16*, 5011.

39. Gascoyne, P. R.; Noshari, J.; Anderson, T. J.; Becker, F. F., Isolation of rare cells from cell mixtures by dielectrophoresis. *Electrophoresis* **2009,** *30*, 1388.

40. Hu, Y.; Fan, L.; Zheng, J.; Cui, R.; Liu, W.; He, Y.; Li, X.; Huang, S., Detection of circulating tumor cells in breast cancer patients utilizing multiparameter flow cytometry and assessment of the prognosis of patients in different CTCs levels. *Cytometry A* **2010,** *77*, 213.

41. Zharov, V. P.; Galanzha, E. I.; Shashkov, E. V.; Khlebtsov, N. G.; Tuchin, V. V., In vivo photoacoustic flow cytometry for monitoring of circulating single cancer cells and contrast agents. *Opt. Lett.* **2006,** *31*, 3623.

42. Georgakoudi, I.; Solban, N.; Novak, J.; Rice, W. L.; Wei, X.; Hasan, T.; Lin, C. P., In vivo flow cytometry: a new method for enumerating circulating cancer cells. *Cancer Res.* **2004,** *64*, 5044.

43. Kojima, T.; Hashimoto, Y.; Watanabe, Y.; Kagawa, S.; Uno, F.; Kuroda, S.; Tazawa, H.; Kyo, S.; Mizuguchi, H.; Urata, Y.; Tanaka, N.; Fujiwara, T., A simple biological imaging system for detecting viable human circulating tumor cells. *J. Clin. Invest.* **2009,** *119*, 3172.

44. Hsieh, H. B.; Marrinucci, D.; Bethel, K.; Curry, D. N.; Humphrey, M.; Krivacic, R. T.; Kroener, J.; Kroener, L.; Ladanyi, A.; Lazarus, N.; Kuhn, P.; Bruce, R. H.; Nieva, J., High speed detection of circulating tumor cells. *Biosens. Bioelectron.* **2006,** *21*, 1893.

45. Galanzha, E. I.; Shashkov, E. V.; Kelly, T.; Kim, J. W.; Yang, L.; Zharov, V. P., In vivo magnetic enrichment and multiplex photoacoustic detection of circulating tumour cells. *Nat. Nanotechnol.* **2009,** *4*, 855.

46. Nedosekin, D. A.; Sarimollaoglu, M.; Shashkov, E. V.; Galanzha, E. I.; Zharov, V. P., Ultra-fast photoacoustic flow cytometry with a 0.5 MHz pulse repetition rate nanosecond laser. *Opt. Express* **2010,** *18*, 8605.

47. Weight, R. M.; Viator, J. A.; Dale, P. S.; Caldwell, C. W.; Lisle, A. E., Photoacoustic detection of metastatic melanoma cells in the human circulatory system. *Opt. Lett.* **2006,** *31*, 2998.

48. Gutierrez-Juarez, G.; Gupta, S. K.; Weight, R. M.; Polo-Parada, L.; Papagiorgio, C.; Bunch, J. D.; Viator, J. A., Optical Photoacoustic Detection of Circulating Melanoma Cells In Vitro. *Int. J. Thermophys.* **2010,** *31*, 784.

49. Chung, Y. K.; Reboud, J.; Lee, K. C.; Lim, H. M.; Lim, P. Y.; Wang, K. Y.; Tang, K. C.; Ji, H.; Chen, Y., An electrical biosensor for the detection of circulating tumor cells. *Biosens. Bioelectron.* **2011,** *26*, 2520.

50. Sha, M. Y.; Xu, H.; Natan, M. J.; Cromer, R., Surface-enhanced Raman scattering tags for rapid and homogeneous detection of circulating tumor cells in the presence of human whole blood. *J. Am. Chem. Soc.* **2008,** *130*, 17214.

51. Wang, X.; Qian, X.; Beitler, J. J.; Chen, Z. G.; Khuri, F. R.; Lewis, M. M.; Shin, H. J.; Nie, S.; Shin, D. M., Detection of circulating tumor cells in human peripheral blood using surface-enhanced Raman scattering nanoparticles. *Cancer Res.* **2011,** *71*, 1526.

52. Neugebauer, U.; Bocklitz, T.; Clement, J. H.; Krafft, C.; Popp, J., Towards detection and identification of circulating tumour cells using Raman spectroscopy. *Analyst* **2010,** *135*, 3178.

53. Hossain, M.; Wang, C.; Su, M., Multiplexed biomarker detection using X-ray fluorescence of composition-encoded nanoparticles. *Appl. Phys. Lett.* **2010,** *97*, 263704.

54. Mann, S. E.; Ringo, M. C.; Shea-McCarthy, G.; Penner-Hahn, J.; Evans, C. E., Element-specific detection in capillary electrophoresis using X-ray fluorescence spectroscopy. *Anal. Chem.* **2000,** *72*, 1754.

55. Hatzistavros, V. S.; Koulouridakis, P. E.; Aretaki, II; Kallithrakas-Kontos, N. G., Bromate determination in water after membrane complexation and total reflection X-ray fluorescence analysis. *Anal. Chem.* **2007,** *79*, 2827.

56. Rabin, O.; Manuel Perez, J.; Grimm, J.; Wojtkiewicz, G.; Weissleder, R., An X-ray computed tomography imaging agent based on long-circulating bismuth sulphide nanoparticles. *Nat. Mater.* **2006,** *5*, 118.

57. Bhattacharya, D.; Das, M.; Mishra, D.; Banerjee, I.; Sahu, S. K.; Maiti, T. K.; Pramanik, P., Folate receptor targeted, carboxymethyl chitosan functionalized iron oxide nanoparticles: a novel ultradispersed nanoconjugates for bimodal imaging. *Nanoscale* **2011,** *3*, 1653.

58. Zhang, Y.; Kohler, N.; Zhang, M. Q., Surface modification of superparamagnetic magnetite nanoparticles and their intracellular uptake. *Biomaterials* **2002,** *23*, 1553.

59. Hainfeld, J. F.; Slatkin, D. N.; Smilowitz, H. M., The use of gold nanoparticles to enhance radiotherapy in mice. *Phys. Med. Biol.* **2004,** *49*, N309.

60. Rahman, W. N.; Bishara, N.; Ackerly, T.; He, C. F.; Jackson, P.; Wong, C.; Davidson, R.; Geso, M., Enhancement of radiation effects by gold nanoparticles for superficial radiation therapy. *Nanomedicine* **2009,** *5*, 136.

61. Ngwa, W.; Makrigiorgos, G. M.; Berbeco, R. I., Gold nanoparticle-aided brachytherapy with vascular dose painting: Estimation of dose enhancement to the tumor endothelial cell nucleus. *Med. Phys.* **2012,** *39*, 392.

62. Karlsson, H. L., The comet assay in nanotoxicology research. *Anal. Bioanal. Chem.* **2010,** *398*, 651.

63. Qiao, Y.; Wang, C.; Su, M.; Ma, L., Single Cell DNA Damage/Repair Assay Using HaloChip. *Anal. Chem.* **2012,** *84*, 1112.

64. Sonvico, F.; Mornet, S.; Vasseur, S.; Dubernet, C.; Jaillard, D.; Degrouard, J.; Hoebeke, J.; Duguet, E.; Colombo, P.; Couvreur, P., Folate-conjugated iron oxide nanoparticles for solid tumor targeting as potential specific magnetic hyperthermia mediators: synthesis, physicochemical characterization, and in vitro experiments. *Bioconjugate Chem.* **2005,** *16*, 1181.

65. Larsen, A.; Martiny, M.; Stoltenberg, M.; Danscher, G.; Rungby, J., Gastrointestinal and systemic uptake of bismuth in mice after oral exposure. *Pharmacol. Toxicol.* **2003,** *93*, 82.

66. Andrews, P. C.; Ferrero, R. L.; Forsyth, C. M.; Junk, P. C.; Maclellan, J. G.; Peiris, R. M., Bismuth(III) Saccharinate and Thiosaccharinate Complexes and the Effect of Ligand Substitution on Their Activity against Helicobacter pylori. *Organometallics* **2011,** *30*, 6283.

67. Gisbert, J. P., Helicobacter pylori eradication: A new, single-capsule bismuth-containing quadruple therapy. *Nat. Rev.Gastroenterol. Hepatol.* **2011,** *8*, 307.

68. Malfertheiner, P.; Bazzoli, F.; Delchier, J. C.; Celinski, K.; Giguere, M.; Riviere, M.; Megraud, F., Helicobacter pylori eradication with a capsule containing bismuth subcitrate potassium, metronidazole, and tetracycline given with omeprazole versus clarithromycin-based triple therapy: a randomised, open-label, non-inferiority, phase 3 trial. *Lancet* **2011,** *377*, 905.

69. Rosenblat, T. L.; McDevitt, M. R.; Mulford, D. A.; Pandit-Taskar, N.; Divgi, C. R.; Panageas, K. S.; Heaney, M. L.; Chanel, S.; Morgenstern, A.; Sgouros, G.; Larson, S. M.; Scheinberg, D. A.; Jurcic, J. G., Sequential cytarabine and alpha-particle immunotherapy with bismuth-213-lintuzumab (HuM195) for acute myeloid leukemia. *Clin. Cancer Res.* **2010,** *16*, 5303.

70. Leussink, B. T.; Baelde, H. J.; Broekhuizen-van den Berg, T. M.; de Heer, E.; van der Voet, G. B.; Slikkerveer, A.; Bruijn, J. A.; de Wolff, F. A., Renal epithelial gene expression profile and bismuth-induced resistance against cisplatin nephrotoxicity. *Hum. Exp. Toxicol.* **2003,** *22*, 535.

71. Kinsella, J. M.; Jimenez, R. E.; Karmali, P. P.; Rush, A. M.; Kotamraju, V. R.; Gianneschi, N. C.; Ruoslahti, E.; Stupack, D.; Sailor, M. J., X-ray computed tomography imaging of breast cancer by using targeted peptide-labeled bismuth sulfide nanoparticles. *Angew. Chem. Int. Ed.* **2011,** *50*, 12308.

72. Ding, S. N.; Shan, D.; Xue, H. G.; Cosnier, S., A promising biosensing-platform based on bismuth oxide polycrystalline-modified electrode: characterization and its application in development of amperometric glucose sensor. *Bioelectrochemistry* **2010,** *79*, 218.

73. Ma, L.; Hong, Y.; Ma, Z.; Kaittanis, C.; Perez, J. M.; Su, M., Multiplexed highly sensitive detections of cancer biomarkers in thermal space using encapsulated phase change nanoparticles. *Appl. Phys. Lett.* **2009,** *95*, 043701.

74. Wang, C.; Sun, Z.; Ma, L.; Su, M., Simultaneous detection of multiple biomarkers with over three orders of concentration difference using phase change nanoparticles. *Anal. Chem.* **2011,** *83*, 2215.

75. Wang, L.; Nagesha, D. K.; Selvarasah, S.; Dokmeci, M. R.; Carrier, R. L., Toxicity of CdSe Nanoparticles in Caco-2 Cell Cultures. *J. Nanobiotechnology* **2008,** *6*, 11.

76. Clift, M. J.; Rothen-Rutishauser, B.; Brown, D. M.; Duffin, R.; Donaldson, K.; Proudfoot, L.; Guy, K.; Stone, V., The impact of different nanoparticle surface chemistry and size on uptake and toxicity in a murine macrophage cell line. *Toxicol. Appl. Pharmacol* . **2008,** *232*, 418.

77. Zhu, Z. J.; Carboni, R.; Quercio, M. J., Jr.; Yan, B.; Miranda, O. R.; Anderton, D. L.; Arcaro, K. F.; Rotello, V. M.; Vachet, R. W., Surface properties dictate uptake, distribution, excretion, and toxicity of nanoparticles in fish. *Small* **2010,** *6*, 2261.

78. Hoshino, A.; Hanada, S.; Yamamoto, K., Toxicity of nanocrystal quantum dots: the relevance of surface modifications. *Arch. Toxicol.* **2011,** *85*, 707.

79. Selim, K. K.; Xing, Z. C.; Choi, M. J.; Chang, Y.; Guo, H.; Kang, I. K., Reduced cytotoxicity of insulin-immobilized CdS quantum dots using PEG as a spacer. *Nanoscale Res. Lett* . **2011,** *6*, 528.

80. Zhang, X. D.; Wu, D.; Shen, X.; Liu, P. X.; Yang, N.; Zhao, B.; Zhang, H.; Sun, Y. M.; Zhang, L. A.; Fan, F. Y., Size-dependent in vivo toxicity of PEG-coated gold nanoparticles. *Int. J. Nanomed.* **2011,** *6*, 2071.

81. Cho, W. S.; Cho, M. J.; Jeong, J.; Choi, M.; Cho, H. Y.; Han, B. S.; Kim, S. H.; Kim, H. O.; Lim, Y. T.; Chung, B. H.; Jeong, J., Acute toxicity and pharmacokinetics of 13 nm-sized PEG-coated gold nanoparticles. *Toxicol. Appl. Pharmacol* . **2009,** *236*, 16.

82. Malugin, A.; Ghandehari, H., Cellular uptake and toxicity of gold nanoparticles in prostate cancer cells: a comparative study of rods and spheres. *J. Appl. Toxicol* . **2010,** *30*, 212.

83. Nair, S.; Sasidharan, A.; Divya Rani, V. V.; Menon, D.; Manzoor, K.; Raina, S., Role of size scale of ZnO nanoparticles and microparticles on toxicity toward bacteria and osteoblast cancer cells. *J. Mater. Sci. - Mater. Med.* **2009,** *20 Suppl 1*, S235.

84. Wang, H.; Wingett, D.; Engelhard, M. H.; Feris, K.; Reddy, K. M.; Turner, P.; Layne, J.; Hanley, C.; Bell, J.; Tenne, D.; Wang, C.; Punnoose, A., Fluorescent dye encapsulated ZnO particles with cell-specific toxicity for potential use in biomedical applications. *J. Mater. Sci. - Mater. Med.* **2009,** *20*, 11.

85. Zhao, Y.; Lin, K.; Zhang, W.; Liu, L., Quantum dots enhance Cu^{2+}-induced hepatic L02 cells toxicity. *J. Environ. Sci.* **2010,** *22*, 1987.

86. Mahmoudi, M.; Simchi, A.; Imani, M.; Milani, A. S.; Stroeve, P., An in vitro study of bare and poly(ethylene glycol)-co-fumarate-coated superparamagnetic iron oxide nanoparticles: a new toxicity identification procedure. *Nanotechnology* **2009,** *20*, 225104.

87. Johnston, H. J.; Hutchison, G.; Christensen, F. M.; Peters, S.; Hankin, S.; Stone, V., A review of the in vivo and in vitro toxicity of silver and gold particulates: particle attributes and biological mechanisms responsible for the observed toxicity. *Crit. Rev. Toxicol.* **2010,** *40*, 328.

88. Yan, M.; Zhang, Y.; Xu, K.; Fu, T.; Qin, H.; Zheng, X., An in vitro study of vascular endothelial toxicity of CdTe quantum dots. *Toxicology* **2011,** *282*, 94.

89. von Recklinghausen, U.; Hartmann, L. M.; Rabieh, S.; Hippler, J.; Hirner, A. V.; Rettenmeier, A. W.; Dopp, E., Methylated bismuth, but not bismuth citrate or bismuth glutathione, induces cyto- and genotoxic effects in human cells in vitro. *Chem. Res. Toxicol.* **2008,** *21*, 1219.

90. Talapin, D. V.; Rogach, A. L.; Kornowski, A.; Haase, M.; Weller, H., Highly luminescent monodisperse CdSe and CdSe/ZnS nanocrystals synthesized in a hexadecylamine-trioctylphosphine oxide-trioctylphospine mixture. *Nano Lett.* **2001,** *1*, 207.

91. Kirchner, C.; Liedl, T.; Kudera, S.; Pellegrino, T.; Munoz Javier, A.; Gaub, H. E.; Stolzle, S.; Fertig, N.; Parak, W. J., Cytotoxicity of colloidal CdSe and CdSe/ZnS nanoparticles. *Nano Lett.* **2005,** *5*, 331.

92. Tiwari, D. K.; Jin, T.; Behari, J., Bio-distribution and toxicity assessment of intravenously injected anti-HER2 antibody conjugated CdSe/ZnS quantum dots in Wistar rats. *Int. J. Nanomed.* **2011,** *6*, 463.

93. Naqvi, S.; Samim, M.; Abdin, M.; Ahmed, F. J.; Maitra, A.; Prashant, C.; Dinda, A. K., Concentration-dependent toxicity of iron oxide nanoparticles mediated by increased oxidative stress. *Int. J. Nanomed.* **2010,** *5*, 983.

94. Mahmoudi, M.; Simchi, A.; Milani, A. S.; Stroeve, P., Cell toxicity of superparamagnetic iron oxide nanoparticles. *J. Colloid Interface Sci.* **2009,** *336*, 510.

95. Gupta, A. K.; Berry, C.; Gupta, M.; Curtis, A., Receptor-mediated targeting of magnetic nanoparticles using insulin as a surface ligand to prevent endocytosis. *IEEE Trans. Nanobiosci.* **2003,** *2*, 255.

96. Park, J.; Fong, P. M.; Lu, J.; Russell, K. S.; Booth, C. J.; Saltzman, W. M.; Fahmy, T. M., PEGylated PLGA nanoparticles for the improved delivery of doxorubicin. *Nanomed. Nanotech. Biol. Med.* **2009,** *5*, 410.

97. Grace, M. B.; Moyer, B. R.; Prasher, J.; Cliffer, K. D.; Ramakrishnan, N.; Kaminski, J.; Coleman, C. N.; Manning, R. G.; Maidment, B. W.; Hatchett, R., Rapid Radiation Dose Assessment for Radiological Public Health Emergencies: Roles of Niaid and Barda. *Health Phys.* **2010,** *98*, 172.

98. Amundson, S. A.; Bittner, M.; Meltzer, P.; Trent, J.; Fornace, A. J., Jr., Biological indicators for the identification of ionizing radiation exposure in humans. *Expert Rev. Mol. Diagn.* **2001,** *1*, 211.

99. Vral, A.; Fenech, M.; Thierens, H., The micronucleus assay as a biological dosimeter of in vivo ionising radiation exposure. *Mutagenesis* **2011,** *26*, 11.

100. Hsieh, W. A.; Lucas, J. N.; Hwang, J. J.; Chan, C. C.; Chang, W. P., Biodosimetry using chromosomal translocations measured by FISH in a population chronically exposed to low dose-rate Co-60 gamma-irradiation. *Int. J. Radiat. Biol.* **2001,** *77*, 797.

101. Prasanna, P. G. S.; Kolanko, C. J.; Gerstenberg, H. M.; Blakely, W. F., Premature chromosome condensation assay for biodosimetry: Studies with fission-neutrons. *Health Phys.* **1997,** *72*, 594.

102. Redon, C. E.; Nakamura, A. J.; Gouliaeva, K.; Rahman, A.; Blakely, W. F.; Bonner, W. M., The use of gamma-H2AX as a biodosimeter for total-body radiation exposure in non-human primates. *PLoS ONE* **2010,** *5*, e15544.

103. Straume, T.; Lucas, J. N.; Tucker, J. D.; Bigbee, W. L.; Langlois, R. G., Biodosimetry for a Radiation Worker Using Multiple Assays. *Health Phys.* **1992,** *62*, 122.

104. Valcarcel, M.; Arteta, B.; Jaureguibeitia, A.; Lopategi, A.; Martinez, I.; Mendoza, L.; Muruzabal, F. J.; Salado, C.; Vidal-Vanaclocha, F., Three-dimensional growth as multicellular spheroid activates the proangiogenic phenotype of colorectal carcinoma cells via LFA-1-dependent VEGF: implications on hepatic micrometastasis. *J. Transl. Med.* **2008,** *6*, doi:10.1186/1479.

105. Ota, H.; Yamamoto, R.; Deguchi, K.; Tanaka, Y.; Kazoe, Y.; Sato, Y.; Miki, N., Three-dimensional spheroid-forming lab-on-a-chip using micro-rotational flow. *Sensor Actuat. B-Chem* **2010,** *147*, 359.

106. Yu, L.; Chen, M. C.; Cheung, K. C., Droplet-based microfluidic system for multicellular tumor spheroid formation and anticancer drug testing. *Lab Chip* **2010,** *10*, 2424.

107. Li, C. Y.; Wood, D. K.; Hsu, C. M.; Bhatia, S. N., DNA-templated assembly of droplet-derived PEG microtissues. *Lab Chip* **2011,** *11*, 2967.

108. Wang, W.; Itaka, K.; Ohba, S.; Nishiyama, N.; Chung, U. I.; Yamasaki, Y.; Kataoka, K., 3D spheroid culture system on micropatterned substrates for improved differentiation efficiency of multipotent mesenchymal stem cells. *Biomaterials* **2009,** *30*, 2705.

109. Zhu, H.; Mavandadi, S.; Coskun, A. F.; Yaglidere, O.; Ozcan, A., Optofluidic fluorescent imaging cytometry on a cell phone. *Anal. Chem.* **2011,** *83*, 6641.

110. Breslauer, D. N.; Maamari, R. N.; Switz, N. A.; Lam, W. A.; Fletcher, D. A., Mobile phone based clinical microscopy for global health applications. *PLoS ONE* **2009,** *4*, e6320.

111. Bourquin, Y.; Reboud, J.; Wilson, R.; Zhang, Y.; Cooper, J. M., Integrated immunoassay using tuneable surface acoustic waves and lensfree detection. *Lab Chip* **2011,** *11*, 2725.

112. Jiang, K.; Lancaster, M. J.; Llamas-Garro, I.; Jin, P., SU-8 Ka-band filter and its microfabrication. *J. Micromech. Microeng.* **2005,** *15*, 1522.

113. Just, L.; Kursten, A.; Borth-Bruhns, T.; Lindenmaier, W.; Rohde, M.; Dittmar, K.; Bader, A., Formation of three-dimensional fetal myocardial tissue cultures from rat for long-term cultivation. *Dev. Dynam.* **2006,** *235*, 2200.

114. Walters, R. A.; Petersen, D. F., Radiosensitivity of Mammalian Cells .I. Timing and Dose-Dependence of Radiation-Induced Division Delay. *Biophys. J.* **1968,** *8*, 1475.

115. Dean, C. J.; Feldschreiber, P.; Lett, J. T., Repair of X-ray damage to the deoxyribonucleic acid in Micrococcus radiodurans. *Nature* **1966,** *209*, 49.

116. Chithrani, D. B.; Jelveh, S.; Jalali, F.; van Prooijen, M.; Allen, C.; Bristow, R. G.; Hill, R. P.; Jaffray, D. A., Gold nanoparticles as radiation sensitizers in cancer therapy. *Radiat. Res.* **2010,** *173*, 719.

117. Mesbahi, A., A review on gold nanoparticles radiosensitization effect in radiation therapy of cancer. *Rep. Prac. Oncol. Radiother.* **2010,** *15*, 176.

118. Hainfeld, J. F.; Dilmanian, F. A.; Zhong, Z.; Slatkin, D. N.; Kalef-Ezra, J. A.; Smilowitz, H. M., Gold nanoparticles enhance the radiation therapy of a murine squamous cell carcinoma. *Phys. Med. Biol.* **2010,** *55*, 3045.

119. Rahman, W. N.; Bishara, N.; Ackerly, T.; He, C. F.; Jackson, P.; Wong, C.; Davidson, R.; Geso, M., Enhancement of radiation effects by gold nanoparticles for superficial radiation therapy. *Nanomed-Nanotechnol.* **2009,** *5*, 136.

120. Hainfeld, J. F.; Dilmanian, F. A.; Slatkin, D. N.; Smilowitz, H. M., Radiotherapy enhancement with gold nanoparticles. *J. Pharm. Pharmacol.* **2008,** *60*, 977.

121. Roa, W.; Zhang, X. J.; Guo, L. H.; Shaw, A.; Hu, X. Y.; Xiong, Y. P.; Gulavita, S.; Patel, S.; Sun, X. J.; Chen, J.; Moore, R.; Xing, J. Z., Gold nanoparticle sensitize radiotherapy of prostate cancer cells by regulation of the cell cycle. *Nanotechnology* **2009,** *20*.

122. Polf, J. C.; Bronk, L. F.; Driessen, W. H. P.; Arap, W.; Pasqualini, R.; Gillin, M., Enhanced relative biological effectiveness of proton radiotherapy in tumor cells with internalized gold nanoparticles. *Appl. Phys. Lett.* **2011,** *98*, 193702.

123. Berbeco, R. I.; Ngwa, W.; Makrigiorgos, G. M., Localized dose enhancement to tumor blood vessel endothelial cells via megavoltage X-rays and targeted gold nanoparticles: new potential for external beam radiotherapy. *Int. J. Radiat. Oncol* . **2011,** *81*, 270.

124. Hainfeld, J. F.; Slatkin, D. N.; Smilowitz, H. M., The use of gold nanoparticles to enhance radiotherapy in mice. *Phys. Med. Biol.* **2004,** *49*, N309.

125. Lechtman, E.; Chattopadhyay, N.; Cai, Z.; Mashouf, S.; Reilly, R.; Pignol, J. P., Implications on clinical scenario of gold nanoparticle radiosensitization in regards to photon energy, nanoparticle size, concentration and location. *Phys. Med. Biol.* **2011,** *56*, 4631.

126. Cho, S. H., Estimation of tumour dose enhancement due to gold nanoparticles during typical radiation treatments: a preliminary Monte Carlo study. *Phys. Med. Biol.* **2005,** *50*, N163.

127. Cho, S. H.; Jones, B. L.; Krishnan, S., The dosimetric feasibility of gold nanoparticle-aided radiation therapy (GNRT) via brachytherapy using low-energy gamma-/X-ray sources. *Phys. Med. Biol.* **2009,** *54*, 4889.

128. Lin, H. K.; Zheng, S.; Williams, A. J.; Balic, M.; Groshen, S.; Scher, H. I.; Fleisher, M.; Stadler, W.; Datar, R. H.; Tai, Y.-C.; Cote, R. J., Portable filter-based microdevice for detection and characterization of circulating tumor cells. *Clin. Cancer Res.* **2010,** *16*, 5011.

129. Jones, B. L.; Krishnan, S.; Cho, S. H., Estimation of microscopic dose enhancement factor around gold nanoparticles by Monte Carlo calculations. *Med. Phys* . **2010,** *37*, 3809.

130. Lee, C.; Cheng, N. N.; Davidson, R. A.; Guo, T., Geometry enhancement of nanoscale energy deposition by X-rays. *J. Phys. Chem. C* **2012,** *116*, 11292.

131. Ngwa, W.; Makrigiorgos, G. M.; Berbeco, R. I., Applying gold nanoparticles as tumor-vascular disrupting agents during brachytherapy: estimation of endothelial dose enhancement. *Phys. Med. Biol.* **2010,** *55*, 6533.

132. McMahon, S. J.; Hyland, W. B.; Muir, M. F.; Coulter, J. A.; Jain, S.; Butterworth, K. T.; Schettino, G.; Dickson, G. R.; Hounsell, A. R.; O'Sullivan, J. M.; Prise, K. M.; Hirst, D. G.; Currell, F. J., Biological consequences of nanoscale energy deposition near irradiated heavy atom nanoparticles. *Sci Rep-Uk* **2011,** *1*, 18.

133. Carter, J. D.; Cheng, N. N.; Qu, Y.; Suarez, G. D.; Guo, T., Nanoscale energy deposition by X-ray absorbing nanostructures. *J. Phys. Chem. B* **2007,** *111*, 11622.

134. Munro, T. R., The Relative Radiosensitivity of the Nucleus and Cytoplasm of Chinese Hamster Fibroblasts. *Radiat. Res.* **1970,** *42*, 451.

135. Ngwa, W.; Makrigiorgos, G. M.; Berbeco, R. I., Gold nanoparticle-aided brachytherapy with vascular dose painting: Estimation of dose enhancement to the tumor endothelial cell nucleus. *Med. Phys.* **2012,** *39*, 392.

136. Kang, B.; Mackey, M. A.; El-Sayed, M. A., Nuclear targeting of gold nanoparticles in cancer cells induces DNA damage, causing cytokinesis arrest and apoptosis. *J. Am. Chem. Soc.* **2010,** *132*, 1517.

137. Praetorius, N. P.; Mandal, T. K., Engineered nanoparticles in cancer therapy. *Recent Pat. Drug Deliv. Formul* . **2007,** *1*, 37.

138. Liehn, S.; Sech, C. L.; Porcel, E.; Zielbauer, B.; Habib, J.; Kazamias, S.; Guilbaud, O.; Pittman, M.; Ros, D.; Penhoat, M.-A. H. d.; Touati, A.; Remita, H.; Lacombe, S., Biological effects induced by low energy X-rays: effects of nanoparticles. *Proc. SPIE* **2009,** *7451*, 74510Z.

139. Porcel, E.; Liehn, S.; Remita, H.; Usami, N.; Kobayashi, K.; Furusawa, Y.; Le Sech, C.; Lacombe, S., Platinum nanoparticles: a promising material for future cancer therapy? *Nanotechnology* **2010,** *21*.

140. Rabin, O.; Manuel Perez, J.; Grimm, J.; Wojtkiewicz, G.; Weissleder, R., An X-ray computed tomography imaging agent based on long-circulating bismuth sulphide nanoparticles. *Nat Mater* **2006,** *5*, 118.

141. Kinsella, J. M.; Jimenez, R. E.; Karmali, P. P.; Rush, A. M.; Kotamraju, V. R.; Gianneschi, N. C.; Ruoslahti, E.; Stupack, D.; Sailor, M. J., X-ray computed tomography imaging of breast cancer by using targeted peptide-labeled bismuth sulfide nanoparticles. *Angew. Chem. Int. Ed.* **2011,** *50*, 12308.

142. Kobayashi, K.; Usami, N.; Porcel, E.; Lacombe, S.; Le Sech, C., Enhancement of radiation effect by heavy elements. *Mutation Res.* **2010,** *704*, 123.

143. Cole, A., Absorption of 20-eV to 50,000-eV electron beams in air and plastic. *Radiat. Res.* **1969,** *38*, 7.

144. Specification of X-ray beams. *J. ICRU* **2005,** *5*, 21.